Document Version
Final published version

Citation (APA)
Chapeland, C. G. M. (2026). *Towards improved seismic methods for investigating the offshore shallow subsurface: From inversion and imaging methods to acquisition hardware development*. [Dissertation (TU Delft), Delft University of Technology]. https://doi.org/10.4233/uuid:7b349768-f302-45d2-a59a-61b6ae95bf24

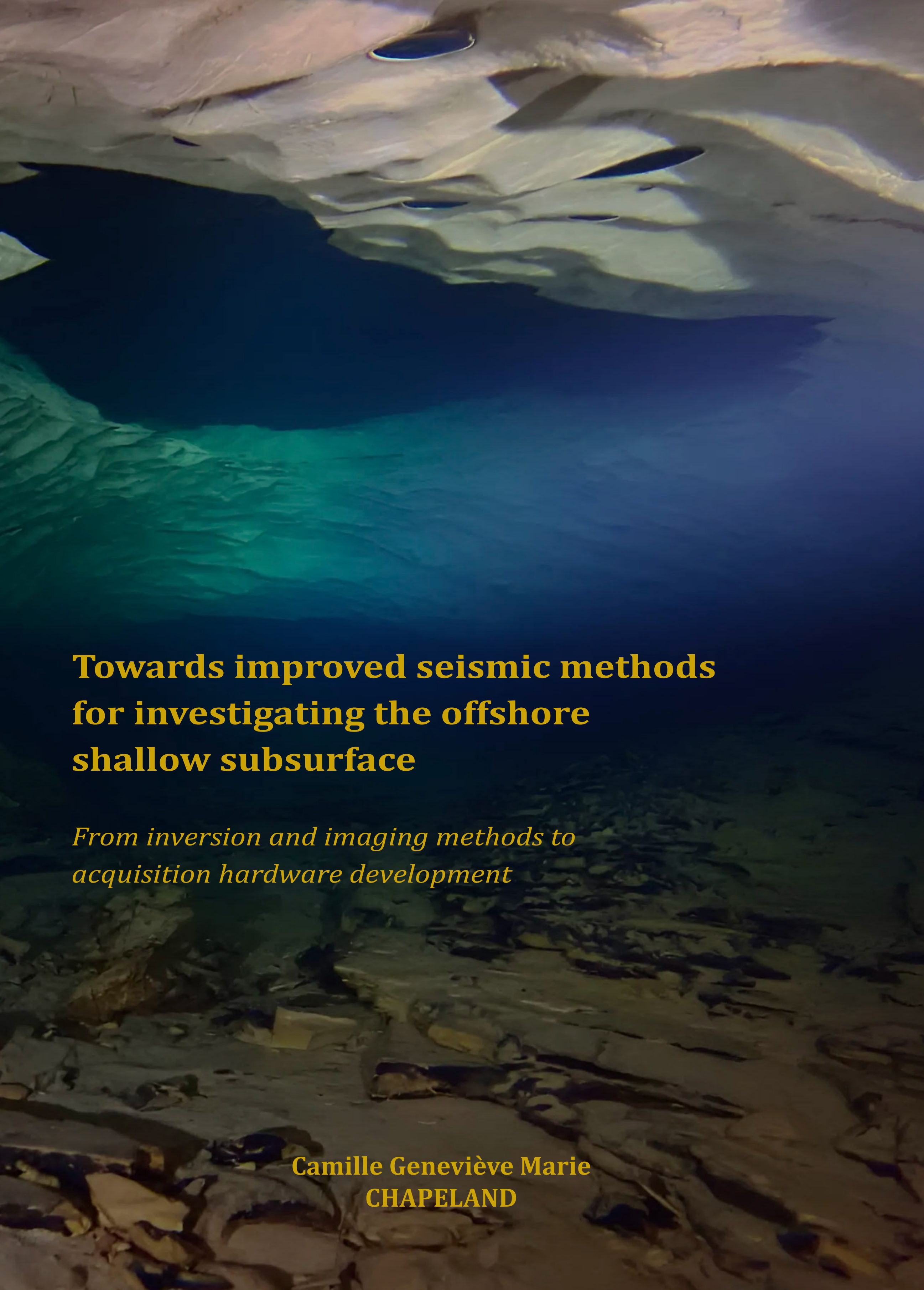

Towards improved seismic methods for investigating the offshore shallow subsurface

From inversion and imaging methods to acquisition hardware development

Camille Geneviève Marie
CHAPELAND

TOWARDS IMPROVED SEISMIC METHODS FOR INVESTIGATING THE OFFSHORE SHALLOW SUBSURFACE

FROM INVERSION AND IMAGING METHODS TO ACQUISITION HARDWARE DEVELOPMENT

TOWARDS IMPROVED SEISMIC METHODS FOR INVESTIGATING THE OFFSHORE SHALLOW SUBSURFACE

FROM INVERSION AND IMAGING METHODS TO ACQUISITION HARDWARE DEVELOPMENT

Dissertation

for the purpose of obtaining the degree of doctor
at Delft University of Technology
by the authority of the Rector Magnificus, Prof.dr.ir. H. Bijl
chair of the Board for Doctorates
to be defended publicly on
Thursday 9 April 2026 at 17 :30

by

Camille Geneviève Marie CHAPELAND

This dissertation has been approved by the promotors.

Composition of the doctoral committee :

Rector Magnificus,	chairperson
Dr. ir. D. J. Verschuur,	Delft University of Technology, *promotor*
Dr. ir. D. S. Draganov,	Delft University of Technology, *promotor*

Independent members :

Prof. dr. ir. E. C. Slob	Delft University of Technology
Prof. dr. L. G. Evers	Delft University of Technology / KNMI, NL
Prof. dr. T. J. Henstock	University of Southampton, UK
Dr. ir. G. G. Drijkoningen	Delft University of Technology
Dr. P. Hanssen	Equinor, Norway

Printed by : RidderPrint
Cover photo by : Mike van Schenkhof and Camille Chapeland
Cover design by : Marie and Camille Chapeland

The work in this dissertation was conduction at the department of Geoscience and Engineering, Faculty of Civil Engineering and Geosciences, Delft University of Technology within the Delphi Consortium. Part of the work in this dissertation was supported financially by Deltares.

ISBN 978-94-6537-404-8

À Balou, Kiwi, Tobo, Mint et Miko.

TABLE DES MATIÈRES

SUMMARY

In this thesis, we focus on two areas relevant to improving near-surface offshore seismic surveys : inversion-based estimation of subsurface properties and the monitoring of the acquisition-geometry. These issues remain challenging in ultra-high-resolution (UHR) marine geophysics, where imaging the first tens of meters below the seafloor can be limited by both data quality and instrument uncertainties. Through a combination of modelling- and field-data studies and experimental hardware development, we investigate the possibilities for enhancing the characterization of this shallow region which is of interest for the development and monitoring of offshore infrastructure and subsurface resources extraction.

In the first part of this research, we revisit the foundations of seismic-velocity model building for UHR data. Standard approaches such as Full Waveform Inversion (FWI) often fail under the limitations typical of near-surface surveys which can be characterise by short offsets, limited low-frequency content, and inaccurate starting velocity models. To overcome these challenges, we introduce and evaluate a sequential inversion workflow that integrates Joint Migration Inversion (JMI) and FWI. Using synthetic experiments, we demonstrate that JMI can reliably retrieve the low-wavenumber background velocity by simultaneously inverting for reflectivity and transmission effects, providing a stable foundation for subsequent FWI refinement. We show that the workflow successfully reconstructs complex near-surface structures such as layered sediments and buried diffractors—features that conventional inversion methods often misinterpret or miss entirely.

We then apply the workflow to a field dataset acquired at a Dutch North Sea wind farm site, representative of modern offshore engineering surveys. In this field case, FWI alone fails to converge due to the absence of refracted arrivals and the dominance of reflected energy. Conversely, JMI produces more robust results, revealing the presence of a high-velocity layer relevant for geotechnical planning of monopile foundations. Our comparison emphasizes a key conclusion : in UHR seismic acquisition, where offsets are short and data bandwidths limited, the JMI framework offers a more viable approach to reconstructing near-

surface velocity models than conventional FWI. The results also highlight a critical dependency between data quality and hardware performance, motivating the second part of our research.

In the second half of the thesis, we address a major hardware limitation in UHR seismic acquisition : the poor control and monitoring of hydrophone positions along the streamer. In such surveys, precise receiver positioning is vital, as even small uncertainties in depth or lateral displacement can distort amplitude spectra and be detrimental to subsequent processing that relies on relative source and hydrophone positions. However, unlike exploration-scale streamers, UHR streamers lack embedded GPS or inertial navigation systems. To overcome this, we propose a novel method based on Fiber-Optic Shape Sensing (FOSS) — a technology that translates distributed strain measurements in multi-core optical fibers into three-dimensional shape reconstructions.

After performing a detailed theoretical analysis of FOSS principles, we then design dedicated sensor architecture for geophysical and geotechnical use. The design considerations include interrogator selection, core geometry, embedding configuration, and shape reconstruction algorithms. We develop a prototype, the SSU2000, and test it in both bench setups and a controlled flume environment. Our experiments successfully demonstrate the feasibility of reconstructing the 3D streamer shape and hydrophone depths in real time. The reconstructed positions are then used to perform receiver-side deghosting, recovering lost spectral amplitudes and improving the vertical resolution of the seismic data. While we observe some limitations in the sensor embedding and curvature handling, the proof-of-concept experiments validate FOSS as a viable solution to the positioning problem in marine UHR acquisition.

In the concluding chapter we expand on the implications of the developments described above. On the inversion side, the integration of JMI into near-surface workflows opens new pathways for shallow imaging where traditional reflection or refraction-based inversions fail. On the hardware side, extending FOSS into long-distance distributed sensing (LD-FOSS) presents opportunities beyond seismic applications — including unmanned underwater vehicle navigation, tethered robotics, and continuous structural-health monitoring. Both innovations represent a shift toward hybrid solutions where computational algorithms and physical sensing systems evolve together to address the limits of marine data fidelity.

Ultimately, with this thesis we demonstrate that improving offshore imaging requires more than algorithmic sophistication alone ; the improvement depends equally on the precision of the instruments used to acquire the data. By uniting advancements in seismic inversion and fiber-optic sensing, our work contributes to the broader goal of reliable high-resolution marine subsurface characterization —an essential foundation for future offshore infrastructure, environmental monitoring, and resource management.

SAMENVATTING

In dit proefschrift richten we ons op twee gebieden die relevant zijn voor het verbeteren van near-surface offshore seismische onderzoeken: inversiegebaseerde schatting van ondergrondse eigenschappen en het monitoren van de acquisitiegeometrie. Deze vraagstukken blijven uitdagend binnen de ultra-high-resolution (UHR) mariene geofysica, waar de beeldvorming van de eerste tientallen meters onder de zeebodem wordt beperkt door zowel datakwaliteit als instrumentonzekerheden. Door een combinatie van modelleer- en veldgegevensstudies en experimentele hardwareontwikkeling onderzoeken we de mogelijkheden om de karakterisatie van deze ondiepe zone te verbeteren — een gebied dat van belang is voor de ontwikkeling en monitoring van offshore-infrastructuur en de winning van ondergrondse hulpbronnen.

In het eerste deel van dit onderzoek herzien we de fundamenten van seismische snelheidsmodelbouw voor UHR-data. Standaardmethoden zoals Full Waveform Inversion (FWI) falen vaak onder de typische beperkingen van near-surface-onderzoeken, die gekenmerkt kunnen worden door korte offsets, beperkte laagfrequente inhoud en onnauwkeurige startsnelheidsmodellen. Om deze uitdagingen te overwinnen introduceren en evalueren wij een sequentiële inversieworkflow die Joint Migration Inversion (JMI) en FWI integreert. Met synthetische experimenten tonen we aan dat JMI in staat is het laag-golftal achtergrond snelheidsmodel betrouwbaar te reconstrueren door gelijktijdig in reflectiviteit en transmissie-effecten te inverteren, waarmee een stabiele basis ontstaat voor verdere FWI-verfijning. We laten zien dat de workflow complexe near-surface structuren — zoals gelaagde sedimenten en begraven diffractors — succesvol kan reconstrueren, structuren die door conventionele inversiemethoden vaak verkeerd worden geïnterpreteerd of geheel worden gemist.

Vervolgens passen we de workflow toe op een velddataset die is verkregen op een windparklocatie in de Nederlandse Noordzee, representatief voor moderne offshore ingenieursonderzoeken. In deze veldcase convergeert FWI op zichzelf niet vanwege het ontbreken van gerefractieerde aankomsten en de dominantie van gereflecteerde energie. Daarentegen levert JMI robuustere resultaten op en onthult het de aanwezigheid van een hoge-snelheidlaag die relevant is voor ge-

otechnische planning van monopile-fundaties. Onze vergelijking benadrukt een kernconclusie: in UHR-seismische acquisitie, waar offsets kort zijn en de databandbreedte beperkt is, biedt het JMI-raamwerk een haalbaarder aanpak voor het reconstrueren van near-surface snelheidsmodellen dan conventionele FWI. De resultaten onderstrepen tevens een kritieke afhankelijkheid tussen datakwaliteit en hardwareprestaties, wat de aanleiding vormt voor het tweede deel van ons onderzoek.

In de tweede helft van dit proefschrift richten we ons op een belangrijke hardwarebeperking in UHR-seismische acquisitie: de beperkte controle en monitoring van hydrofoonposities langs de streamer. In dergelijke onderzoeken is precieze ontvangerpositionering cruciaal, aangezien zelfs kleine onzekerheden in diepte of laterale verplaatsing de amplitudespectra kunnen verstoren en nadelig kunnen zijn voor daaropvolgende verwerking die afhankelijk is van relatieve bron- en hydrofoonposities. Anders dan exploratie-schaal streamers beschikken UHR-streamers echter niet over ingebouwde GPS- of inertiaalnavigatiesystemen. Om dit te verhelpen stellen we een nieuwe methode voor op basis van Fiber-Optic Shape Sensing (FOSS) — een technologie die gedistribueerde rekmetingen in multi-core optische vezels omzet in driedimensionale vormreconstructies.

Na een gedetailleerde theoretische analyse van de FOSS-principes ontwerpen we vervolgens een specifieke sensorarchitectuur voor geofysische en geotechnische toepassingen. De ontwerpkeuzes omvatten de selectie van de interrogator, de kerngeometrie, de inbeddingsconfiguratie en de algoritmen voor vormreconstructie. We ontwikkelen een prototype, de SSU2000, en testen dit zowel in laboratoriumopstellingen als in een gecontroleerde flume-omgeving. Onze experimenten tonen succesvol de haalbaarheid aan van het reconstrueren van de 3D-streamervorm en hydrofoondiepten in real time. De gereconstrueerde posities worden vervolgens gebruikt voor ontvanger-zijdige deghosting, waarbij verloren spectrale amplitudes worden teruggewonnen en de verticale resolutie van de seismische data wordt verbeterd. Hoewel we enkele beperkingen waarnemen in de inbedding van de sensor en de behandeling van kromming, bevestigen de proof-of-concept-experimenten dat FOSS een haalbare oplossing vormt voor het positioneringsprobleem binnen mariene UHR-acquisitie.

In het afsluitende hoofdstuk gaan we dieper in op de implicaties van de hierboven beschreven ontwikkelingen. Aan de inversiekant opent de integratie van JMI in near-surface workflows nieuwe mogelijkheden voor ondiepe beeldvorming wanneer traditionele reflectie - of refractiegebaseerde inversies tekortschieten.

Aan de hardwarekant biedt uitbreiding van FOSS naar long-distance distributed sensing (LD-FOSS) kansen buiten seismische toepassingen — waaronder navigatie van onbemande onderwatervoertuigen, getetherde robotica en continue structurele conditiebewaking. Beide innovaties vertegenwoordigen een verschuiving naar hybride oplossingen waarbij computationele algoritmen en fysieke sensorsystemen gezamenlijk evolueren om de grenzen van mariene data-fideliteit te doorbreken.

Uiteindelijk laten we met dit proefschrift zien dat verbetering van offshore beeldvorming meer vereist dan alleen algoritmische verfijning; de vooruitgang hangt evenzeer af van de precisie van de instrumenten die worden gebruikt voor de dataverwerving. Door innovaties in seismische inversie en vezeloptische sensortechnologie te verenigen, draagt ons werk bij aan het bredere doel van betrouwbare hoog-resolutie karakterisatie van de mariene ondergrond — een essentiële basis voor toekomstige offshore-infrastructuur, milieumonitoring en hulpbronnenbeheer.

SOMMAIRE

Dans cette thèse, nous nous concentrons sur deux domaines essentiels à l'amélioration des études sismiques offshore de proche surface : l'estimation par inversion des propriétés du sous-sol et le suivi de la géométrie de la flûte sismique au cours des campagnes sismiques. Ces problématiques restent complexes dans le cadre de la sismique marine à Ultra-Haute Résolution (UHR), où l'imagerie des premières dizaines de mètres sous le fond marin est limitée à la fois par la qualité des données et par les incertitudes instrumentales. Grâce à une combinaison d'études basées sur des données réelles et synthétiques, ainsi que sur le développement expérimental de nouvelles méthodes instrumentales, nous explorons les possibilités d'améliorer la caractérisation de cette zone de profondeur superficielle, qui est d'intérêt majeur pour le développement et le suivi des infrastructures offshore ainsi que pour la cartographie des ressources du sous-sol.

Dans la première partie de cette recherche, nous revisitions les fondements de la construction de modèles de vitesse sismique pour les données UHR. Les approches standards, telles que l'inversion de formes d'ondes complètes (nommé Full-Waveform Inversion ou FWI dans la littérature scientifique internationale), échouent souvent en raison des limitations typiques des mesures de proche surface. Celles-ci sont généralement caractérisées par des décalages source-récepteur courts, un contenu de fréquences basses limité et des modèles de vitesse initiaux imprécis. Pour surmonter ces défis, nous présentons et évaluons une méthode d'inversion séquentielle intégrant la migration et inversion jointes (similairement nommé Joint Migration Inversion ou JMI) et la FWI. À l'aide d'expériences synthétiques, nous démontrons que la JMI permet de reconstruire de manière fiable le fond de vitesse à bas nombre d'ondes en inversant simultanément la réflectivité et les effets de transmission, fournissant ainsi une base stable pour un raffinement ultérieur par FWI. Nous montrons que cette méthodologie permet de reconstruire des structures complexes du sous-sol de proche surface telles que des sédiments stratifiés et des corps (géologiques) diffracteurs enfouis — des éléments que les méthodes d'inversion classiques interprètent souvent médiocrement ou manquent complètement.

Nous appliquons ensuite cette méthodologie à un jeu de données acquis sur un site de parc éolien en mer du Nord néerlandaise, représentatif des campagnes sismiques appliquées à l'ingénierie offshore moderne. Dans ce cas réel, la FWI seule ne converge pas en raison de l'absence d'ondes réfractées et de la dominance de l'énergie réfléchie. À l'inverse, la JMI produit des résultats plus robustes et révèle la présence d'une couche à haute vitesse pertinente pour la planification géotechnique des fondations monopieux. Notre comparaison met en évidence une conclusion clé : dans l'acquisition sismique UHR, où les distances source-recepteur sont courtes et la bande passante fréquentielle des données limitée, le cadre JMI constitue une approche plus viable pour reconstruire les modèles de vitesse du sous-sol proche que la FWI conventionnelle. Les résultats soulignent également une dépendance critique entre la qualité des données et la performance du matériel d'acquisition des mesures, ce qui motive la seconde partie de notre étude.

Dans la deuxième partie de la thèse, nous abordons une limitation matérielle majeure dans l'acquisition sismique UHR : le contrôle et le suivi insuffisants des positions des hydrophones le long de la flûte sismique. Dans ces acquisitions, une localisation précise des hydrophones est essentielle, car même de faibles incertitudes en profondeur ou en déplacement latéral peuvent distordre les spectres fréquentiels et compromettre les traitements ultérieurs qui s'appuient sur les positions relatives de la source et des hydrophones. Contrairement aux flûtes utilisées pour l'exploration pétrolière, les flûtes UHR ne disposent pas de GPS intégrés ni de systèmes de navigation inertielle. Pour remédier à cette limitation, nous proposons une méthode innovante basée sur la détection de forme utilisant la fibre optique (nommée Fiber-Optic Shape Sensing ou FOSS) — une technologie qui convertit des mesures distribuées de déformation dans des senseurs optiques multi-cœurs en reconstructions tridimensionnelles de la forme.

Après avoir réalisé une analyse théorique détaillée des principes du FOSS, nous concevons une architecture de capteur dédiée aux applications géophysiques et géotechniques. Les considérations de conception incluent le choix de l'interrogateur, la géométrie des fibres, la configuration d'intégration dans le streamer et les algorithmes de reconstruction de forme. Nous développons un prototype, le SSU2000, et le testons à la fois en laboratoire et dans un canal hydraulique contrôlé. Nos expériences démontrent avec succès la faisabilité de reconstruire en temps réel la forme 3D du streamer et la profondeur des hydrophones. Les positions reconstruites sont ensuite utilisées pour effectuer un traitement de l'empreinte des réverbérations de surface qui se présentent comme des encoches dans le domaine des fréquences. Ceci permet de récupérer les amplitudes spectrales perdues et d’améliorer la résolution verticale des données sismiques. Bien que nous observions certaines limites liées à l’intégration du capteur et à la gestion des courbures, ces expériences de preuve de concept valident le FOSS comme solution viable au problème de positionnement dans l’acquisition marine UHR.

Dans le dernier chapitre, nous approfondissons les implications des développements présentés ci-dessus. Du point de vue de l’inversion, l’intégration de la JMI dans les méthodes sismiques appliquées aux sous-sols peu profonds, ouvre de nouvelles perspectives pour l’imagerie lorsque les inversions traditionnelles basées sur la réflexion ou la réfraction échouent. Du point de vue matériel, l’extension du FOSS vers la longue distance offre des opportunités au-delà des applications sismiques — notamment la navigation de véhicules sous-marins autonomes, la robotique et le suivi en temps réel des infrastructures. Ces deux innovations représentent une évolution vers des solutions hybrides où les algorithmes de calcul et les systèmes de détection physique progressent conjointement afin de repousser les limites de la fidélité des données marines.

Finalement, cette thèse démontre que l’amélioration de l’imagerie offshore nécessite plus qu’une sophistication algorithmique : elle dépend tout autant de la précision des instruments utilisés pour acquérir les données. En réunissant les avancées de l’inversion sismique et de la détection par fibres optiques, nos travaux contribuent à l’objectif plus large d’une caractérisation marine du sous-sol à haute résolution — un fondement essentiel pour les futures infrastructures offshore, le suivi environnemental et la gestion des ressources.

1

INTRODUCTION

It is colloquially said that man knows more about the surface of the moon than the bottom of the ocean. Yet, we have utilised the seafloor and its immediate subsurface much more than we have the moon at this point in time.

The goal of the research in this thesis is to improve the performance of existing methods to understand the geometry and composition of the subsurface immediately under our oceans, seas, lakes, and rivers. With a breadth of methods to choose from, we focus on the high-resolution seismic method as it allows us to significantly penetrate the subsurface and derive material parametres from the wave propagation phenomenon.

1.1. INTEREST IN THE OFFSHORE NEAR-SURFACE

Historically, the ground below the seafloor has been utilised to tap into large hydrocarbon deposits that accumulated from plant material in the Carboniferous period, some 300 million years ago. Generally, such organic-matter reservoirs can be found at depths of 1,000 to 6,000 metres below the seafloor. Seismic methods that can penetrate deep within the subsurface are critical in locating them, mapping their geometry, and planning the efforts to drill and access the deposits [1]. In recent decades, interest in the offshore near-subsurface has steadily increased with the expansion of infrastructure and the installation of underwater cables for intercontinental communication and energy transmission. These geo-engineering projects require increasingly accurate and high-resolution imaging of the shallow subsurface. Additionally, conventional (deep) exploration seismologists recognize that a more precise characterization of a reservoir's overburden greatly improves its imaging, especially in the context of time-lapse seismics. Some more detailed examples include :

- **Dutch offshore wind energy investiture :** The expansion of wind farms in the North Sea has been a pivotal development in Europe's energy transition since the 2015 Paris Climate Agreement. The region is critical for offshore renewable energy due to its wind resources, favorable geography with a shallow water layer, and already established energy infrastructure. As of April 2024, the Dutch government alone reports 10 active wind farms in the Dutch North Sea, which have a total production capacity of 4.7 GW [2]. Although the Netherlands originally pledged to produce 49 TWh of offshore wind energy per year by 2030 (requiring a capacity of 11.5 GW), in 2022, the government increased the target to 21 GW by 2033 [3]. This investment in offshore wind turbine infrastructure requires a detailed investigation of potential wind farm sites, and seismic methods have responded to the demand by developing increasingly higher-resolution survey systems and processing methods [4]-[6]. Specifically, these surveys aim to : 1. identify objects of interest like boulders, and submarine communication and energy transmission cables; 2. investigate the geometry and composition of the subsurface. It is reported that approximately 10% of piling attempts were unsuccessful due to unexpected encounters with hard strata and objects like boulders [7]. These failed attempts can directly result in damage to the pile, leading to delays and increases in operational costs [8]. Equipped with the results of relevant geophysical surveys, operators and governments can make informed decisions where the operational risks during construction are minimized and the design of the infrastructure is appropriate for its full lifecycle [9]. Finally, as can be seen in Figure 1.1, offshore wind farms are themselves adding infrastructure to an already heavily utilised Dutch North Sea territory. Notably, this figure omits all infrastructure related to hydrocarbon extraction, which is also a major operation in the area. Managing the existing infrastructure in this increasingly complex environment requires a significant effort in shallow subsurface exploration and monitoring [10], [11].

- **Overburden characterization for complete reservoir exploitation in the Gulf of Mexico :** The term "overburden" refers to the layers of rock, sediment, or other material that lie directly above a target of interest in the subsurface. Because of its location, all seismic information

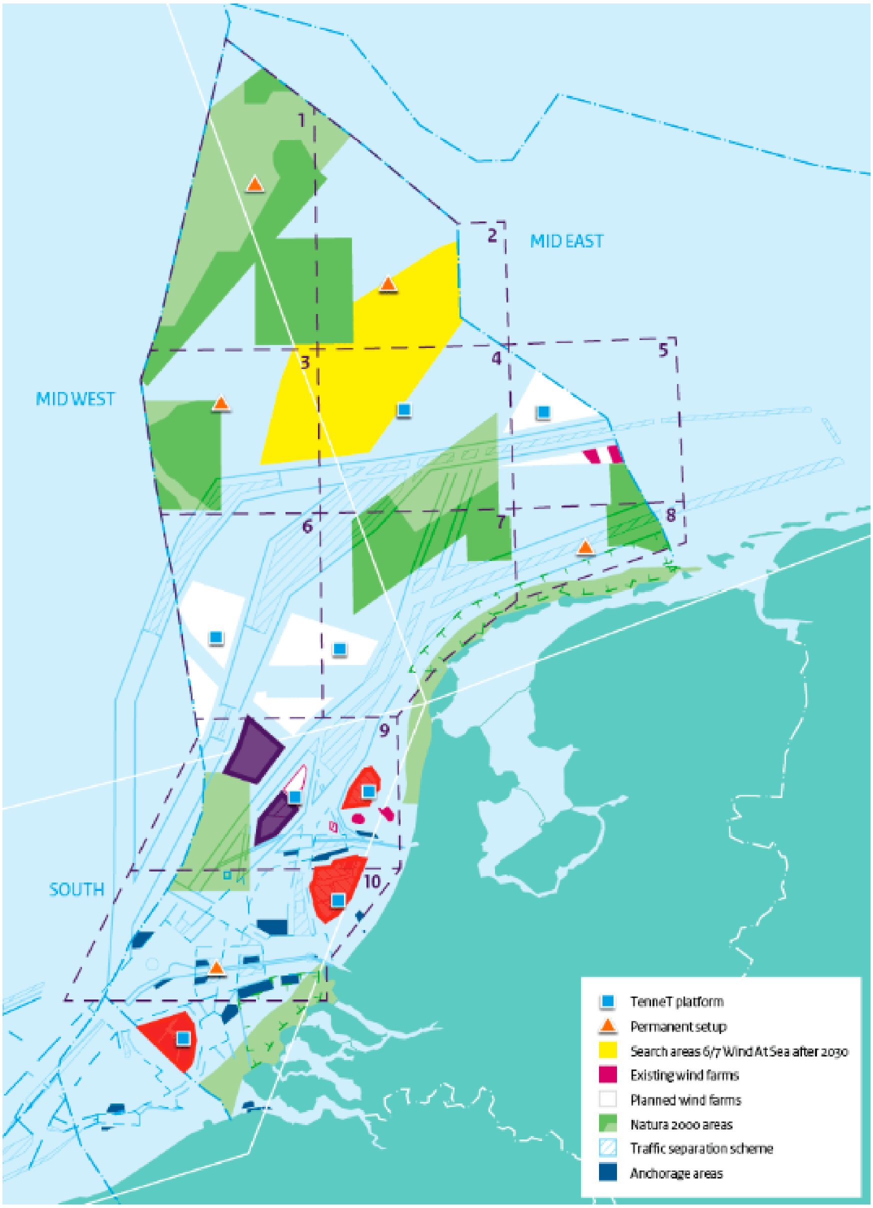

FIGURE 1.1. – *Map showing the boundary of the Dutch North Sea territory (blue dotted line) and the existing (pink) and planned (white) wind farm locations up to 2030. The wind farms with granted permits to be developed between 2025 and 2029 are shown in purple.* [12]

from a source at the surface to a receiver at the surface will travel through the overburden twice : once on the way down to the target and once on the way back up to the receiver. Moreover, proximity to the surface means that the overburden will change more rapidly in geological time compared to deeper layers, and will often feature a complex, shallow stratigraphy, which leads to elastic-wave effects, attenuation and scattering of the seismic signal [13]. Historically, the effects of the overburden on acquired data were generally ignored as resolving other factors had a more significant impact on the imaging results. However, with the growing concerns regarding the finite nature of non-renewable energies, governments and companies have focused their efforts towards fully exploiting known reservoirs. To do so, increased resources have gone towards high-resolution imaging of the reservoir. Part of this effort has involved investigating the effects of the overburden on deep target imaging, specifically in a monitoring context-also referred to as time-lapse or 4D [14]. In 2021, NCS SubSea completed a 4D Ultra-High-Resolution (UHR) seismic survey in the US Gulf of Mexico to map the overburden of a well-studied reservoir [15]. Although the results of this survey remain undisclosed, NCS SubSea suggests that the survey aims to improve the client's understanding of reservoir production performance and to provide data for further development of their asset.

— **Re-utilization of depleted reservoirs in the North Sea :** The development of Carbon Capture and Storage (CCS) in depleted offshore reservoirs has also gained traction in recent years. The intention is to capture atmospheric carbon dioxide (CO_2) and permanently store it in the subsurface to mitigate the effects of global warming. In March 2023, Project Greensand demonstrated for the first time that it is possible to transport captured CO_2 across borders and safely store it offshore [16]. Because this is a relatively new application, governments and regulatory bodies require extensive monitoring programs to be implemented to ensure long-term storage integrity and environmental safety. A key example is the PORTHOS CCS project, in the Dutch North Sea, scheduled to begin injection in 2026. This project includes a comprehensive monitoring plan using seismic, geochemical, and geotechnical techniques throughout its operational life [17], [18]. While the risk of CO_2 leakage into marine environments is low, monitoring using diverse technologies is required to detect and quantify potential leaks and to address natural overburden variability. Specifically, seismic surveys can identify potential risks such as faults, fractures, or subsurface voids that could compromise the integrity of the CCS reservoir in the long term; thus, they are a critical tool to ensure that CCS remains a permanent and safe carbon-storage solution [19].

— **Unforeseen environmental consequences of warfare :** Following World Wars I and II, significant amounts of explosive ordnance were left undetonated. Deployed unexploded munitions were often abandoned, and surplus supplies were discarded, sometimes carelessly. As a result, large quantities of unexploded ordnances (UxOs) persist in the environment, particularly in the oceans, where they continue to pose substantial risks to human safety, offshore infrastructure, and the marine ecosystem [20]. Techniques to locate UxOs in the environment are often "multi-physical" in nature. A common method is to carry out two concurrent surveys : 1. a magnetometry survey that can discretely measure the magnetic force, responding to the ferromagnetic nature of UxOs; 2. a high-resolution acoustic survey (seismic or subbottom profiling) to detect the precise location of the anomaly [21], [22].

— **South Korea's floating city :** In 2024, the South Korean government unveiled its plan for a floating city in Busan [23]. Geophysical surveys were carried out in the area in the previous year, and it could be inferred that the subsurface information will inform the construction and monitoring of the floating city [24]. The development of floating coastal offshore infrastructure is not unique and presents several advantages over traditional sea-reclamation projects : 1. the environmental damage is reduced as the sea bottom remains free to be populated by indigenous ecosystems; 2. they are resistant to water-level changes and flooding; 3. they can be designed in a modular fashion that can permit expansion to accommodate growing populations [25]. Monitoring the stability of the subsurface in which these cities are anchored will be a crucial aspect in ensuring the safety and viability of these structures in the long term.

The offshore subsurface has become an important aspect of modern economic development, supporting critical activities ranging from renewable-energy expansion and large-scale carbon-storage efforts to the development of new urban environments. As the demands on offshore spaces continue to grow, a detailed understanding of the shallow subsurface is essential to ensure that offshore infrastructure remains safe, resilient, and capable of supporting a sustainable energy transition.

1.2. SUMMARY OF OFFSHORE NEAR-SURFACE GEOPHYSICAL METHODS

Several methods can help us image and characterise the shallow subsurface. Broadly speaking, they fall under two categories : invasive and non-invasive. Invasive methods are more difficult to perform in a marine setting as access to the seafloor is limited. They may include drilling to extract core samples and Cone-Penetration-Tests (CPTs) where a cone-shaped probe is pushed into the seabed to measure soil resistance, pore pressure, and shear strength [26]. These measurements are discrete, but the conversion process to obtain soil parametres is precise since they provide low measurement uncertainty, and the theoretical interpretation model is directly linked to fundamental soil mechanics [27], [28]. However, invasive measurements only provide discrete information about the subsurface parametres and provide limited information regarding lateral subsurface variability [29]. Additionally, although poorly reported in the literature, the presence of boulders, gravel, or hard inclusions can prematurely terminate penetration and sometimes cause equipment damage. For this reason, CPT providers may opt to perform non-invasive geophysical surveys before selecting the CPT measurement locations.

Non-invasive geophysical methods infer the properties of subsurface formations without direct physical alteration to the seabed or subsurface. These methods are therefore of particular interest in the offshore environment because they allow for continuous, spatially extensive characterization of the subsurface in a cost-effective and minimally disruptive manner. Key techniques include seismic methods using passive or active sources, such as Ocean Bottom Nodes (OBNs) or Ocean Bottom Cables (OBCs), and towed-streamer seismics; side-scan and multi-beam sonar; magnetic and gravity surveys; Controlled-Source Electromagnetics (CSEM); and SubBottom Profiling (SBP). [30]. Note that in the case of OBCs and OBNs, although there is direct contact with the seafloor, no alteration to the subsurface is made.

Near-Surface Method	Measurand	Penetration Depth	Vertical Resolution	Derived Parametres	Relative cost	Applications
Ocean Bottom Node/Cable (OBN/C)	3-component elastic wavefield	>1 km	0.5 - 10 m	P and S-wave velocities, layer reflectivity	$$$$	Seismic imaging, site characterization, soil properties mapping
Towed-streamer seismics	Acoustic ~1Hz to 10kHz	>1 km	0.5 - 10 m	P-wave velocities, layer reflectivity	$$$	Seismic imaging, site characterization
SubBottom Profiler (SBP)	Acoustic ~10kHz to 100kHz	<80 m	0.1 - 1 m	Layer reflectivity	$$	Sediment stratigraphy, buried object detection
Side-Scan / Multibeam Sonar	Acoustic ~100kHz to 1MHz	<10 m	1 - 20 cm	Layer reflectivity, bathymetry	$$	Seafloor mapping, pipeline routing, archeology
Gravity	Gravitational field	∞	n/a	Local gravitational variations	$$	Hydrocarbon detection, CO_2 leakage monitoring
Ground Penetrating Radar (GPR)	Microwave electromagnetic radiation	<30 m	2 - 50 cm	Layer reflectivity	$	Concrete scanning, utility locating, archeology
Controlled Source Electromagnetic (CSEM)	Electromagnetic field response	>1 km	10 - 300 m	Electric resistivity	$$	Overburden characterization, CO_2 leakage monitoring
Magnetometry	Local magnetic field variations	<50 m	n/a	Magnetic force	$	UxOs, ferromagnetic objects

TABLE 1.1. – *Comparison of common non-invasive geophysical techniques for different offshore near-surface applications. The data presented in this table is compiled from [9], [30]-[34].*

Table 1.1 compares key characteristics of these techniques. Each is employed for a specific purpose based on the application for geological, geotechnical, or environmental investigation and monitoring. They can be combined in multiphysical schemes that aim to simultaneously invert multiple non-invasive geophysical datasets, also known as joint-inversion schemes [35], [36]. A prime example is the integration of electromagnetic and seismic data, where the strong correlation between electromagnetic resistivity and seismic velocities allows for the direct inversion of petrophysical properties such as porosity and fluid saturation [37]. Joint inversion schemes for near-surface applications are similarly becoming more robust, although the smaller projects and limited budgets reduce the opportunities to carry out multiple concurrent surveys [38], [39]. Also of note is that constraining the inversion of continuous methods with point-wise measurements like CPTs, magnetometry, or gravitational data provides robust characterization of specific targets like UxOs [21], [22] or to improve the convergence of optimization schemes towards the global minimum [29].

1.3. COMPARISON OF NON-INVASIVE MECHANICAL WAVEFIELDS METHODS

Mechanical wavefield methods play a significant role in offshore near-surface exploration, whether applied standalone or in joint-inversion schemes. They are currently the only non-invasive approach capable of producing detailed continuous images of subsurface stratigraphy at significant penetration depths. According to a PGS release [40], when building wind farm ground models, an initial "reconnaissance" 2D survey is performed and subsequently interpolated into a crude 3D model. The reconnaissance helps in defining the locations for acquiring additional geophysical data, and the measured soil and geotechnical parametres are integrated into the 3D models to fine-tune them and create a more complete image of the subsurface.

As illustrated in Table 1.1 and Figure 1.2, these surveys can be classified into High-Resolution (HR) seismics, Ultra-High Resolution (UHR) seismics, and Sub-Bottom Profiling (SBP). Frequency ranges vary across literature and industry practices, and some groups propose further subdivisions, such as Ultra-Ultra High Resolution (UUHR). However, given the similarities in hardware, acquisition methods, and processing techniques between UHR and UUHR seismics, we argue that further subdivision of the UHR category is unnecessary. HR seismics are traditionally used for standard exploration tasks but also play a critical role in monitoring CCS applications in depleted

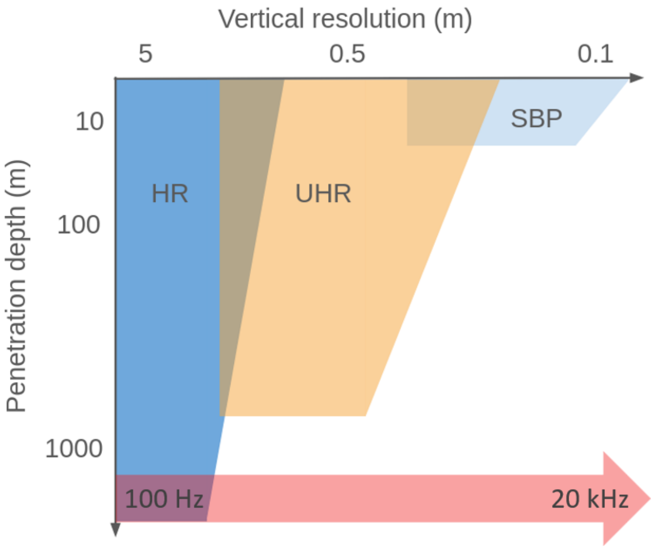

FIGURE 1.2. – *Comparison of the penetration depth and vertical resolution trade-off with representative frequencies for HR seismics (50-500 Hz), UHR seismics(100-5000 Hz), and SBP methods (>1000 Hz).*

offshore reservoirs [41], [42]. In the event of a CO_2 leak, the gas would migrate toward the surface, where UHR seismics combined with CSEM methods can help detect the plume front [43]. UHR seismics are also the primary tool for wind farm site investigations and monitoring, as well as geotechnical and offshore infrastructure projects requiring detailed subsurface imaging [44]. Lastly, sonar and SBP are primarily used for very shallow investigations, but because they only produce zero-offset reflection data, they are unsuitable for detailed characterization tasks.

We have chosen to focus on UHR seismic methods as they are on the frontier of established technologies. In this context, UHR seismics fill the gap by providing high-resolution near-surface imaging with significant penetration and information from offsets. Seismic methods have been used for decades yet direct translation of these to a higher frequency range is not a 1 :1 transition. As we will discuss throughout this thesis, state-of-the-art industry methods fall short for UHR seismics, both on the acquisition and processing fronts.

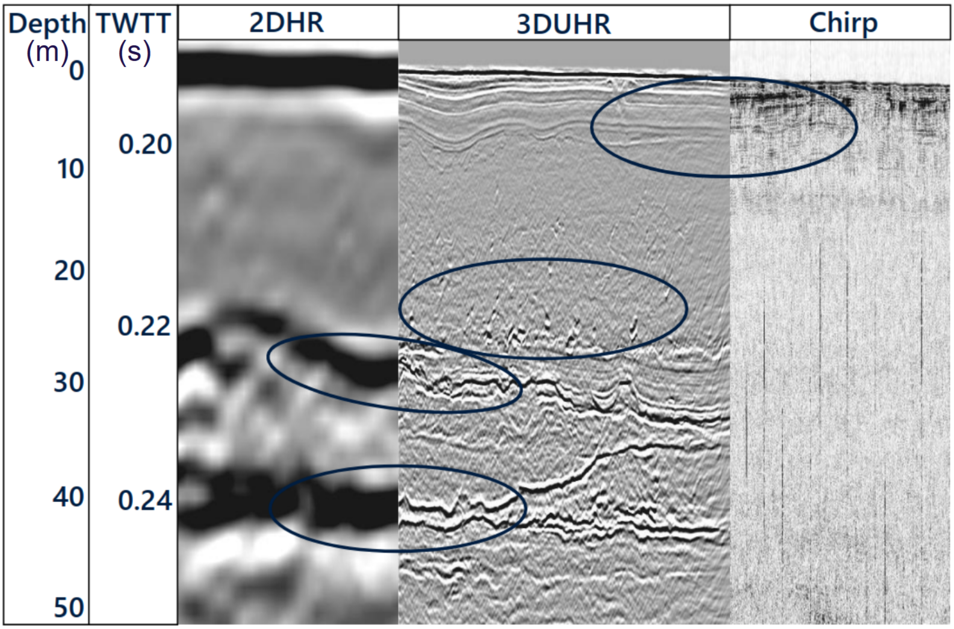

FIGURE 1.3. – *Figure released on a presentation from Fugro [45] comparing the data resolution from 2D HR, UHR, and sonar surveys in the same area from 0 to 50 m of the subsurface. Depth axis is in meters and the Two-Way Travel-Time is in seconds. Highlighted areas point to the improvement in imaging small-scale features by using higher resolution methods.*

1.4. OVERVIEW OF SEISMIC METHODS

Seismic methods refer to a set of techniques where mechanical wavefields that have propagated through the subsurface are recorded and analyzed to infer the properties and geometries of the layered media they have travelled through. The wavefields can occur naturally to varying degrees of amplitudes, like from earthquakes or from the vibrations from passing trains. They can also be artificially designed using "sources" that can take the form of a hammer on a plate or a controlled explosive. In the case of offshore acquisition, airguns, sparkers, boomers or marine vibrators are typically used. Airguns produce lower frequency signals whereas sparkers and boomers are used to obtain higher frequency and, therefore, higher resolution data. Marine vibrators produce a frequency swept signal similar to an onshore vibroseis and are less commonly utilized than the three aforementioned [46]. The seismic waves are recorded using geophone arrays (or hydrophones in water). They produce typical seismic datasets containing a "shot record" : the wavefield emanating from the same source recorded over time by multiple geophones at different locations. This data can subsequently be used to produce images and map parametres in the subsurface.

There are two modes in which the seismic waves propagate through the subsurface : as compressional waves and as shear waves. Shear waves (or S-waves), where the medium displacement is perpendicular to the direction of propagation, only propagate through solids. At the interface with air or water, S-waves can combine with compressional waves and create surface waves, including Love and Rayleigh waves. Shear wave propagation depends on the subsurface's elastic parametres that can be used to derive material properties like the bulk density, which is the mass per unit volume including the pore volume; the shear modulus, which is the ratio of shear stress to shear strain; and Poisson's ratio, which is the ratio of transverse strain to axial strain. Compressional waves (or P-waves), where the medium displacement is parallel to the direction of propagation, can travel through and be recorded in all media, including gases and liquids. For example, the sound produced by a tree falling in a forest is carried by P-waves, even if no one is around to hear it; and when the tree hits the ground, a combination of P- and S-waves will be produced, even if no one is around to feel them.

The speed at which a wavefield propagates from its source to the geophone varies depending on the medium it traverses. For example, a P-wave will propagate at around 1500m/s through water, a velocity that will vary depending on water temperature and salinity. With a constant speed, the wavefield will not deviate from its path, propagating in a constant direction and, therefore, at a constant velocity. If the wavefield encounters a boundary where material properties change, it will be transmitted, reflected, refracted, or diffracted. By recording the seismic waves and measuring the travel times between the source and the receiver array, analysing amplitude variations, phase shifts, and frequency content, it is possible to reconstruct an image of subsurface reflectors and diffractors in a process called imaging, as well as derive the seismic velocities of these layers using velocity inversion methods [47].

These models are created with a level of uncertainty. In a nutshell, the velocity inversion method, just like all inversion methods, looks for a solution where the residual between the recorded seismic data and the model is minimized. This solution is non-unique and exists in a solution space that contains multiple local minima. Finding the global minimum in this solution space, aka the true solution, can not be done with a complete level of certainty. Similarly, this imperfect velocity estimate is required to produce an image of subsurface reflectors. If the velocities are poorly constrained, the reflectors will be placed at an incorrect depth in the image to account for the measured arrival travel-time. The fields of seismic imaging and inversion are, therefore, continually innovating to improve the certainty and accuracy of subsurface models. Advanced algorithms incorporate additional data constraints and leverage machine learning techniques to reduce uncertainties and improve resolution [44]. Despite these advancements, challenges remain due to factors such as noise in the recorded data, limited acquisition coverage, and the inherent non-uniqueness of the inversion process [29]. Consequently, seismic methods continue to evolve, integrating new technologies and methodologies to refine our understanding of Earth's subsurface structures, including in the near-surface.

1.5. DEFINING THE INTENT OF THIS RESEARCH

In this thesis, we attempt to provide new insights and solutions into the dilemmas of seismic methods in an offshore near-surface context. To this end, we focus on the upper 100 m of the subsurface, tackling both inversion and imaging methods as well as improving the quality of seismic data during the acquisition via accurate measurements of hydrophone positions.

The main research questions that we focus on are :

1. *What characteristics of the offshore near-surface seismic data pose a challenge when performing seismic velocity inversion using state-of-the-art methods?*
2. *What techniques improve velocity-model building of the offshore near-surface, where methods used in exploration seismics fall short?*
3. *How can the quality of near-surface data be improved during acquisition to mitigate some of the challenges with offshore near-surface data processing?*
4. *Can existing shape sensing technologies be applied to UHR streamers to improve the positioning of hydrophones in the water?*

In **Chapter 2**, we discuss the applicability of reflection and refraction seismic methods to near-surface seismic velocity inversion and encounter the challenges of dealing with offshore near-surface data. We propose a workflow of Joint-Migration-Inversion (JMI), based on reflection tomography, and Full-Waveform-Inversion (FWI) that sequentially harnesses the strengths of each method to improve the velocity model and reflection image, using synthetic data.

In **Chapter 3**, we apply the proposed workflow to seismic data from a wind farm site in the Dutch North Sea. Although the synthetic datasets used in Chapter 2 were designed to reflect typical offshore near-surface acquisition, we observe firsthand the effects of data quality and acquisition design on the inversion process. Nonetheless, we demonstrate the efficacy of using JMI methods to improve estimates of the acoustic velocity model.

In **Chapter 4**, we take a detour to look at a technical constraint that can severely negatively affect the data quality during a near-surface seismic survey. Specifically, the limitations in streamer design as hardware have typically been "scaled down" from exploration geophysics to be applied to the near-surface surveys. A victim of this transition are the positioning methods that currently fail to accurately record the positions of hydrophones in the water during the survey. We discuss the effects of poor receiver positioning for near-surface data and the community's call to improve existing methods.

In **Chapter 5**, we propose to use so-called Fiber-Optic Shape Sensing (FOSS) to monitor the shape of seismic streamers used during acquisition and solve the hydrophone positioning limitations discussed in Chapter 4. We explore the basic theory of FOSS and describe the procedures and considerations involved in the process of deployment and the steps required for reliable and repeatable measurements. We go in-depth on the guidelines we have established to design a shape-sensor specifically to serve implementations in the geotechnical and geophysical industries, from the interrogator technology to the sensor geometry, mentioning the importance of a central core, embedding, and options for the reconstructed shape in 3D-space.

In **Chapter 6**, we present the first developments in testing the possibility of using FOSS for streamer shape reconstruction. Our work involves the design of a dedicated sensor and embedding sleeve, developed through bench experimentation and numerical modelling. We then deploy these elements in a flume in a series of experiments that utilise FOSS and streamer data in a controlled environment.

Finally, in **Chapter 7**, we discuss the outlook of the work presented in this thesis. We look at the realistic application potential of JMI in the industry for near-surface offshore data. Furthermore, we discuss the value of long-distance

FOSS sensors in geotechnical fields and the practical issues that must still be tackled.

With this thesis, we aim to contribute to both the scientific and applied geophysical community by addressing two longstanding challenges : (1) the accuracy and reliability of velocity model building in the complex near-surface, and (2) the precision of hydrophone positioning during acquisition. The proposed innovations aim to improve offshore engineering safety, reduce project risk, and advance sustainable use of the marine environment.

RÉFÉRENCES

[1] Y. XIE, Y. YE, X. HUANG, W. SUN et Y. WEI, « Advancements and new frontiers in offshore seismic exploration technology », *Journal of Earth Science*, t. 35, nº 5, p. 1749-1757, oct. 2024, ISSN : 1867-111X. DOI : `10.1007/s12583-024-0075-3`. adresse : `https://doi.org/10.1007/s12583-024-0075-3`.

[2] NETHERLANDS ENTERPRISE AGENCY (RVO), *Operational wind farms in the Netherlands : Offshore wind energy*, `https://english.rvo.nl/topics/offshore-wind-energy/operational-wind-farms`, Accessed : 2024-11-25, 2024.

[3] NOORDZEELOKET, *Energy transition and the North Sea : Offshore wind energy*, `https://www.noordzeeloket.nl/en/functions-and-use/offshore-wind-energy/energy-transition-north-sea/`, Accessed : 2024-11-25, 2024.

[4] O. MONRIGAL, I. D. JONG et H. DUARTE, « An ultra-high-resolution 3D marine seismic system for detailed site investigation », *Near Surface Geophysics*, t. 15, nº 4, p. 335-345, août 2017. DOI : `10.3997/1873-0604.2017025`.

[5] R. BRUNE, J. HABERKERN, S. WENAU et B. PREU, « Ultra-High-Resolution Marine Seismic Survey for Wind Farm Site Characterization in the German North Sea », in *83rd EAGE Annual Conference and Exhibition*, Madrid, Spain / Online : European Association of Geoscientists et Engineers, 2022, p. 1-5. DOI : `10.3997/2214-4609.202210674`.

[6] H. DUARTE, N. WARDELL et O. MONRIGAL, « Advanced processing for UHR3D shallow marine seismic surveys », *Near Surface Geophysics*, t. 15, nº 4, p. 347-358, août 2017. DOI : `10.3997/1873-0604.2017022`.

[7] A. HOLEYMAN *et al.*, « Boulder-Soil-Pile Dynamic Interaction », in *Frontiers in Offshore Geotechnics III*, 2015, ISBN : 978-1-138-02848-7.

[8] T. ALDRIDGE *et al.*, « BP Clair Phase 1 - Pile Driveability and Capacity in Extremely Hard Till », in *Frontiers in Offshore Geotechnics II*, 2010, ISBN : 978-0-415-58480-7.

[9] GEOEXPRO. « Marine Site Investigation and Reducing Risk ». Accessed : 2024-11-26. (2024), adresse : https://geoexpro.com/marine-site-investigation-and-reducing-risk/.

[10] M. of INFRASTRUCTURE, W. MANAGEMENT et other responsible MINISTRIES, *North Sea Programme 2022–2027*, https://www.noordzeeloket.nl/publish/pages/201299/north-sea-programme-2022-2027.pdf, Accessed : 2025-10-24, 2022.

[11] TNO — NETHERLANDS ORGANISATION FOR APPLIED SCIENTIFIC RESEARCH. « New seabed sediment map for improved North Sea management ». Accessed : 2025-10-24. (2023), adresse : https://www.tno.nl/en/newsroom/insights/2023/05/map-seabed-sediment-northsea/.

[12] DIGITAL NORTH SEA, *Maritime Information Provision Service Point*, https://www.digitalnorthsea.nl/topics/m/maritime-information-service-point, Accessed : 20-09-2025, n.d.

[13] P. ROUTH, R. NEELAMANI, R. LU, S. LAZARATOS, H. BRAAKSMA, S. HUGHES, R. SALTZER, J. STEWART, K. NAIDU, H. AVERILL, V. GOTTUMUKKULA, P. HOMONKO, J. REILLY et D. LESLIE, « Impact of high-resolution FWI in the Western Black Sea : Revealing overburden and reservoir complexity », *The Leading Edge*, t. 36, n^{o} 1, p. 60-66, 2017. DOI : 10.1190/tle36010060.1. eprint : https://doi.org/10.1190/tle36010060.1. adresse : https://doi.org/10.1190/tle36010060.1.

[14] S. AL MESAABI, M. MAHGOUB, A. LEVEQUE, G. POPA, H. HAGIWARA et K. OBAID, « Impact of near surface topography on seismic imaging and reservoir characterization of deep targets - a case study from onshore Abu Dhabi », in *International Geophysical Conference and Oil & Gas Exhibition, Istanbul, Turkey, 17-19 September 2012*. 2013, p. 1-4. DOI : 10.1190/IST092012-001.11. eprint : https://library.seg.org/doi/pdf/10.1190/IST092012-001.11. adresse : https://library.seg.org/doi/abs/10.1190/IST092012-001.11.

[15] OFFSHORE ENERGY, *NCS Subsea Completes 4D Seismic Survey in US Gulf of Mexico*, https://www.offshore-energy.biz/ncs-subsea-completes-4d-seismic-survey-in-us-gulf-of-mexico/, Accessed : 2024-11-26, 2024.

[16] N. SKOPLJAK, « Denmark's CO_2 storage pilot project paves the way for large-scale CCS », *Offshore Energy*, 2024.

[17] P. C. TRANSPORT et S. C.V. « Project — Porthos CO_2 ». Accessed : 2025-10-24. (2023), adresse : https://www.porthosco2.nl/en/project/.

[18] R. /. NOORDZEELOKET. « Porthos gaat van start, het eerste grote project voor CO_2-opslag in Nederland ». Accessed : 2025-10-24. (2023), adresse : https://noordzeeloket.nl/beleid/interdepartementaal-directeuren-overleg-noordzee/idon-nieuwsbrief/nr-44/porthos-gaat-start-eerste-grote-project-co2-opslag/.

[19] A. E. A. BLOMBERG, I.-K. WAARUM, C. TOTLAND et E. EEK, « Marine Monitoring for Offshore Geological Carbon Storage—A Review of Strategies, Technologies and Trends », *Geosciences*, t. 11, n° 9, 2021, ISSN : 2076-3263. DOI : `10.3390/geosciences11090383`. adresse : `https://www.mdpi.com/2076-3263/11/9/383`.

[20] B. HOWARD, J. AKER et M. REID, « Risk Management for Unexploded Ordnance (UxO) in the Marine Environment », *Dalhousie Journal of Interdisciplinary Management*, t. 8, n° 2, 2012. DOI : `10.5931/djim.v8i2.366`. adresse : `https://doi.org/10.5931/djim.v8i2.366`.

[21] R. MORROW, M. VARDY, R. HAMILTON, J. DIX, T. HENSTOCK et L. PINSON, « UxO Characterization by 3D Seismic Constrained Magnetometry Inversion », t. 2014, n° 1, p. 1-5, 2014, ISSN : 2214-4609. DOI : `https://doi.org/10.3997/2214-4609.20142146`. adresse : `https://www.earthdoc.org/content/papers/10.3997/2214-4609.20142146`.

[22] S. M. ABBOTT *et al.*, « Combining High Resolution Seismic Sub-Bottom Imagery with Magnetometer Data to Identify Potential UxOs : A Case Study off the Danish Coast », *Atlantic Geoscience*, t. 58, p. 47, 2022, Accessed : 2024-11-27. adresse : `https://link.gale.com/apps/doc/A716577007/HRCA?u=anon~dec31f48&sid=googleScholar&xid=aef52ec4`.

[23] A. GOH, « South Korea is designing a 'flood-proof' city that can house 12,000 people and looks like a giant, floating honeycomb — take a look », *Business insider*, 2022.

[24] H.-Y. LEE, K.-P. PARK, N.-H. KOO, D.-G. YOO, D.-H. KANG, Y.-G. KIM, K.-D. HWANG et J.-C. KIM, « High-resolution shallow marine seismic surveys off Busan and Pohang, Korea, using a small-scale multichannel system », *Journal of Applied Geophysics*, t. 56, n° 1, p. 1-15, 2004, ISSN : 0926-9851. DOI : `https://doi.org/10.1016/j.jappgeo.2004.03.003`. adresse : `https://www.sciencedirect.com/science/article/pii/S0926985104000096`.

[25] G. S. BHARGAVI, J. N. CHAITANYA, DR.K.CHANDRAMOULI et M. C. N. KUMAR, « Study on Future Floating Cities », *International Journal for Modern Trends in Science and Technology*, t. 7, p. 93-98, juill. 2021. DOI : `10.46501/IJMTST0707016`.

[26] X. LEI, Z. ZHANG, Z. LI, J. LAO, Y. LI et C. HU, « Application of Cone Penetration Testing (CPT) in Site Investigation for Wind Farm Development : Predicting Soil Properties Using Advanced Machine Learning Techniques », sér. International Ocean and Polar Engineering Conference, t. All Days, juin 2024, ISOPE-I-24-227. eprint : `https://onepetro.org/ISOPEIOPEC/proceedings-pdf/ISOPE24/All-ISOPE24/ISOPE-I-24-227/3416291/isope-i-24-227.pdf`.

[27] J. PEUCHEN et J. TERWIND, *Introduction to CPT accuracy*, `https://www.g-i.co.nz/wp-content/uploads/introduction-to-cpt-accuracy-fugro.pdf`, Online presentation, 2012.

[28] Y. Lu, H. Zhang, X. Zhang, S. Zheng et Y. Wu, « Offshore Cone Penetration Test and Its Application in Full Water-Depth Geological Surveys », in *IOP Conference Series : Earth and Environmental Science*, t. 570, IOP Publishing, 2020, p. 042 008. DOI : 10.1088/1755-1315/570/4/042008. adresse : https://iopscience.iop.org/article/10.1088/1755-1315/570/4/042008/pdf.

[29] M. E. Vardy, M. A. Clare, M. Vanneste, C. F. Forsberg et J. K. Dix, « Seismic Inversion for Site Characterization : When, Where and Why Should We Use It ? », sér. OTC Offshore Technology Conference, t. Day 2 Tue, May 01, 2018, avr. 2018, D021S027R005. DOI : 10.4043/28730-MS. eprint : https://onepetro.org/OTCONF/proceedings-pdf/18OTC/2-18OTC/D021S027R005/1193694/otc-28730-ms.pdf. adresse : https://doi.org/10.4043/28730-MS.

[30] C.-C. Tsai et C.-H. Lin, « Review and Future Perspective of Geophysical Methods Applied in Nearshore Site Characterization », *Journal of Marine Science and Engineering*, t. 10, n° 3, 2022, ISSN : 2077-1312. DOI : 10.3390/jmse10030344. adresse : https://www.mdpi.com/2077-1312/10/3/344.

[31] C. Chen et Y. Tian, « Comprehensive Application of Multi-beam Sounding System and Side-scan Sonar in Scouring Detection of Underwater Structures in Offshore Wind Farms », *IOP Conf. Ser. : Earth Environ. Sci.*, t. 668, p. 012 007, 2021. DOI : 10.1088/1755-1315/668/1/012007.

[32] M. Wilkinson, J. Mouli-Castillo, P. Morgan et R. Eid, « Time-lapse gravity surveying as a monitoring tool for CO_2 storage », *International Journal of Greenhouse Gas Control*, t. 60, p. 93-99, 2017, ISSN : 1750-5836. DOI : https://doi.org/10.1016/j.ijggc.2017.03.006. adresse : https://www.sciencedirect.com/science/article/pii/S1750583616303310.

[33] S. Vakulenko, A. Ponimaskin, M. Tokarev, S. Gorbachev et L. Gurvich, « MASW Application for Near-Surface Site Characterization of 2D/3D OBN Seismic Survey on Pechora Sea Shelf », t. 2021, n° 1, p. 1-9, 2021, ISSN : 2214-4609. DOI : https://doi.org/10.3997/2214-4609.202152188. adresse : https://www.earthdoc.org/content/papers/10.3997/2214-4609.202152188.

[34] S. Hou, D. Zheng, X. Miao et R. Haacke, « Multi-modal Surface Wave Inversion and Application to North Sea OBN Data », t. 2016, n° 1, p. 1-5, 2016, ISSN : 2214-4609. DOI : https://doi.org/10.3997/2214-4609.201601364. adresse : https://www.earthdoc.org/content/papers/10.3997/2214-4609.201601364.

[35] L. A. Gallardo, S. L. Fontes, M. A. Meju, M. P. Buonora et P. P. de Lugao, « Robust geophysical integration through structure-coupled joint inversion and multispectral fusion of seismic reflection, magnetotelluric, magnetic, and gravity images : Example from Santos Basin, offshore Brazil », *GEOPHYSICS*, t. 77, n° 5, B237-B251, 2012. DOI : 10.1190/geo2011-0394.1. eprint : https://doi.org/10.1190/geo2011-0394.1. adresse : https://doi.org/10.1190/geo2011-0394.1.

[36] D. COLOMBO et D. ROVETTA, « Coupling strategies in multiparameter geophysical joint inversion », *Geophysical Journal International*, t. 215, n° 2, p. 1171-1184, août 2018, ISSN : 0956-540X. DOI : 10.1093/gji/ggy341. eprint : https://academic.oup.com/gji/article-pdf/215/2/1171/39576594/ggy341.pdf. adresse : https://doi.org/10.1093/gji/ggy341.

[37] A. ABUBAKAR, G. GAO, T. M. HABASHY et J. LIU, « Joint inversion approaches for geophysical electromagnetic and elastic full-waveform data », *Inverse Problems*, t. 28, n° 5, p. 055016, avr. 2012. DOI : 10.1088/0266-5611/28/5/055016. adresse : https://dx.doi.org/10.1088/0266-5611/28/5/055016.

[38] A. B. KARPIAH, M. A. MEJU, R. L. MACKIE, A. A. AZIZ et M. MUSA, « Use of 3D cross-gradient joint inversion of marine controlled-source electromagnetic and seismic refraction data for overburden geohazard mapping », *Geophysics*, 2023. DOI : 10.1190/geo2023-0398.1.

[39] Z. SHI et C. WANG, « Near-surface imaging by joint inversion of ERT and seismic traveltime data with guided FCM clustering », *Journal of Applied Geophysics*, t. 222, p. 105 332, 2024, ISSN : 0926-9851. DOI : https://doi.org/10.1016/j.jappgeo.2024.105332. adresse : https://www.sciencedirect.com/science/article/pii/S092698512400048X.

[40] A. LONG, « 3D ground model insights for offshore windfarm development », *A Clearer Image, PGS*, 2023.

[41] M. WIDMAIER, D. O'DOWD et C. DELARUE, « Strategies for High Resolution Towed-Streamer Acquisition and Imaging of Shallow Targets », in *87th Annual Meeting, Society of Exploration Geophysicists (SEG) Expanded Abstracts*, Spectral bandwidth reported as 2–200 Hz, SEG, 2017. adresse : https://www.tgs.com/hubfs/Technical%20Library/Technical%20Library%20Files/seg2017_widmaier_etal_shallowtargets.pdf.

[42] T. A. MECKEL, Y. E. FENG, R. H. TREVIÑO et D. SAVA, « High-resolution 3D marine seismic acquisition in the overburden at the Tomakomai CO_2 storage project, offshore Hokkaido, Japan », *International Journal of Greenhouse Gas Control*, t. 88, p. 124-133, 2019. DOI : 10.1016/j.ijggc.2019.05.034. adresse : https://www.sciencedirect.com/science/article/abs/pii/S1750583618309289.

[43] M. FAWAD et N. H. MONDOL, « Monitoring geological storage of CO_2 : a new approach », *Scientific Reports*, t. 11, n° 1, p. 5942, 2021. DOI : 10.1038/s41598-021-85346-8. adresse : https://doi.org/10.1038/s41598-021-85346-8.

[44] CASELITZ, A. MCKAY, M. WIDMAIER, J. OUKILI, D. DAVIES et N. PERNIN, « Harnessing 3D Ultra-High-Resolution Seismic Technology for Offshore Wind Farm Development : Advancements, Challenges, and Future Prospects », *The Leading Edge*, t. 44, n° 3, 2025. DOI : 10.1190/tle44030170.1. adresse : https://www.tgs.com/hubfs/2025%20Articles/caselitz-et-al-2025-harnessing-3d-ultra-high-resolution-seismic-technology-for-offshore-wind-farm-development.pdf.

[45] S. OAKLEY, « Sub-seabed boulder detection using 3DUHR Seismic Data », 2021, Online presentation.

[46] C. D. RUPPEL, T. C. WEBER, E. R. STAATERMAN, S. J. LABAK et P. E. HART, « Categorizing Active Marine Acoustic Sources Based on Their Potential to Affect Marine Animals », *Journal of Marine Science and Engineering*, t. 10, n^{o} 9, 2022, ISSN : 2077-1312. DOI : `10.3390/jmse10091278`. adresse : `https://www.mdpi.com/2077-1312/10/9/1278`.

[47] B. BIONDI, « 3-D Seismic Imaging », jan. 2006. DOI : `10.1190/1.9781560801689`.

2

JMI AND FWI WORKFLOW: THEORY AND SYNTHETIC EXAMPLES

To improve the imaging and characterization of the near-surface, we begin the research by looking at existing inversion methods of seismic data and evaluating their benefits and drawbacks.

In this chapter, we implement a workflow of Joint-Migration Inversion and Full Waveform Inversion to improve the final reflectivity images and seismic velocity estimates on synthetic datasets.

2.1. INTRODUCTION

In geophysics, inversion is the process of using data to estimate the physical properties of the medium characterised by the recorded data. When using seismic data, it is possible to invert for P- and S-wave velocities, as well as density, Poisson's ratio, and other elastic parameters. Seismic velocity inversion methods can be categorized into seismic refraction methods, seismic reflection methods, and transmitted waves methods. Seismic reflection methods involve computing the round-trip travel time of a seismic wave from a source, via a subsurface reflection layer, to a receiver to gain velocity information of the layers the acoustic energy travelled through, and therewith the location of interfaces. Refraction seismics, on the other hand, makes use of the multi-pathing nature of seismic energy at farther offsets through layers of varying velocities to compute the difference between paths. This is detectable from refracted head-waves that occur when a seismic wave encounters a higher velocity layer below a lower velocity layer. At the critical angle, the wave travels along the interface between the layers (guided by the faster medium), and continually radiates energy back up to the surface at the critical angle. The critical angle is dictated by Snell's law, which describes when a wavefield will reflect or refract based on the angle of incidence and the refraction index. Snell's law can be described as

$$\frac{sin\theta_1}{v1} = \frac{sin\theta_2}{v2} \quad \text{and} \quad \theta_c = arcsin(\frac{v1}{v2}) \tag{2.1}$$

where $\theta_1$and θ_2 are the angles of incidence and refraction in media 1 and 2 respectively, and θ_c is the critical angle computed when $\theta_2 = 90^o$ in medium with velocities v_1 and v_2, as shown in Figure 2.1. Special kinds of refracted waves are so-called "diving-waves" that occur when the velocity increases with depth, forcing the wavefront to continuously refract, eventually turning back towards the surface. Diving waves are an example of transmitted waves where part of the seismic wave energy continues through the boundary into the next layer, without bouncing back. Unlike refraction's critical-angle phenomenon, transmission occurs for all incident angles below the critical angle. Transmitted waves are, for example, utilised in surface-wave inversion and in first-break tomography, where direct and refracted body waves are combined to recover subsurface velocity models.

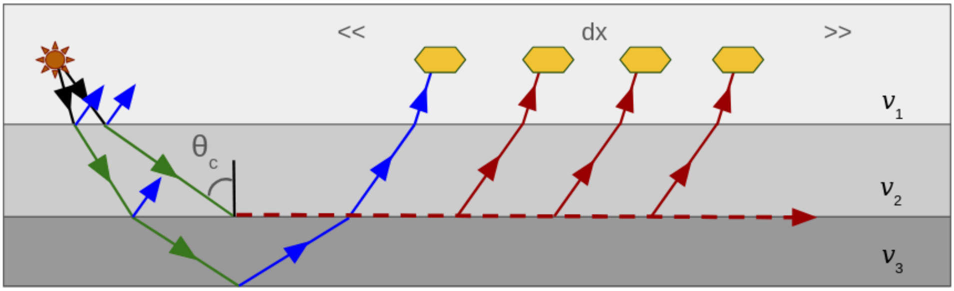

FIGURE 2.1. – *Conceptual drawing showing reflected seismic waves (blue arrows), transmitted refracted seismic waves (green arrows), and refracted seismic head waves (red arrows) at the critical angle of incidence θ_c from the source (yellow star) to the receiver array (yellow polygons).*

In this chapter, we focus on reflection and refraction methods, which will be used for velocity inversion. A basic principle that governs both reflection and refraction seismic inversion is that by increasing the number of sources and receivers, as well as the range of offsets and frequencies, an increasingly accurate image of the subsurface can be constructed. Naturally, during real-world seismic surveys, time and costs limit the reach of this principle. To improve imaging and inversion results of offshore near-surface seismic data, with no prior knowledge, we must resort to improving processing and inversion strategies. To this end, we propose a workflow of Joint Migration Inversion (JMI), Full Waveform Inversion (FWI), and Full Wavefield Migration (FWM).

2.2. MOTIVATION

In field UHR seismic applications, both S-wave and P-wave velocities are of interest. The shear information that can be related to and interpolated from point measurements called Cone Penetration Tests (CPTs) and give information about subsurface physical characteristics like density, Poisson's ratio and stiffness [1]. These parameters are useful to understand how the subsurface will react to different piling methods. P-wave information is typically used for structural imaging, which is important to discern the structural depth of specific hard layers as well as lateral variability and hazard detection, like boulders. In unconsolidated shallow sediments, P-wave velocity can also be strongly correlated to with stiffness and effective stress, allowing P-wave velocities to serve as a practical proxy for geotechnical parameters when calibrated against CPT or borehole measurements [2]. The higher propagation velocity of P-waves also lead to shorter wavelength that can sample smaller structures, increasing the fidelity in the reflection imaging. Approaches to recover density and Poisson's ratio have been demonstrated on UHR reflection data for the 1.5D case under the assumption of lateral homogeneity, where the scale of layering is small compared with the streamer aperture (e.g., elastic 1D inversion strategies such as those presented by Provenzano et al., 2017, 2018 [3]). These approaches explicitly target elastic parameters and are particularly suited to settings where lateral variability is limited and the data response can be approximated as locally one-dimensional. For these reasons, this work adopts an acoustic approximation within the FWI framework. This choice is not intended to imply that elastic properties are unimportant, but rather to focus on imaging positioning accuracy of small-scale structures and hazard.

To derive the P-wave propagation velocities and improve reflectivity imaging, we propose a FWI workflow conditioned by a JMI starting velocity model.

FWI is well-suited for high-resolution velocity estimation as it produces a set of solutions with a resolution equal to half of the propagated source wavelength [4]. Resolution, in this case, can be described as the minimum spatial separation between two perturbations that can be distinguished in the reconstructed model. For example, with a maximum frequency of 1000 Hz, the solution will have a resolution of 75 cm in water with a propagation speed of 1500 m/s. Its data-driven approach reaches a solution that most closely resembles the seismic data in a locally optimised manner. However, the least-squares error function may converge towards a mathematical local minimum due to the lack of low frequencies in the dataset and the low precision of the starting model. The refraction-based FWI method also struggles when the dataset lacks far-offsets and therefore contains mainly reflection data, which can be a feature of near-surface marine data with short acquisition streamers [5].

To improve the convergence of Full Waveform Inversion (FWI), the industry standard calls for initial model-building methods, which have their respective advantages and drawbacks. Some sites may benefit from legacy conventional seismic models and borehole data that can be reprocessed to create a low-resolution initial velocity model [6]. Travel-time tomography of first arrivals is a simpler method that does not rely on legacy or well-log data; however, it is limited in its ability to recover complex velocity structures, especially in areas with sparse ray coverage or strong lateral heterogeneity [7], [8]. Finally, a recent trend in literature has been to use machine learning methods for initial model building, which have shown promising results in generating data-driven, geologically plausible velocity models that can help FWI avoid cycle skipping and converge more reliably toward the global minimum [9].

Instead, we propose to use JMI to build the initial velocity model for FWI [10], [11]. It uses the full wavefield and fully accounts for internal multiples, which are not treated as noise in the data, to invert the velocity model and perform seismic migration simultaneously. The recursive, iterative two-way modelling [12] produces a sharp, high-resolution reflectivity image and a smoother propagation velocity estimate [13]. The reflectivity image can be used to improve the velocity resolution during the iterative process by acting locally as a weight during the velocity update process [14]. The efficiency of JMI is optimised by using a multi-scale approach. It does not require additional information or a robust starting model to perform relatively well, but the final resolution of the velocity estimate is too low for it to be used on its own in this application. It is, however, a reliable, data-driven method to obtain a starting model for high-resolution FWI that does not depend on the presence of low frequencies in the data.

2.3. THEORY

2.3.1. FDM

Acoustic Finite-Difference Modeling (FDM) is the forward modelling method of FWI and was also used to create the synthetic datasets. The acoustic wave equation can describe the propagation of seismic waves through the subsurface, by modelling the pressure variations in a compressible medium. In two dimensions, the second-order acoustic wave equation is given as

$$\frac{\partial^2 p(x,z,t)}{\partial t^2} = c(x,z)^2 \left(\frac{\partial^2 p}{\partial x^2} + \frac{\partial^2 p}{\partial z^2} \right) + s(x,z,t), \tag{2.2}$$

where $p(x,z,t)$ is the acoustic pressure, $c(x,z)$ is the spatially varying wave velocity, and $s(x,z,t)$ is the seismic source. Alternatively, the wave equation can be formulated as a first-order hyperbolic system in terms of particle velocity $\mathbf{u} = (u_x, u_z)$, which is advantageous for the staggered-grid FDM engine described by Thorebecke [15], [16]

$$\frac{\partial \mathbf{u}}{\partial t} = -\frac{1}{\rho} \nabla p, \tag{2.3}$$

$$\frac{\partial p}{\partial t} = -\kappa \nabla \cdot \mathbf{u} + s(\mathbf{x}, t), \tag{2.4}$$

where ρ is the density, κ is the compressibility (or the reciprocal of the bulk modulus), and ∇ is the spatial derivative. The spatial derivatives in these equations are approximated using combinations of Taylor expansions that form a stencil of 4 points around the point where the wavefield is derived. The spatial and temporal first order derivatives are approximated using the 2nd and 4th Crank-Nicolson approximation respectively [15] as

$$\frac{\partial P}{\partial t} \approx \frac{P((i+0.5)\Delta t) - P((i-0.5)\Delta t)}{\Delta t}, \tag{2.5}$$

$$\begin{aligned} \frac{\partial P}{\partial x} \approx & \frac{-P((i+1.5)\Delta x) + 27P((i+0.5)\Delta x)}{24\Delta x} \\ & - \frac{27P((i-0.5)\Delta x) - P((i-1.5)\Delta x)}{24\Delta x}. \end{aligned} \tag{2.6}$$

The modelling domain must therefore be discretized, which is done, in this case, using a staggered grid. The compressibility κ is constrained in terms of the P-wave velocity and density such that

$$\frac{1}{\kappa} = c_p^2 \rho. \tag{2.7}$$

Zero initial-conditions can be applied to ensure uniqueness, and, to simulate wave propagation in an open domain, absorbing boundary conditions are applied at the model edges to minimise artificial reflections. To summarize, this FDM engine takes the input of a velocity c_p and density ρ models to simulate the propagation of a wavefield from a source signature that is also provided.

2.3.2. FWI

Full-Waveform Inversion (FWI) is a high-resolution seismic imaging technique that aims to estimate subsurface parameters (e.g., acoustic velocity) by minimising the misfit between observed and simulated seismic wavefields. The process works in three major stages :

1. The forward modelling, where the source wavelet is propagated through an estimated velocity model to a set of receivers. This is done using the FDM forward engine.
2. The least-squares error computation, where the predicted (or modelled) receiver data is compared to the recorded receiver data.
3. The estimated velocity update, which is computed through a chosen optimisation scheme.

In this research, we implement the Devito framework where FWI is implemented through symbolic representation of partial differential equations, automatic differentiation, and optimised finite-difference operators [17], [18]. The least-squares function that is minimised iteratively compares the recorded data to the synthetically propagated source wavelet. It is defined as

$$\mathscr{J}(m) = \frac{1}{2}\sum_s \sum_r \int_0^T \left[d_{s,r}(t) - p_{s,r}(t;m)\right]^2 dt, \tag{2.8}$$

where $m(x)$ represents the spatially varying model parameters, which, in this case, is the squared slowness $m = 1/c_p^2$, $d_{s,r}(t)$ is is the recorded pressure data for source s at receiver location $\mathbf{x}_r$, and $p_{s,r}(\mathbf{x}_r, t; m)$ is the modelled pressure field using the current model m. The forward problem, which is the propagation of the source wavefield in the current model parameters, is done by discretizing the acoustic wave equation using finite differences

$$\frac{\partial^2 p}{\partial t^2} - m(\mathbf{x})\nabla^2 p = s(\mathbf{x}, t), \tag{2.9}$$

where ∇^2 is the Laplacian operator. Devito employs the adjoint-state method to compute the gradient of the objective function [19]. The adjoint wavefield $\lambda(\mathbf{x}, t)$ is obtained by solving the adjoint wave equation backward in time

$$\frac{\partial^2 \lambda}{\partial t^2} - m(\mathbf{x})\nabla^2 \lambda = r(\mathbf{x}, t), \tag{2.10}$$

where the adjoint source

$$r(\mathbf{x}_r, t) = p_{s,r}(\mathbf{x}, t; m) - d_{s,r}(t) \tag{2.11}$$

is the data residual injected at receiver locations. Then, the gradient of the objective function with respect to the model m is computed by correlating the time derivatives of the forward and adjoint pressure fields

$$\nabla \mathscr{J}(m)(\mathbf{x}) = -\int_0^T \frac{\partial p}{\partial t}(\mathbf{x}, \tau) \cdot \frac{\partial \lambda}{\partial t}(\mathbf{x}, t-\tau)\, d\tau, \tag{2.12}$$

Finally, the gradient can be passed to a chosen optimisation algorithm. In this chapter a simple steepest gradient descent scheme is applied the model is iteratively updated as

$$m^{k+1}(\mathbf{x}) = m^k(\mathbf{x}) - \alpha \nabla \mathscr{J}(m^k)(\mathbf{x}), \tag{2.13}$$

with α as a chosen step length chosen per iteration. In Chapter 3, the Gauss-Newton method is described to update the slowness model iteratively.

2.3.3. JMI

Full Wavefield Migration (FWM) and Joint Migration Inversion (JMI) [10], [20] are built on the Full Wavefield Modeling forward (FWMod) and reverse (FWMod^{-1}) propagation engines [12] which utilise the propagation operators ($\mathbf{W}^+$, $\mathbf{W}^-$) and scattering operators ($\mathbf{R}$, $\delta\mathbf{T}$) [21] to retrieve seismic measurements using source vector information or to retrieve source vector information using seismic measurements respectively. FWMod and FWMod^{-1} are recursively iterative and utilise the full wavefield, including multiples. In short, the forward model can be described by the following set of equations using the downgoing ($\vec{P}_j^+(z_m^-;z_0)$) and upgoing $\vec{P}_j^-(z_m^-;z_0)$ wavefields at depths $m = 0,1,2,...,M$ and $m = M-1, M-2,...,0$ respectively

$$\begin{aligned}\vec{P}_j^+(z_m^-;z_0) =& \mathbf{W}^+(z_m^-,z_0)\vec{S}_j^+(z_0)\\ &+\sum_{n=0}^{m-1}\mathbf{W}^-(z_m^-,z_n^+)\delta\vec{S}_j^+(z_n^+;z_0)\end{aligned} \tag{2.14}$$

and

$$\begin{aligned}\vec{P}_j^-(z_m^-;z_0) =& \mathbf{W}^-(z_m^+,z_M)\vec{P}_j^+(z_M;z_0)\\ &+\sum_{n=m+1}^{M}\mathbf{W}^-(z_m^+,z_n^-)\delta\vec{S}_j^-(z_n^-;z_0).\end{aligned} \tag{2.15}$$

Above, $\vec{S}_j^+(z_0)$ is the source term at depth $z = 0$. The down-going and up-going propagation operators, $\mathbf{W}^+$ and $\mathbf{W}^-$ respectively, are defined using the local propagation velocity. The secondary source terms $\delta\vec{S}_j^+$ and $\delta\vec{S}_j^-$ contain the local scattering information and are defined as

$$\begin{aligned}\delta\vec{S}_j^-(z_n^-;z_0) =& \mathbf{R}^\cup(z_n^-;z_n^-)\vec{P}_j^+(z_n^-;z_0)\\ &+\delta\mathbf{T}^-(z_n^-;z_n^+)\vec{P}_j^-(z_n^+;z_0)\end{aligned} \tag{2.16}$$

and

$$\begin{aligned}\delta\vec{S}_j^+(z_n^+;z_0) =& \mathbf{R}^\cap(z_n^+;z_n^+)\vec{P}_j^-(z_n^+;z_0)\\ &+\delta\mathbf{T}^+(z_n^+;z_n^-)\vec{P}_j^+(z_n^-;z_0),\end{aligned} \tag{2.17}$$

where $\mathbf{R}^\cap$ and $\mathbf{R}^\cup$ are the up-down and down-up reflection coefficients, respectively, and $\delta\mathbf{T}^\pm$ are the down-going and up-going transmission operators, respectively. Performing a round-trip by computing the downgoing wavefield at every depth until $m = M$ and then computing the upgoing wavefield from $m = M$ to $m = 0$ allows us to model synthetic data in the forward FWMod.

In FWMod, the source, propagation operators, and scattering operators are known and used to compute the synthetic seismic data. The reverse (FWMod^{-1}) can also be performed using the same reasoning, where the measurements, propagation, and scattering operators are known and the source properties need to be retrieved. FWMod^{-1} can be expressed using the following upgoing and downgoing wavefield equations :

$$\begin{aligned}\vec{P}_j^-(z_m^-;z_0) =& \mathbf{F}^+(z_m^+,z_M)\vec{P}_j^+\\ &(z_M;z_0)+\sum_{n=1}^{m}\mathbf{F}^-(z_m^+,z_n^-)\delta\vec{S}_j^-(z_n^-;z_0),\end{aligned} \tag{2.18}$$

moving down, and

$$\begin{aligned}\vec{P}_j^+(z_m^-; z_0) =& \mathbf{F}^+(z_m^-, z_0)\vec{S}_j^+(z_0) + \\ & \sum_{n=m}^{M-1} \mathbf{F}^-(z_m^-, z_n^+)\delta\vec{S}_j^+(z_n^+; z_0),\end{aligned} \tag{2.19}$$

moving up, where $\mathbf{F}^{\pm}$ are the reverse propagation operators. In FWMod and FWMod^{-1}, the scattering operators address the amplitude information of the seismic data, and the propagation operators address the phase information of the data.

As described by [20] and [21], FWM is built using both FWMod and FWMod^{-1} engines. FWM utilises seismic measurements, approximate source vectors, and the propagation operators to recover the scattering operator that corresponds to the reflectivity image. Here, the propagation operators are derived from a user-provided propagation velocity model and assumed to be correct. This is achieved by applying FWMod and FWMod^{-1} as a dual round-trip and comparing at every gridpoint the up- and downgoing wavefields of each engine and using a normalized cross-correlation to derive the scattering, i.e., reflectivity, operators. The synthetic results are then compared to the recorded data using a least-squares criterion, and the difference between the datasets is minimised, after which the next dual round-trip starts. The least-squares misfit function is given by

$$\begin{aligned}J(\mathbf{R}^{\cup}, \mathbf{R}^{\cap}) =& \sum_j \sum_{\omega} ||\vec{P}^-_{\mathrm{obs},j}(z_0; z_0) - \\ & \sum_{n=1}^{M} \mathbf{W}^-(z_0, z_n)\delta\vec{S}_j^-(z_n; z_0)||_2^2,\end{aligned} \tag{2.20}$$

where $\vec{P}^-_{\mathrm{obs},j}(z_0; z_0)$ is the measured data at the surface and $\delta\vec{S}_j^-$ represents the physical reflections. The reflectivity image is improved with each round trip and, by recursively applying the FWM engine, an increasing number of multiples are included in the modelled data.

A major holdback of migration technology is the assumption that the propagation velocities provided by the user are correct. Joint Migration Inversion (JMI) resolves this drawback by adding a velocity inversion element and performing seismic migration simultaneously as described by [10], [11]. The least-squares objective function that aims to minimise the reflectivity and propagation velocity at each gridpoint, using a gradient-descent scheme is given by

$$
\begin{aligned}
J(\mathbf{R}^{\cup},\mathbf{R}^{\cap},\delta\mathbf{W}^{+}\delta\mathbf{W}^{-}) = \sum_{j}\sum_{\omega} ||\vec{P}^{-}_{\text{obs},j}(z_0;z_0) - \\
\sum_{n=1}^{M} \mathbf{W}^{-}_{0}(z_0,z_n)[\delta\vec{S}^{-}_{j}(z_n;z_0) + \delta\vec{Q}^{-}_{j}(z_n;z_0)]||^{2}_{2},
\end{aligned}
\tag{2.21}
$$

where $\delta\mathbf{W}^{\pm}$ are the differential propagation operators and $\delta\vec{Q}^{-}_{j} = \delta\mathbf{W}^{-}(\vec{P}^{-}_{j} + \delta\vec{S}^{-})$ is the virtual scattering, which corrects the propagation error at each grid point. Finally, using current JMI technology, we assume that $\mathbf{R}$ and $\delta\mathbf{T}$ are angle- and frequency-independent, which, makes JMI insensitive to Amplitude versus Offset (AvO) effects and diving waves in the data as it struggles to handle far-offsets information [22].

2.4. Workflow

For these synthetic experiments, we propose the workflow shown in Figure 2.2 to improve the FWI results. Starting from the left, the synthetic data is modelled using FDM and is fed into the JMI engine as 'seismic data'. Iteratively, using a least-squares gradient-descent approach, JMI improves the propagation velocity estimate and reflectivity image migration. The reflectivity image is also used to constrain the velocity update at each iteration to reduce the smoothness of the final velocity estimate. Once the error function is minimised, the final inverted velocity estimate is used as the starting model for FWI. Again, using a least-squares gradient-descent approach, the error function is iteratively reduced. The final output is the high-resolution P-wave velocity estimate from FWI. Finally, the resultant velocity estimate is used once again to perform FWM to recover the reflectivity image of the subsurface. The velocity and reflectivity estimates are combined to produce a comprehensive image of the subsurface velocities and reflectors.

Table 2.1 compares the JMI and FWI features relevant to near-surface imaging. The goal of the proposed workflow is to derive a sharper FWI velocity estimate while approaching the global minimum in the solution space by using the JMI engine, which has a reduced dependency on the presence of low frequencies and the starting model. JMI should also help to explain some of the multiples in the data and include them in the starting model for FWI.

JMI	FWI
Reflection-based forward engine (FWMod)	Refraction-based forward engine (FDM)
Influence of reflectivity information on velocity inversion	Velocity inversion using primarily refracted and diving waves
Inherently handles multiples	Struggles with multiples
Smooth velocity estimate, sharp impedance imaging	Sharper “high-resolution” velocity estimate, no imaging component
Reduced dependency on low frequencies and starting models	Dependent on the presence of low frequencies in the data and a reliable starting model
AVO effects not included (angle-dependent reflectivity)	Improved performance when far-offsets are provided
Computationally less expensive due to coarser grid sampling	Finer sampling makes it computationally expensive

TABLE 2.1. – *Comparison of JMI and FWI features relevant to near-surface seismic velocity inversion.*

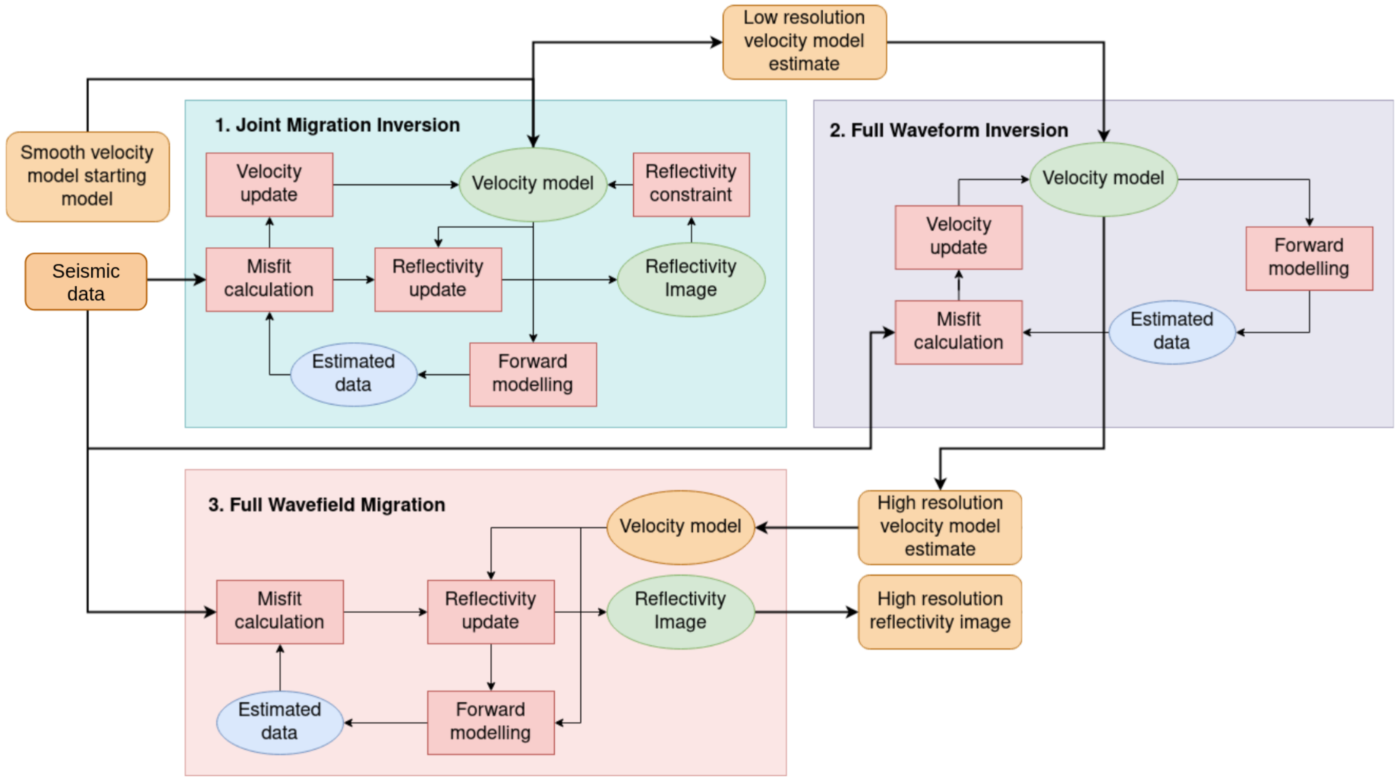

FIGURE 2.2. – *Combined inversion and migration workflow. The orange elements represent inputs and outputs; the red elements represent computational steps; the green elements represent models and images updated during the migration and inversion process, and the blue elements represent the estimated data.*

2.5. DATASETS

We generate synthetic seismic datasets based on marine near-surface models using acoustic FDM, avoiding so-called "inverse crime" for JMI. These models include features such as thin layers, velocity inversions, inclusions, and a shallow water layer, designed to replicate offshore near-surface conditions. The hydrophone array spans 300 metres, with receivers spaced at 2 m intervals and recording for 0.15 s. Shots are modelled every 2 metres, with a bandwidth limited to frequencies between 100 and 600 Hz. However, high frequencies result in spatial aliasing due to the receiver spacing, and this aliasing is not corrected in the data used for inversion, as shown in Figure 2.4.

Figure 2.3 shows an example of a ground-truth acoustic velocity, density and resulting reflectivity model used to create the synthetic data. Note that the reflectivity (R) is computed using the impedance (Z) between layer 1 and layer 2, such that

$$R = \frac{(Z_2 - Z_1)}{(Z_2 + Z_1)}, \tag{2.22}$$

where the impedance is the product of the acoustic velocity and density. The density model in Figure 2.3 was populated using realistic values from core sediment samples found in literature [23]. The models shown are scaled here to fit on the page, but the horizontal dimension is 300 m and the vertical dimension is 80 m. The intrusive feature in the high-velocity layer is, for example, only 2 m thick, approaching the limit of the propagation wavelength of 1.25 m in water for FDM using a 600 Hz frequency limit and exceeding the propagation wavelength of 2.3 m in the high-velocity layer. The seafloor is covered by a layer of mud-like sediments characterised by a small acoustic velocity contrast to the water column but a high density contrast, as seen in the reflectivity image. The subsurface layers are also characterised by velocity inversions and low impedance contrasts below the high-contrast top-layer. The starting velocity model for the JMI step and the FWI control step is a smooth version of the ground-truth velocities.

2.6. RESULTS

We apply the workflow shown in Figure 2.2 to three marine models, to validate the improvement in velocity estimates imaging. We compare the inversion and imaging results to the ground-truth models used to generate the FDM data, and compare the data residuals from the final imaging step.

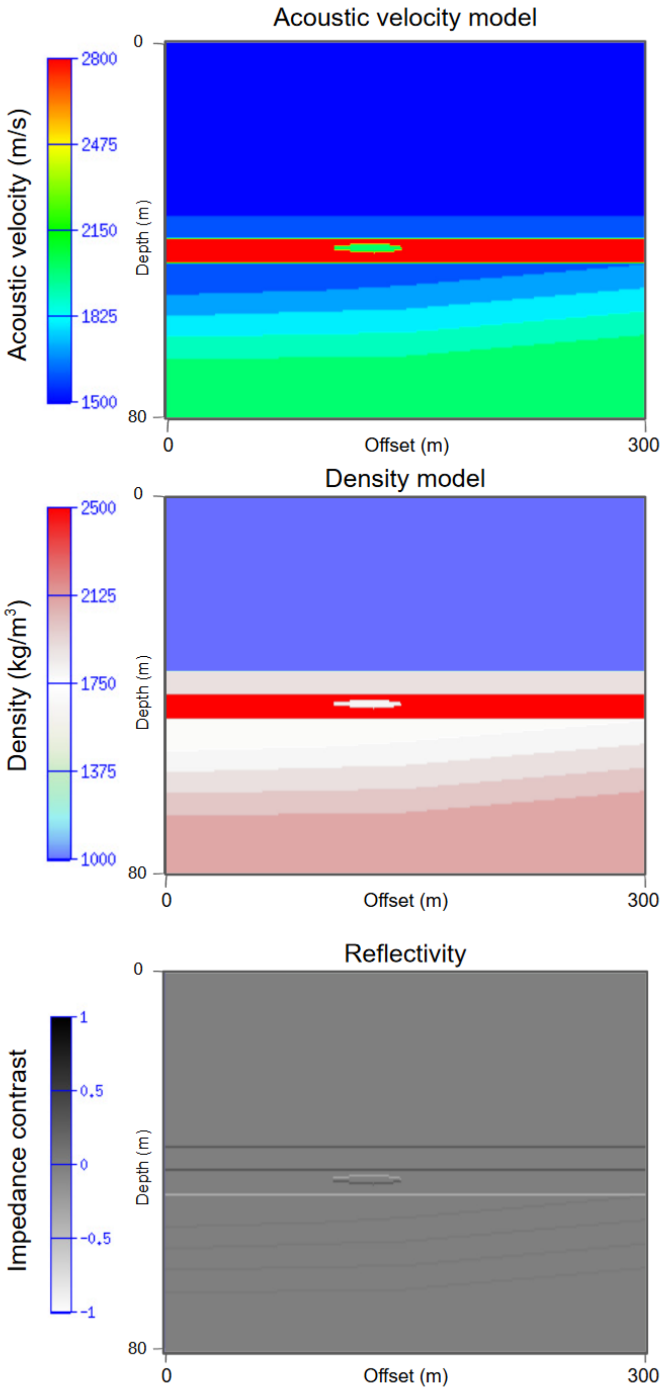

FIGURE 2.3. – *Example of a synthetic acoustic velocity and density models with associated reflectivity in terms of impedance contrast.*

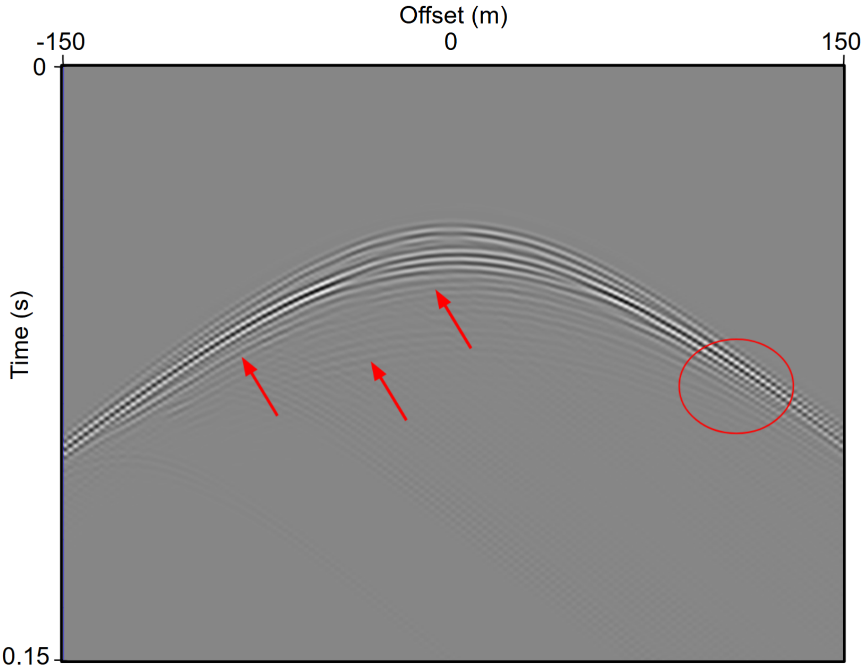

FIGURE 2.4. – *Example of FDM-generated shot record with internal multiples (red arrows) and aliasing (red circle).*

2.6.1. EXAMPLE 1 : CONFINED AQUIFER

The results of the JMI velocity estimation step are shown in Figure 2.5, and the resulting FWI velocities using the JMI model as a starting model are compared to the FWI control experiment. Masks can be used during the inversion in the data- or model-space to fix the velocities in the water-column or to constrain velocities from borehole measurements. This can be done by muting the data in the data-space or setting water velocities values after the update in the model-space, for example. In this chapter, no model masks are used in the examples presented for either inversion method. The JMI step successfully identifies the high-velocity layer and the aquifer branch, though the high velocities remain poorly constrained. Despite the relatively low resolution of the JMI update, the sediment layer is distinguishable, and some velocity contrast below 50 m is captured. These features appear in the velocity estimate due to the reflectivity constraint applied during the JMI process. The FWI step produces a sharper velocity estimate. In the control experiment without JMI, the velocities are poorly constrained, leading to vertical ringing above and below the high-velocity layer due to unexplained

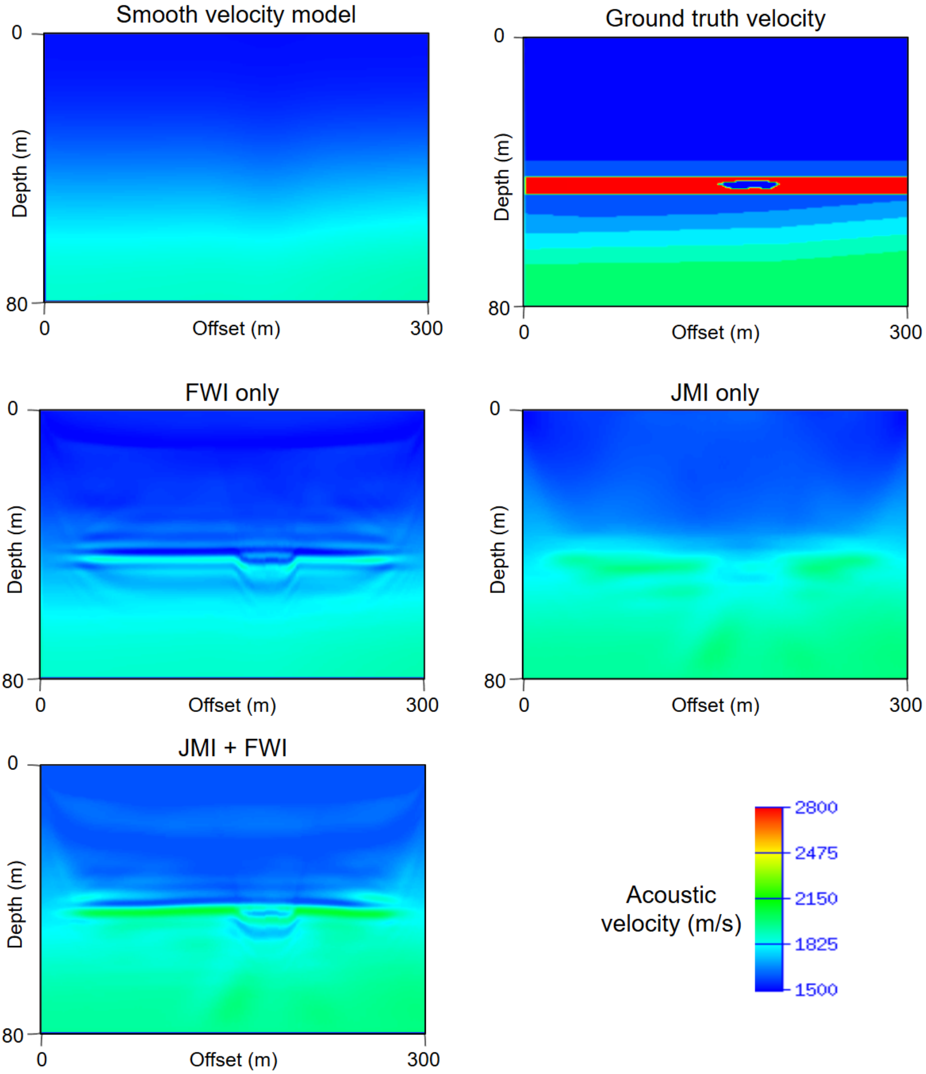

FIGURE 2.5. – *Inversion results of the FWI control experiment using the smooth starting model (FWI only) and the FWI experiment using a JMI-derived (JMI + FWI) starting model compared to the ground-truth velocity model and intermediate JMI velocity estimate (JMI only).*

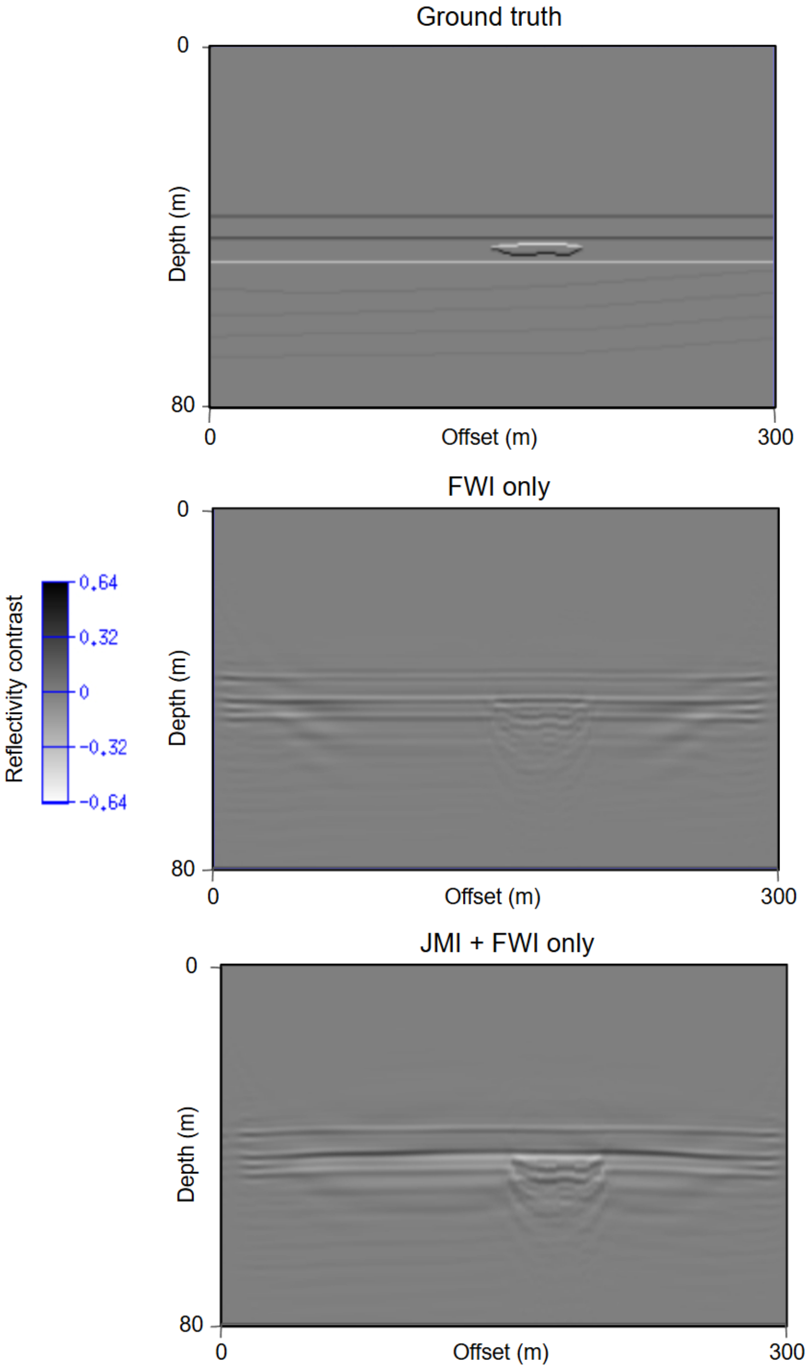

FIGURE 2.6. – *FWM imaging results using the control FWI experiment velocity estimate (left) and the FWI velocity estimate using the JMI-derived starting model experiment (right).*

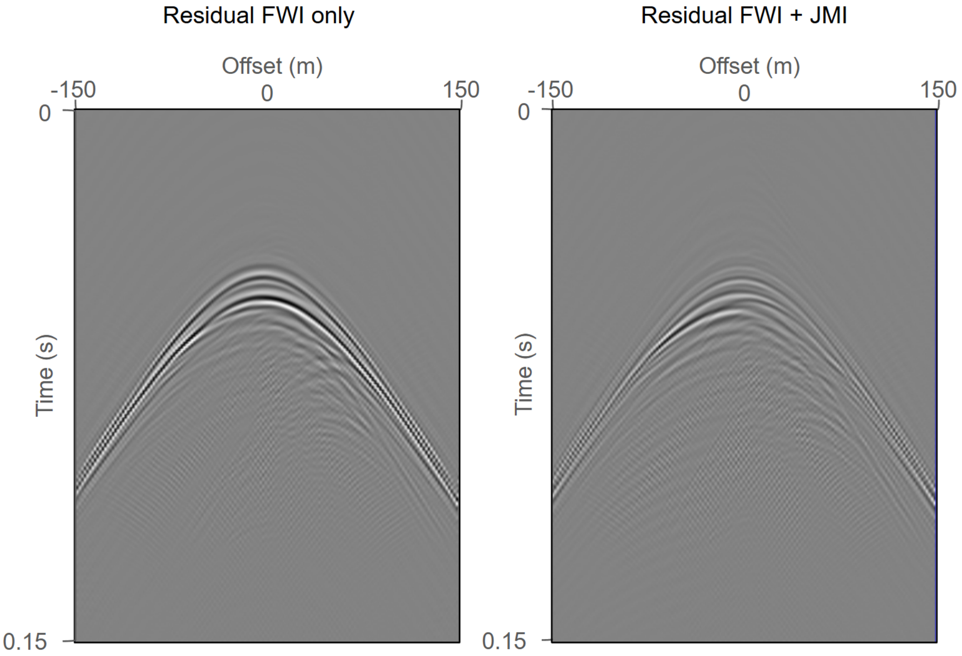

FIGURE 2.7. – *Residual of FWM for the control FWI experiment (left) and the FWI experiment using the JMI conditioning (right).*

data below the high-velocity layer, the model shows few updates. When JMI is used as the starting velocity model, the estimated velocities are closer to the ground-truth, though still underestimated. The depth of the high-velocity layer and the shape of the aquifer branch are also more accurately represented.

The imaging step using the derived velocities is shown in Figure 2.6, again, comparing the control FWI experiment to FWI using JMI as a model-conditioning step. As can be expected, the amplitudes of the reflectivity and depth location of the reflectors improve when the velocity model more closely resembles the ground-truth. However, the low estimation of velocities for the high-velocity layer fails to recreate the strong internal multiples in the aquifer branch layer, causing spurious artefacts below the aquifer branch. Nonetheless, the subsequent low-contrast layers are visible, whereas they are not in the control experiment. The residual between ground-truth and modelled data is shown in Figure 2.7, where the first arrivals are better explained by the velocities derived using the JMI-model conditioning. This is explained by the correct placement of the high-velocity layer and aquifer.

2.6.2. EXAMPLES 2 AND 3 : INCLUSIONS AND COMPLEX MODELS

The models for examples 2 and 3 are variations of the confined-aquifer model with example 3 being the most complex. Example 2 shows the effects of inclusions of various shapes and acoustic velocities, while example 3 includes successive velocity inversions, a graben structure represented by two slanted faults, and a diffractor in the sand layer. The inversion and imaging results for these examples are shown in Figures 2.8 and 2.9. As seen in example 1, using JMI to derive an acoustic starting model improves the final inversion and imaging results.

2.7. CONCLUSIONS

We demonstrated that JMI is an effective method for improving FWI velocity estimates in complex, high-frequency scenarios, even when no prior knowledge is available. By using JMI as a preprocessing step, FWI can achieve more accurate velocity reconstructions, making it a valuable approach for tackling challenging subsurface structures. One of the major challenges in FWI is its dependence on an accurate initial velocity model. Without a good starting model, FWI can easily become trapped in local minima, leading to erroneous velocity updates. JMI helps mitigate this issue by using reflectivity constraints to guide the velocity updates. This method ensures that velocity features related to reflections are better represented, allowing for a more reliable initial model for FWI. Additionally, because JMI is a migration-based method, it can exploit reflection data in ways that traditional FWI struggles with. The ability of JMI to extract meaningful velocity information from reflection data makes it a practical and computationally efficient alternative to traditional velocity model-building methods.

To further refine this method, future work should explore its application to shorter-offset and/or higher-frequency data. Additionally, a more integrated inversion scheme could be developed, where FWI is iteratively informed by JMI, incorporating reflectivity information throughout the process. This approach could help mitigate the risk of local minima and enhance the overall inversion stability. The relevance of integrating migration information becomes even greater when transitioning from acoustic to elastic models, as reflectivity inherently carries density information, making it crucial for subsurface characterization. Despite the promising results with synthetic experiments, several real-world challenges must be addressed before applying

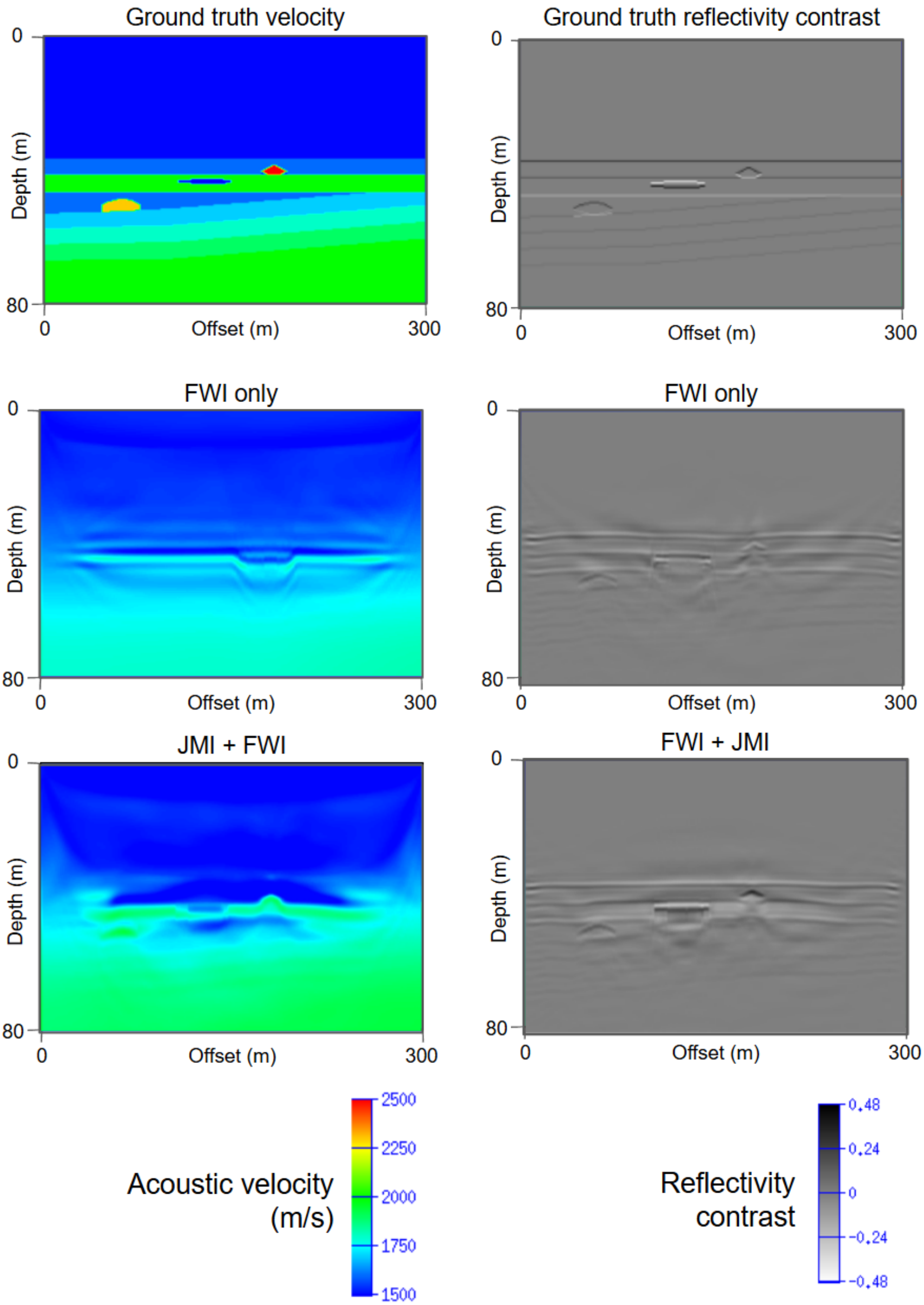

FIGURE 2.8. – *Inversion and imaging results for example 2.*

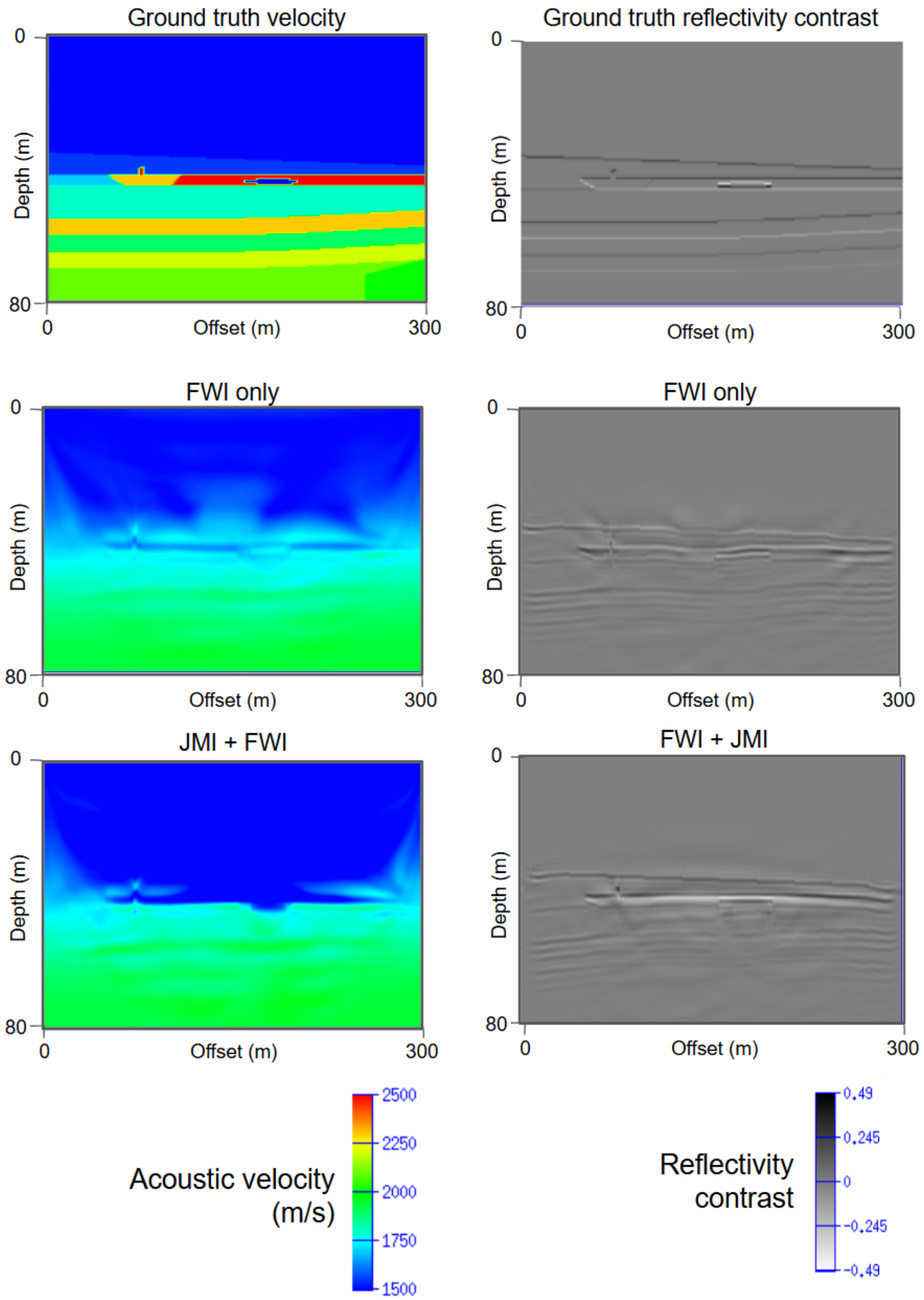

FIGURE 2.9. – *Inversion and imaging results for example 3.*

this method to field data. These synthetic tests were conducted under ideal conditions- with a generous acquisition footprint, no noise, and no positioning errors. In contrast, field data introduces significant complexities, such as acquisition imperfections, noise contamination, and the highly elastic nature of the near-subsurface, all of which can severely degrade FWI accuracy. Therefore, rigorous testing on field data is essential to assess the practical feasibility of this approach and to refine it for real-world applications.

RÉFÉRENCES

[1] J.-S. L'HEUREUX et M. LONG, « Relationship between Shear-Wave Velocity and Geotechnical Parameters for Norwegian Clays », *Journal of Geotechnical and Geoenvironmental Engineering*, t. 143, p. 04 017 013, fév. 2017. DOI : 10.1061/(ASCE)GT.1943-5606.0001645.

[2] K. SARKAR, V. VISHAL et T. N. SINGH, « An Empirical Correlation of Index Geomechanical Parameters with the Compressional Wave Velocity », *Geotechnical and Geological Engineering*, t. 30, p. 469-479, 2012. DOI : 10.1007/s10706-011-9481-2.

[3] G. PROVENZANO, M. VARDY et T. HENSTOCK, « Decimetric-resolution stochastic inversion of shallow marine seismic reflection data : dedicated strategy and application to a geohazard case study », *Geophysical Journal International*, t. 214, p. 1683-1700, juin 2018. DOI : 10.1093/gji/ggy221.

[4] J. VIRIEUX et S. OPERTO, « An overview of full-waveform inversion in exploration geophysics », *GEOPHYSICS*, t. 74, n° 6, WCC1-WCC26, 2009. DOI : 10.1190/1.3238367.

[5] W. MULDER et R.-E. PLESSIX, « Exploring some issues in acoustic full waveform inversion », *Geophysical Prospecting*, t. 56, n° 6, p. 827-841, 2008. DOI : https://doi.org/10.1111/j.1365-2478.2008.00708.x. eprint : https://onlinelibrary.wiley.com/doi/pdf/10.1111/j.1365-2478.2008.00708.x. adresse : https://onlinelibrary.wiley.com/doi/abs/10.1111/j.1365-2478.2008.00708.x.

[6] F. WANG et T. ALKHALIFAH, « Geological and Well Prior Assisted Full Waveform Inversion Using Conditional Diffusion Models », t. 2024, n° 1, p. 1-5, 2024, ISSN : 2214-4609. DOI : https://doi.org/10.3997/2214-4609.202410821. adresse : https://www.earthdoc.org/content/papers/10.3997/2214-4609.202410821.

[7] V. PRIEUX, G. LAMBARÉ, S. OPERTO et J. VIRIEUX, « Building starting models for full waveform inversion from wide-aperture data by stereotomography », *Geophysical Prospecting*, t. 61, p. 109-137, juin 2013. DOI : 10.1111/j.1365-2478.2012.01099.x.

[8] G. WANG, S. WANG, S. YUAN et S. LIAN, « Building a good initial model for full-waveform inversion using frequency shift filter », *Journal of Applied Geophysics*, t. 152, p. 129-136, 2018, ISSN : 0926-9851. DOI : https://doi.org/10.1016/j.jappgeo.2018.03.021. adresse : https://www.sciencedirect.com/science/article/pii/S0926985117308765.

[9] M. ARAYA-POLO, S. FARRIS et M. FLOREZ, « Deep learning-driven velocity model building workflow », *The Leading Edge*, t. 38, n° 11, 872a1-872a9, 2019. DOI : 10.1190/tle38110872a1.1. eprint : https://doi.org/10.1190/tle38110872a1.1. adresse : https://doi.org/10.1190/tle38110872a1.1.

[10] A. BERKHOUT, « Review paper : An outlook on the future of seismic imaging, part III : Joint migration inversion. », *Geophysical Prospecting*, t. 62, n° 5, p. 950-971, 2014. DOI : 10.1111/1365-2478.12158.

[11] D. J. VERSCHUUR, X. R. STAAL et A. J. BERKHOUT, « Joint migration inversion : Simultaneous determination of velocity fields and depth images using all orders of scattering », *The Leading Edge*, t. 35, n° 12, p. 1037-1046, déc. 2016, ISSN : 1070-485X. DOI : 10.1190/tle35121037.1. eprint : https://pubs.geoscienceworld.org/seg/tle/article-pdf/35/12/1037/3067754/gsedge_35_12_1037.pdf. adresse : https://doi.org/10.1190/tle35121037.1.

[12] A. J. BERKHOUT, « Pushing the limits of seismic imaging, Part I : Prestack migration in terms of double dynamic focusing », *Geophysics*, t. 62, n° 3, p. 937-953, 1997.

[13] S. QU, E. VERSCHUUR et Y. CHEN, « Full-waveform inversion and joint migration inversion with an automatic directional total variation constraint », *GEOPHYSICS*, t. 84, n° 2, R175-R183, 2019. DOI : 10.1190/geo2018-0085.1. eprint : https://doi.org/10.1190/geo2018-0085.1. adresse : https://doi.org/10.1190/geo2018-0085.1.

[14] S. MASAYA et D. J. VERSCHUUR, « Iterative reflectivity-constrained velocity estimation for seismic imaging », *Geophysical Journal International*, t. 214, n° 1, p. 1-13, mars 2018, ISSN : 0956-540X. DOI : 10.1093/gji/ggy105. eprint : https://academic.oup.com/gji/article-pdf/214/1/1/27718536/ggy105.pdf. adresse : https://doi.org/10.1093/gji/ggy105.

[15] J. THORBECKE, *2D Finite-Difference Wavefield Modelling*, Accessed : 2025-03-19, 2023. adresse : https://janth.home.xs4all.nl/Software/fdelmodcManual.pdf.

[16] J. W. THORBECKE et D. DRAGANOV, « Finite-difference modeling experiments for seismic interferometry », *GEOPHYSICS*, t. 76, n° 6, H1-H18, 2011. DOI : 10.1190/geo2010-0039.1. eprint : https://doi.org/10.1190/geo2010-0039.1. adresse : https://doi.org/10.1190/geo2010-0039.1.

[17] M. LOUBOUTIN, M. LANGE, F. LUPORINI, N. KUKREJA, P. A. WITTE, F. J. HERRMANN, P. VELESKO et G. J. GORMAN, « Devito (v3.1.0) : an embedded domain-specific language for finite differences and geophysical exploration », *Geoscientific Model Development*, t. 12, n° 3, p. 1165-1187, 2019. DOI : 10.5194/gmd-12-1165-2019. adresse : https://www.geosci-model-dev.net/12/1165/2019/.

[18] F. LUPORINI, M. LANGE, M. LOUBOUTIN, N. KUKREJA, J. HÜCKELHEIM, C. YOUNT, P. WITTE, P. H. J. KELLY, F. J. HERRMANN et G. J. GORMAN, « Architecture and performance of Devito, a system for automated stencil computation », *CoRR*, t. abs/1807.03032, juill. 2018. arXiv : 1807.03032. adresse : http://arxiv.org/abs/1807.03032.

[19] M. LOUBOUTIN, P. WITTE, M. LANGE, N. KUKREJA, F. LUPORINI, G. GORMAN et F. J. HERRMANN, « Full-waveform inversion, Part 2 : Adjoint modeling », *The Leading Edge*, t. 37, n° 1, p. 69-72, jan. 2018, ISSN : 1070-485X. DOI : 10.1190/tle37010069.1. eprint : https://pubs.geoscienceworld.org/seg/tle/article-pdf/37/1/69/7433275/tle37010069.1.pdf. adresse : https://doi.org/10.1190/tle37010069.1.

[20] A. BERKHOUT, « Review Paper : An outlook on the future of seismic imaging, Part II : Full-Wavefield Migration », *Geophysical Prospecting*, t. 62, n° 5, p. 931-949, 2014. DOI : https://doi.org/10.1111/1365-2478.12154. eprint : https://onlinelibrary.wiley.com/doi/pdf/10.1111/1365-2478.12154. adresse : https://onlinelibrary.wiley.com/doi/abs/10.1111/1365-2478.12154.

[21] M. DAVYDENKO et D. VERSCHUUR, « Full-wavefield migration : using surface and internal multiples in imaging », *Geophysical Prospecting*, t. 65, n° 1, p. 7-21, 2017. DOI : https://doi.org/10.1111/1365-2478.12360. eprint : https://onlinelibrary.wiley.com/doi/pdf/10.1111/1365-2478.12360. adresse : https://onlinelibrary.wiley.com/doi/abs/10.1111/1365-2478.12360.

[22] Y. SUN, Y. S. KIM, S. QU et E. VERSCHUUR, « Joint migration inversion : features and challenges », *Journal of Geophysics and Engineering*, t. 17, n° 3, p. 525-538, mars 2020, ISSN : 1742-2132. DOI : 10.1093/jge/gxaa012. eprint : https://academic.oup.com/jge/article-pdf/17/3/525/33034983/gxaa012.pdf. adresse : https://doi.org/10.1093/jge/gxaa012.

[23] E. J. EIDEM et M. L. KOLSTRUP, « Correlations between sound speed and density in seabed sediment cores collected in Norwegian waters », *Proceedings of Meetings on Acoustics*, t. 47, n° 1, p. 070 004, août 2022, ISSN : 1939-800X. DOI : 10.1121/2.0001588. eprint : https://pubs.aip.org/asa/poma/article-pdf/doi/10.1121/2.0001588/18136931/pma.v47.i1.070004_1.online.pdf. adresse : https://doi.org/10.1121/2.0001588.

3

JMI AND FWI EXPERIENCE ON NORTH SEA WINDFARM DATA

With a quantitative improvement of the seismic image and inverted velocities using a JMI-FWI workflow, it is logical to proceed to apply this method to field data, a much more complex case.

This chapter highlights the limitations experienced when refracted waves are no longer present in the data due to short offsets. In this case, a method like JMI can be more effective than FWI.

3.1. INTRODUCTION

As the proposed JMI-FWI workflow was successfully applied to synthetic examples in Chapter 2, we apply the same velocity inversion methods to a field dataset for the characterization of a potential windfarm site. To summarize the logic proposed in the previous chapter on this topic, the refraction-based FWI is a data-driven method that takes advantage of the full wavefield; it generally produces estimates of the propagation velocity field with higher resolution than tomographic methods [1], [2]. However, the propensity of FWI to approach the true solution is limited by missing low frequencies in the data, using a starting model that is too far from the truth, and the relatively short offsets found in UHR seismic data. JMI is a data-driven reflection-based inversion technique that can retrieve propagation velocities

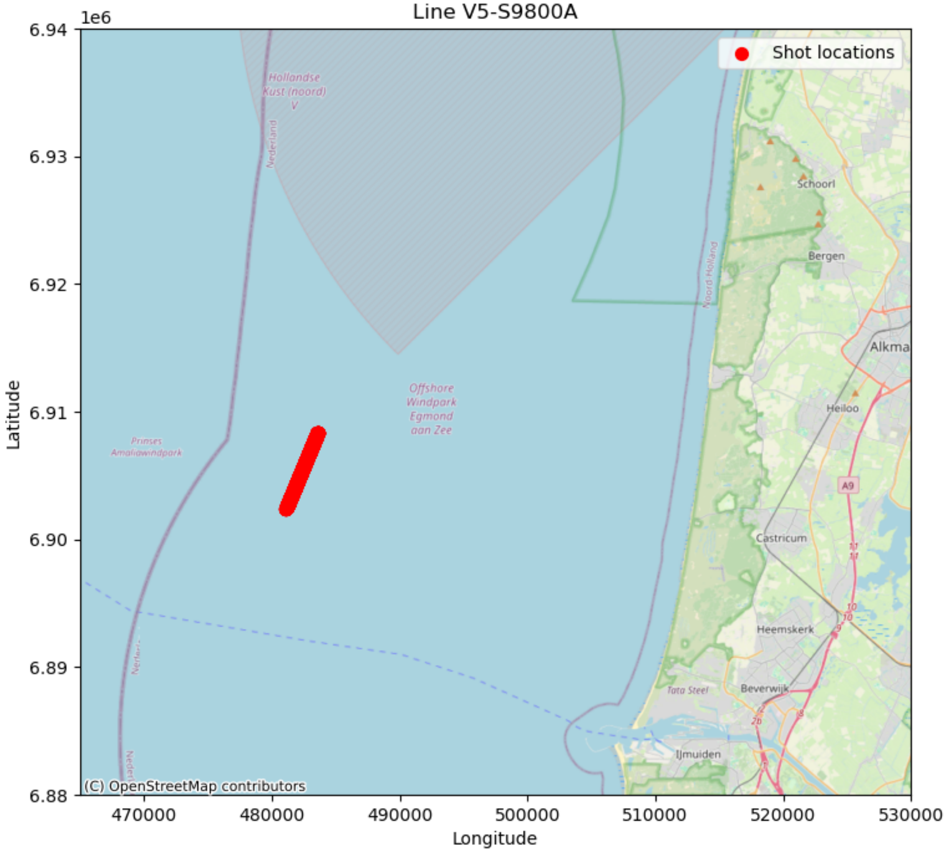

FIGURE 3.1. – *Location of the selected line shots in the Egmond aan Zee Offshore Windpark.*

and impedance images simultaneously where the impedance image can be used as a constraint on the inverted velocities [3], [4]. JMI is less dependent on a comprehensive starting model and the presence of low frequencies in the data, but it is sensitive to amplitude versus offset (AVO) effects and produces a lower-resolution velocity estimate. Although often not sufficient on its own, we have shown in Chapter 2 that it can be a powerful engine for building starting models for FWI, circumventing some of the limitations of FWI in a near-surface context. In this chapter, our goal is to demonstrate this inversion workflow using a field data example. In this case, we apply these methods to a 2DUHR survey from the Hollandse Kust Noord Windfarm Zone.

Survey date	29/09/17
Line number	V5-S9800A
Source bandwidth	150 - 1800 Hz
Time sampling	0.25 ms
Record time	0.2 s
Offset	12 - 120 m
Receiver spacing	1.5 m (12-48 m) 3 m (48-120 m)
Shot spacing	1.5 m
Towing depth limit	0.5 m ±0.1
Feathering angle	6^o
Average seafloor depth	18 m
Single source	yes
2D line	yes

TABLE 3.1. – *Survey parameters for 2D UHR data from the Hollandse Kust Noord windfarm zone.*

3.2. DATA PROCESSING

The raw data used in for the workflow is publicly archived [5] and no velocity-model estimate is included with the data. The acquisition parameters for the chosen line are summarized in Table 3.1. We select a line that shows multiple near-surface structures and look at a subset of 251 shots, shown geographically in Figure 3.1. The data processing is done using the following steps :

1. A bandpass filter between 150-1800Hz is applied to remove instrument response.
2. Analysis of the exact offset of each channel (8-channel segments glued together with variable spacing) using NMO velocity to obtain smooth lateral consistency of first primary.
3. Interpolation of missing near-offsets (0 - 12 m) using the Anti-Leakage Fourier Transform (ALFT) method on the approximate NMO corrected data [6].
4. Extrapolation to 241 channels with 120 m offset and even hydrophone spacing of 0.5 m.
5. FK-dip filtering to remove coherent noise before doing the inverse NMO.
6. Surface-Related Multiple Elimination (SRME), to predict and adaptively substract multiples generated by the free-surface without needing a

velocity model and with minimal preprocessing [7].

7. Laterally constrained predictive deconvolution with a single delay of 6ms over common offset sections, aiming to reduce reverberations in shallow layers and potential airgun bubbles.

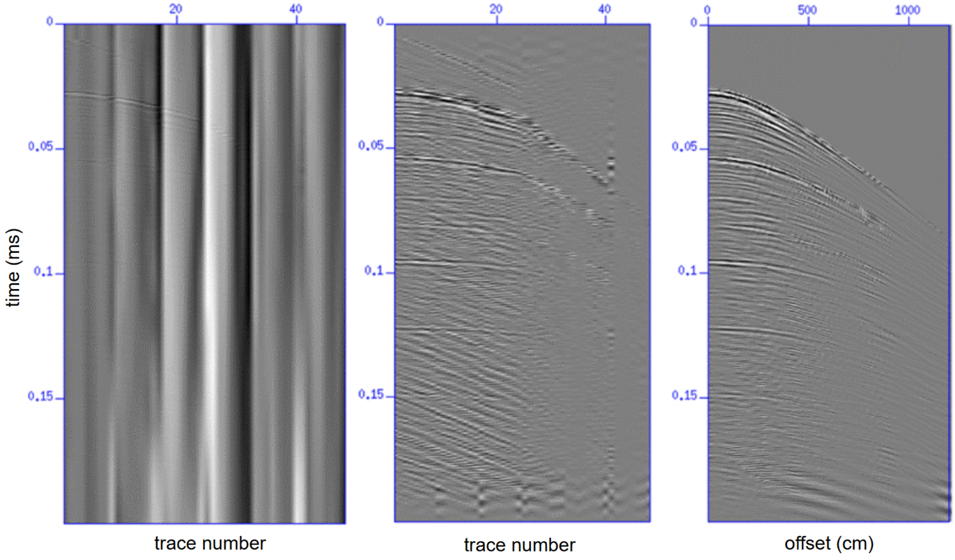

FIGURE 3.2. – *Example of a raw shot record (left), after bandpass filtering (middle) and after interpolation (right).*

Figure 3.2 shows the effects of the bandpass filtering and interpolation on the raw data. The results of the predictive deconvolution are shown on a shot record (index 150) in Figure 3.3. From the difference plot, we observe that some coherent periodic events are minimized which correspond to the linear noise from the acquisition ship. Some noise does remain in the data after the predictive deconvolution operation. The results of the SRME using L1 and L2 norms are shown in near-offsets in Figure 3.4. These show comparable results where the free-surface multiples appearing after 0.05 s are not fully removed with either solutions. For the processing and imaging, the L2-norm SRME results were used.

The shots from the final preprocessed dataset are shown in Figures 3.5 and 3.4, where we can observe several characteristic features of high-frequency offshore seismic data. Firstly, the streamer is towed at a shallow depth of approximately 0.5 m. Given the recorded frequency range of 150-1800 Hz, the

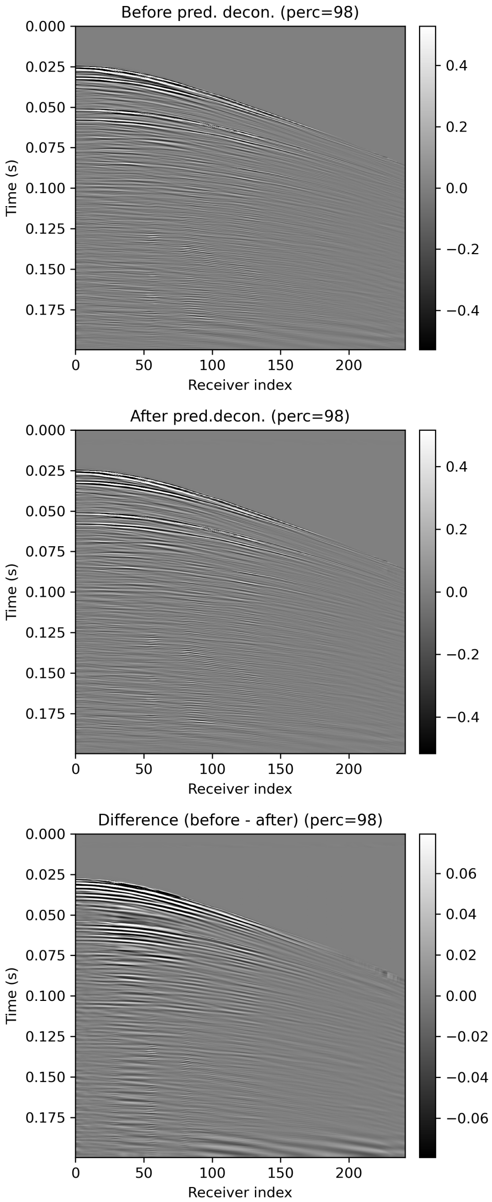

FIGURE 3.3. – *Comparison of shot record before and after predictive deconvolution for shot index 150 with the data after the short-offset interpolation (top), data after predictive deconvolution (middle) and the difference (bottom).*

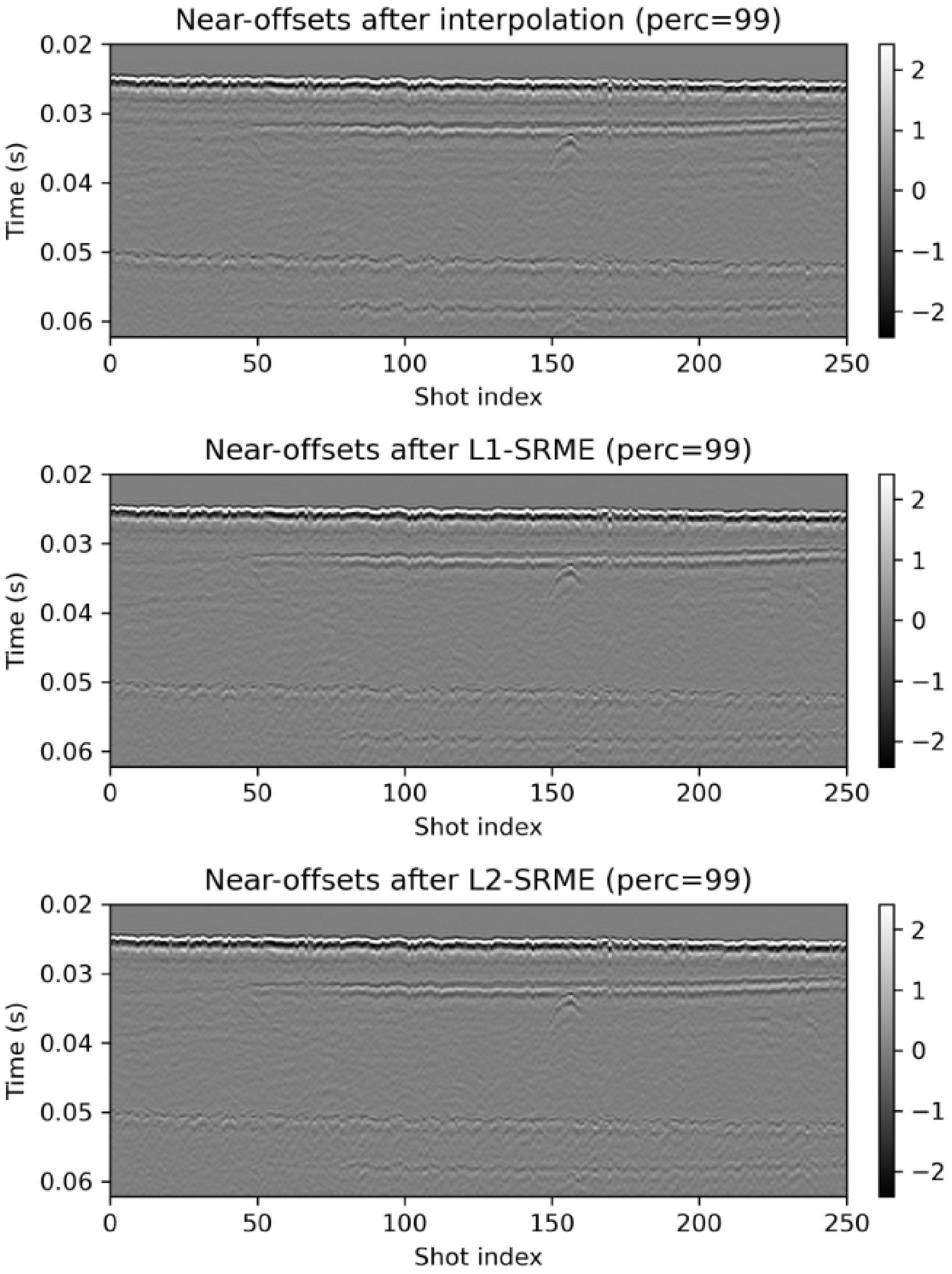

FIGURE 3.4. – *Near-offsets of the data after short-offsets (0-12 m) interpolation (top), after SRME using L1-norm (middle) and after SRME using L2-norm (bottom). The zoom on the time axis shows typical free-surface multiples starting at 0.05 s.*

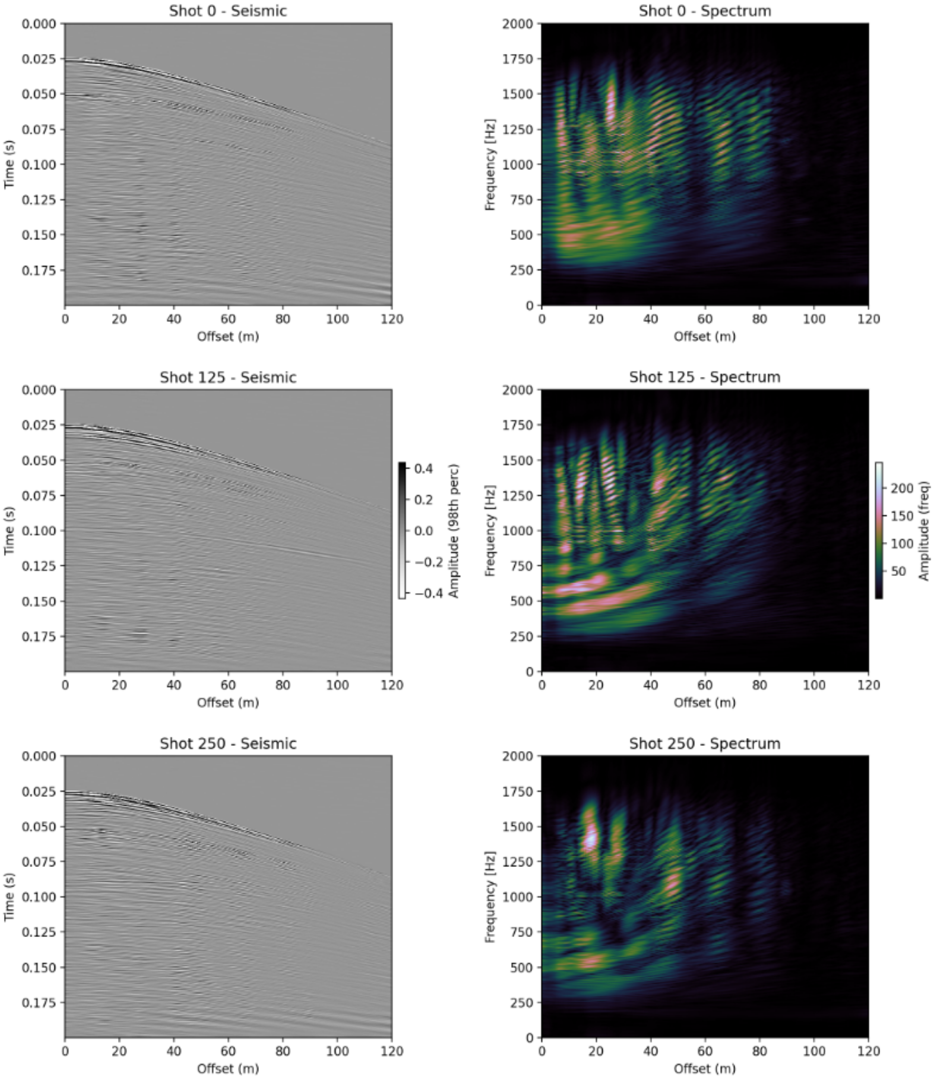

FIGURE 3.5. – *Example of processed shot records (left) and their corresponding frequency spectrum (right).*

towing depth is capable of generating receiver-side ghost notches in the frequency spectrum. These notches arise from destructive interference between the upgoing primary wavefield and its downward-reflected ghost wavefield from the sea surface (more information of ghost notches can be found in Chapter 4). For the towing depth of 0.5 m ±0.1 m, the first receiver-side ghost notch could appear from 1250 Hz to 1800 Hz, corresponding to a half-wavelength equal to twice the streamer depth. In this case, the ghost notch would therefore only appear at the end of the spectrum. Therefore, for the velocity inversion and imaging in this chapter, no further deghosting step is applied. Looking at Figure 3.5, we see that the frequency spectrum shows no notches, or ringing, for shot 0; however, notches are visible in shot 125 and shot 250. These are not caused by ghosts but rather by the interference between the primaries originating from the top and the bottom of a strong, shallow reflector that is also represented in the time-domain data. This reflector is visible in the near-offset section shown in Figure 3.4 to start around shot index 60.

The shallow towing depth of the streamer also increases the influence of surface-related noise, such as cable strumming and wave-induced pressure variation. As discussed above, despite applying predictive deconvolution and SRME, remnant free-surface multiples remain visible in the near-offset section. The persistence of free-surface multiples is likely exacerbated by wave-height variations causing inconsistent surface reflection angle and coefficient [8]. Additionally, 3D geometry effects and limited accuracy of the missing near-offset interpolation also contribute to the reduced effectiveness of SRME and predictive deconvolution [7], [9]. In the end, the uncorrected surface multiples and noise in the data complicate subsequent imaging and inversion steps.

3.3. METHODS

We create a starting velocity model featuring an 18 m water column, as reported in the survey data, and smoothly increasing seismic velocities down to 100 m. We use this starting velocity model for the JMI step and for the control FWI experiment. The source wavelet is designed using the frequency range provided by the survey metadata, and the amplitudes are adjusted based on the amplitudes in the field dataset.

We apply JMI with a reflectivity weight constant of 0.8 on the velocity update, as described by [10]. This means that reflectivities are used to steer velocity updates by making them more blocky. We apply a mask to the water layer for both the reflectivity and velocity updates and use a multiscale frequency scheme to execute 50 iterations with 5 iterations at full bandwidth.

We then apply FWI for 50 iterations at full bandwidth. Looking at the modelled wavefield, we include an equalisation step in the frequency-wavenumber domain to the FDM data in the FWI modelling stage to balance the amplitudes at offset.

To improve the convergence of the FWI process, the optimisation step is upgraded from a steepest-descent scheme to a Gauss–Newton scheme [11]. As described in Chapter 2, the steepest-descent method computes the gradient of the objective function using the data residual and the adjoint operator; this gradient is then scaled and applied to the velocity model as an update. Considering the least-squares objective function

$$f(m) = \frac{1}{2}||d - p(m)||^2, \tag{3.1}$$

where d is the field data and $p(m)$ the synthetic data produced by the forward modelling operator given model parameters m. The data residual is $r(m) = d - p(m)$ and the Jacobian (sensitivity kernel) is denoted by

$$\mathscr{J} = \frac{\partial p(m)}{\partial m}. \tag{3.2}$$

The gradient of the objective function with respect to the model is therefore

$$\nabla f(m) = \phi(m) = -\mathscr{J}^T r(m), \tag{3.3}$$

which is the quantity computed by the adjoint-state method in FWI. A full Newton update would require the exact Hessian $\nabla^2 f(m)$. For nonlinear least-squares problems, the Hessian can be approximated by the Gauss–Newton (GN) matrix,

$$H \approx \mathscr{J}^T \mathscr{J}. \tag{3.4}$$

Forming and inverting $\mathscr{J}^T \mathscr{J}$ is typically intractable in large-scale FWI; a practical compromise is to retain only its diagonal, yielding the diagonal approximation

$$H_{\text{approx}} = \text{diag}(\mathscr{J}^T \mathscr{J}), \tag{3.5}$$

which is cheaper to store and invert. The GN–type model update then applies the inverse diagonal scaling to the gradient :

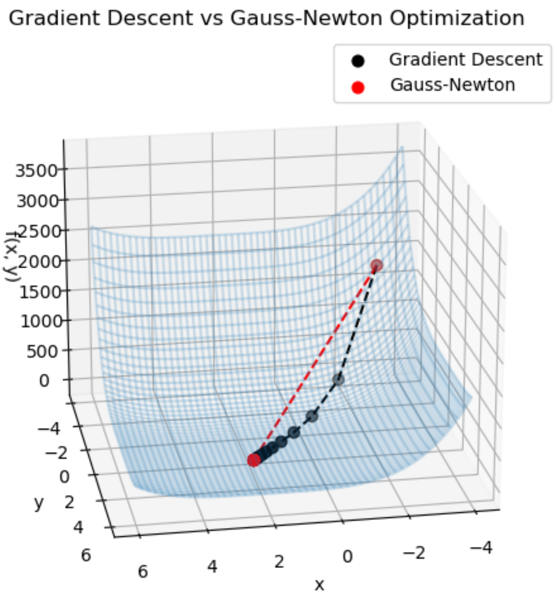

FIGURE 3.6. – *Comparison of the analytical convergence of gradient descent and Gauss-Newton optimisation for* $f(x) = (x+2)^4 + (y-3)^4 + 1$.

$$\delta m = -H_{\text{approx}}^{-1} \phi(m). \tag{3.6}$$

This diagonal GN preconditioner retains essential curvature information-reducing sensitivity to parameter scaling and improving step lengths -while avoiding the cost of assembling or inverting the full GN matrix. A comparison of the convergence of the GN optimisation compared to gradient descent is shown in Figure 3.6.

3.4. RESULTS

3.4.1. JMI

Figure 3.7 shows the results from the JMI inversion engine including the velocity estimate, objective function behaviour and residuals obtained from the JMI process. The objective function increases every 5 iterations due to the multi-banding strategy that sequentially introduces wider band of frequency and thereby increasing the misfit. The misfit at iteration 50 is therefore the minimum value for the full frequency spectrum. The inversion results confirms the presence of a high-velocity layer in the shallow section that was visible as a strong reflector in the near-offset plot (Figure 3.4). The model is better

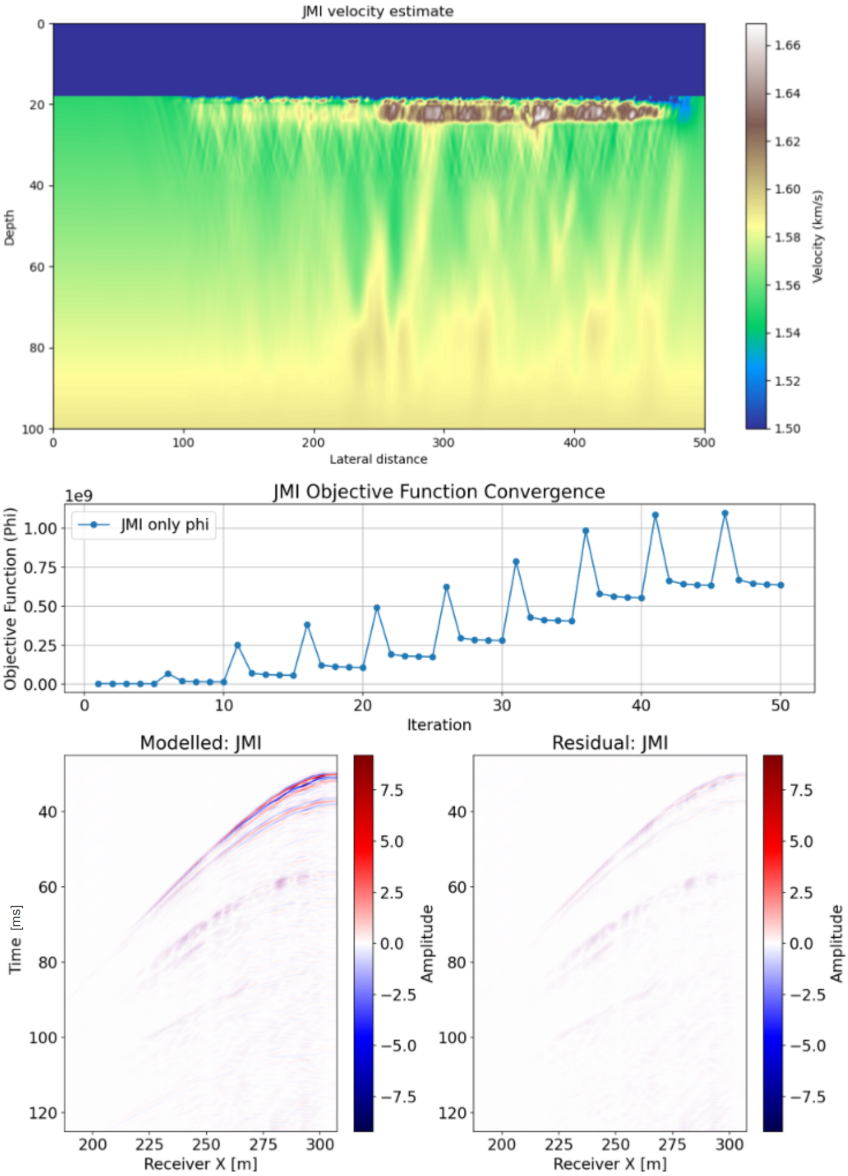

FIGURE 3.7. – *Results from the JMI procedure showing the estimated velocity model (top), the misfit value $\phi(m)$ (middle), the modelled data using FWMod and the JMI-derived velocity model at source location $x = 307.5$ m (bottom left) and the residual between the modelled data and the field data (bottom right).*

resolved on the right-hand side due to the increased illumination coverage from the moving streamer. Below the high-velocity layer, the velocities are poorly resolved, likely due to the absence of strong reflectors at depth. In the velocity estimate, we can also see the effects of the irregular acquisition that is not accounted for in the modelling as a "cross-hatched" pattern, most visible around a 30 m depth. In the misfit plot, the convergence is stable and the "steps" in the misfit function are caused by the multiscale frequency scheme used. Looking at the residuals, the data is relatively well explained but the relative residual amplitudes could be improved.

3.4.2. FWI

Figure 3.8 shows the velocity models obtained from FWI. When initialized with a smooth starting model, the inversion produces only minimal true velocity updates (top panel). For example, it fails to recover the high-velocity layer observed in the true structure. This behaviour indicates that the data lacks sufficiently long offsets, and therefore refracted arrivals and diving waves, causing the inversion to operate effectively in a reflection-mode regime rather than true transmission FWI [12]. Even when the JMI-derived model is used as the starting point, the resulting velocity remains overly smooth, showing only modest improvement in resolution, (3.8 (middle panel). The inversion tends to converge toward a gradually increasing velocity with depth, deviating from the expected layered structure. Additionally, the residual surface multiples in the data can be seen in the FWI velocity updates. Looking at the velocity-difference amplitudes between the two runs confirms that little additional information is gained from using the JMI model compared to the smooth one. The absence of refracted energy ultimately prevents FWI from recovering accurate layer velocities. In Figure 3.9, we show that best models were selected as the iteration where the objective function was most minimised. Yet, the recorded data is still quite poorly explained by the FWI-derived models and the residuals are larger overall than the modelled data.

Looking at the vertical velocity profiles shown in Figure 3.10, we can see that the reflections found in the short offsets contribute to the reconstruction of fine-scale interfaces, seen as the high-resolution, somewhat jittery, structures that are absent from the JMI velocity estimate. However, these cannot be considered tomographic velocity updates as the background velocities remain largely constrained around the initial velocity gradient; they are introduced by FWI to explain the reflection events.

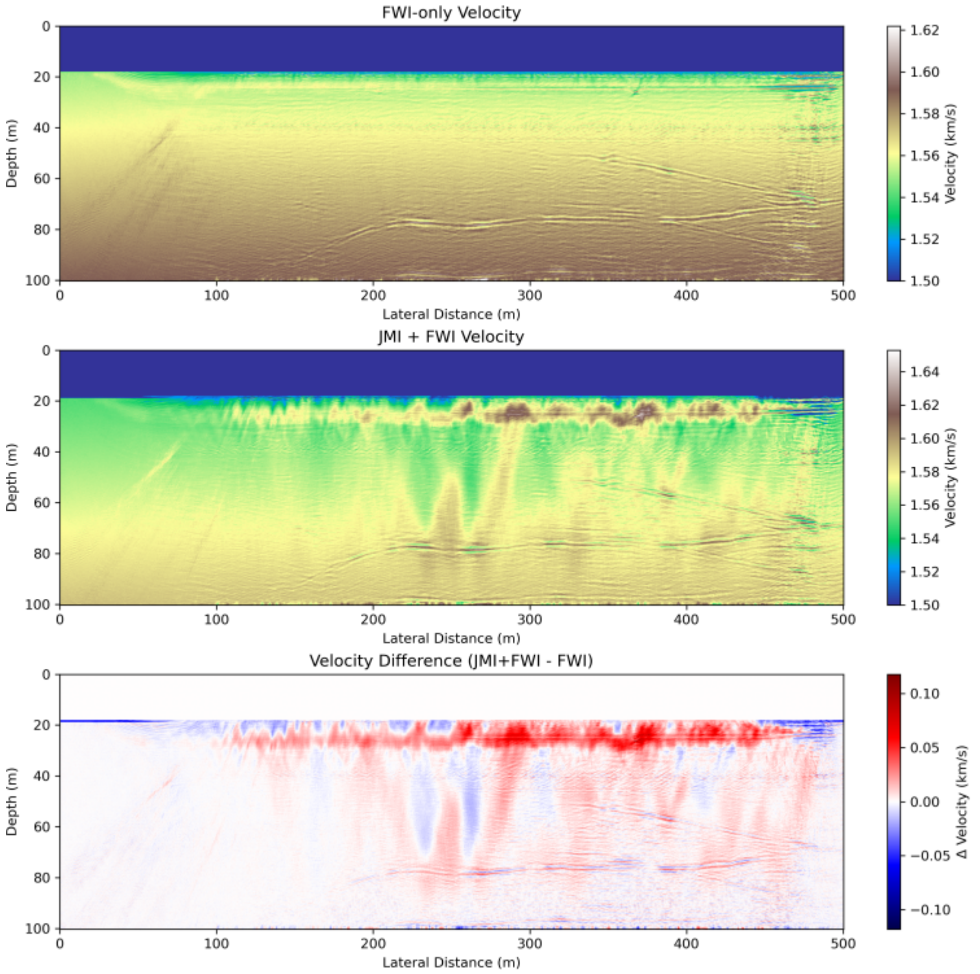

FIGURE 3.8. – *Velocity-inversion results from FWI using a smooth starting model (top); using a JMI-derived velocity model (middle) and the difference between the two panels (bottom).*

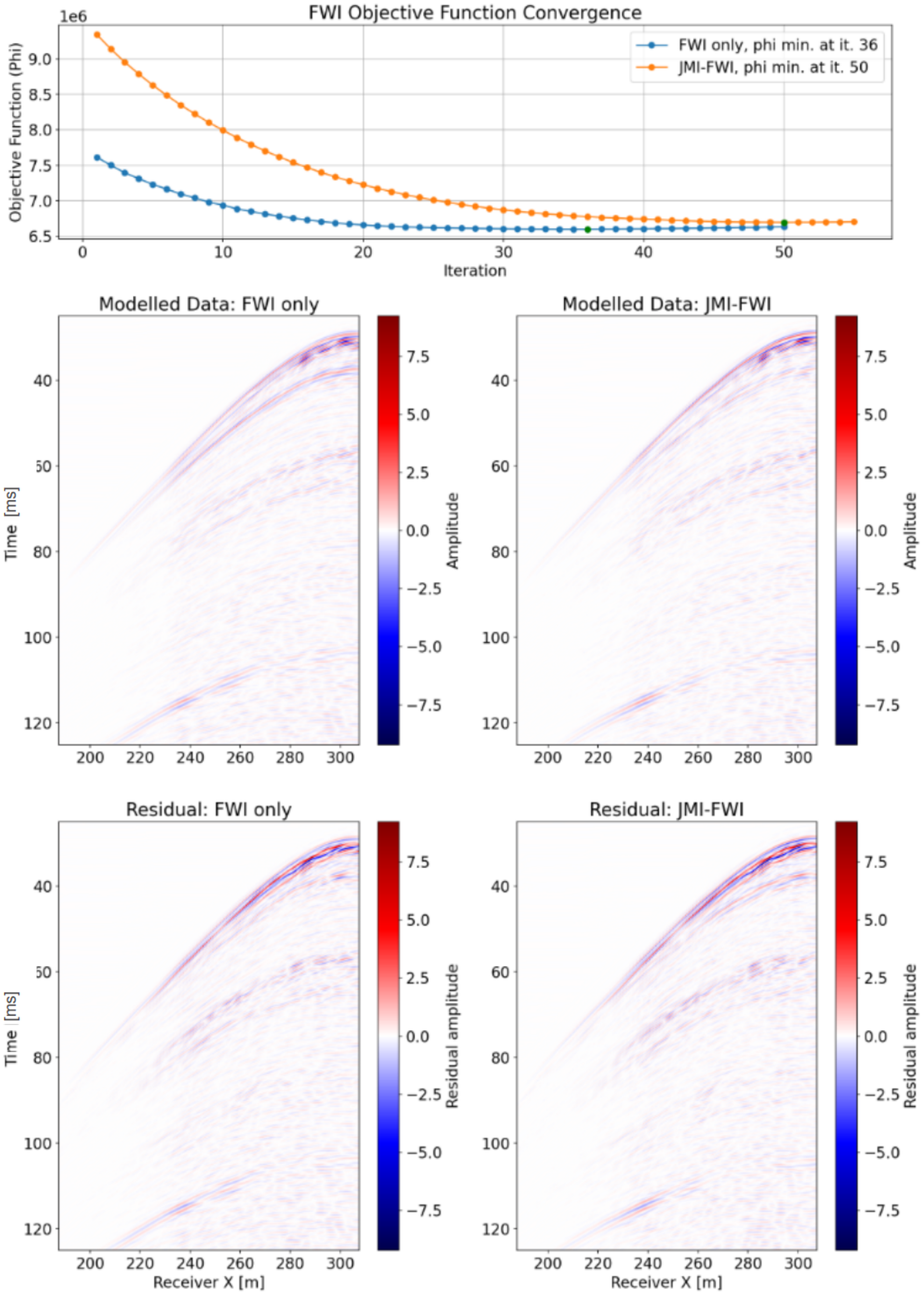

FIGURE 3.9. – *Results from the FWI procedure for the FWI with a smooth starting model (FWI-only) and with the JMI starting model (JMI-FWI), showing the misfit value $\phi(m)$ (top), the modelled data using FDM and the FWI-derived velocity model at source location x=307.5 (middle) and the residual between the modelled data and the field data (bottom), for each scenario.*

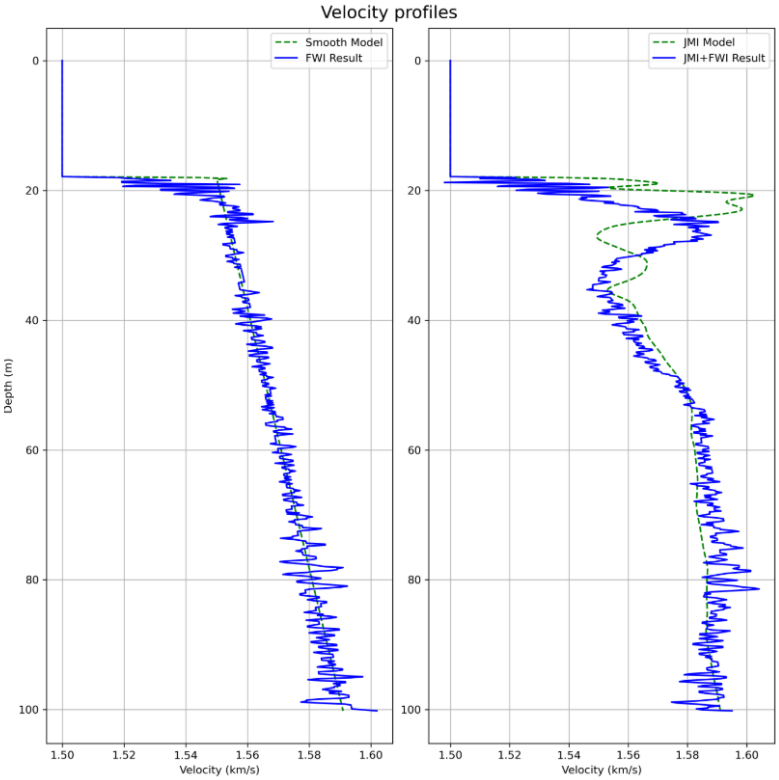

FIGURE 3.10. – *Vertical velocity profiles taken at* $x = 250$ *m comparing the FWI only estimated velocities with the smooth starting velocity model (left) and the JMI velocities compared the JMI+FWI velocities (right).*

3.4.3. REFLECTIVITY IMAGING (FWM)

Using the updated acoustic velocity models, we compare the impedance image obtained when using FWM with the JMI velocity model and when using FWM with the FWI acoustic velocity models. The results are shown in Figures 3.11. Firstly, all impedance images are very similar, showing surface multiples and a well-resolved high-velocity layer, though features below it are less clear. The high velocity from the JMI approach produces a slightly less flat bottom of the layer, which may better represent the diffracting boulder and the base of the high-velocity layer. In the zoomed view, shown in Figure 3.12, the acquisition footprint is visible above the seafloor, likely due to poorly constrained hydrophone locations (see Section 4) and imperfect near-offset interpolation. While clear faults are apparent in the shallow section below the high-velocity layer, most prominently after the FWI step. Ultimately, the

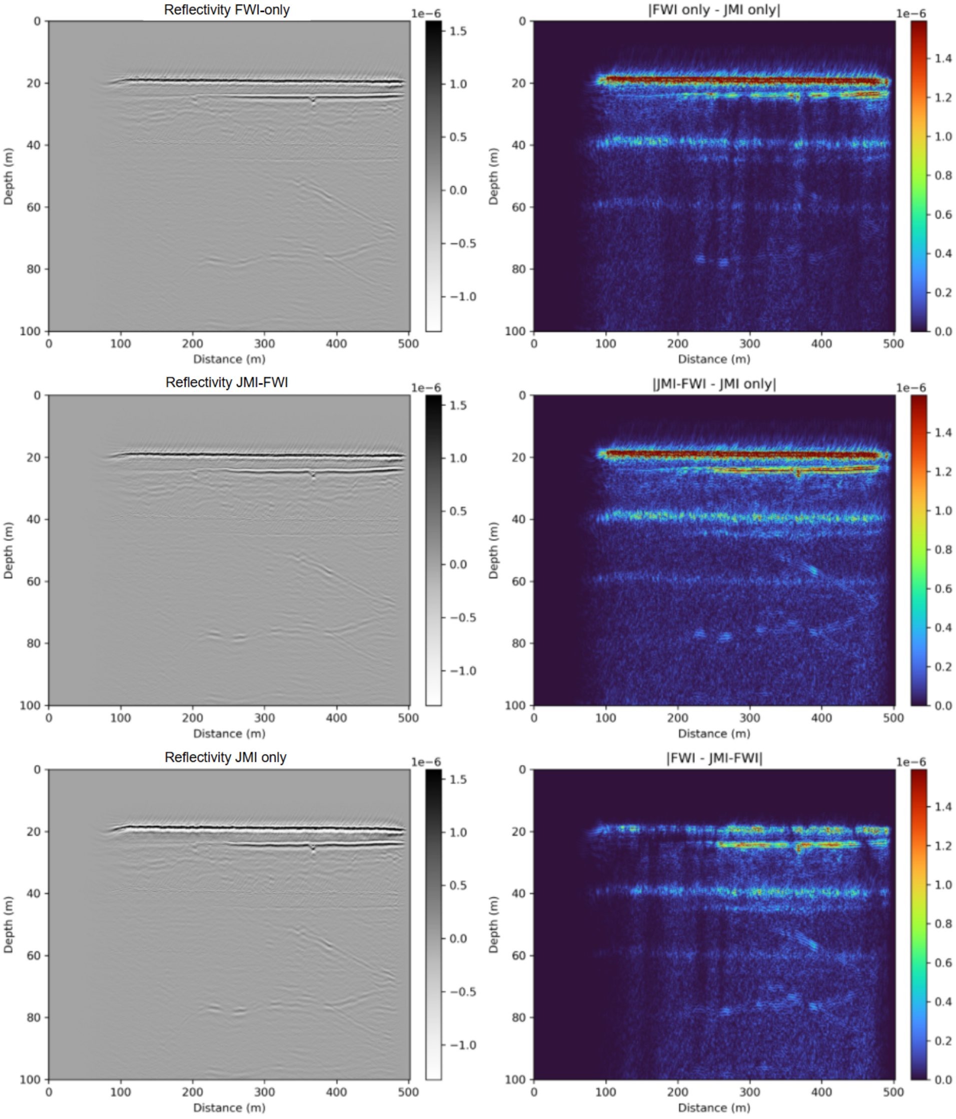

FIGURE 3.11. – *Comparison of migration results using FWM and different acoustic velocity models showing the reflectivity image from FWI only, JMI+FWI, and JMI only approaches (left column, top to bottom) and the absolute differences between the respective models (right column).*

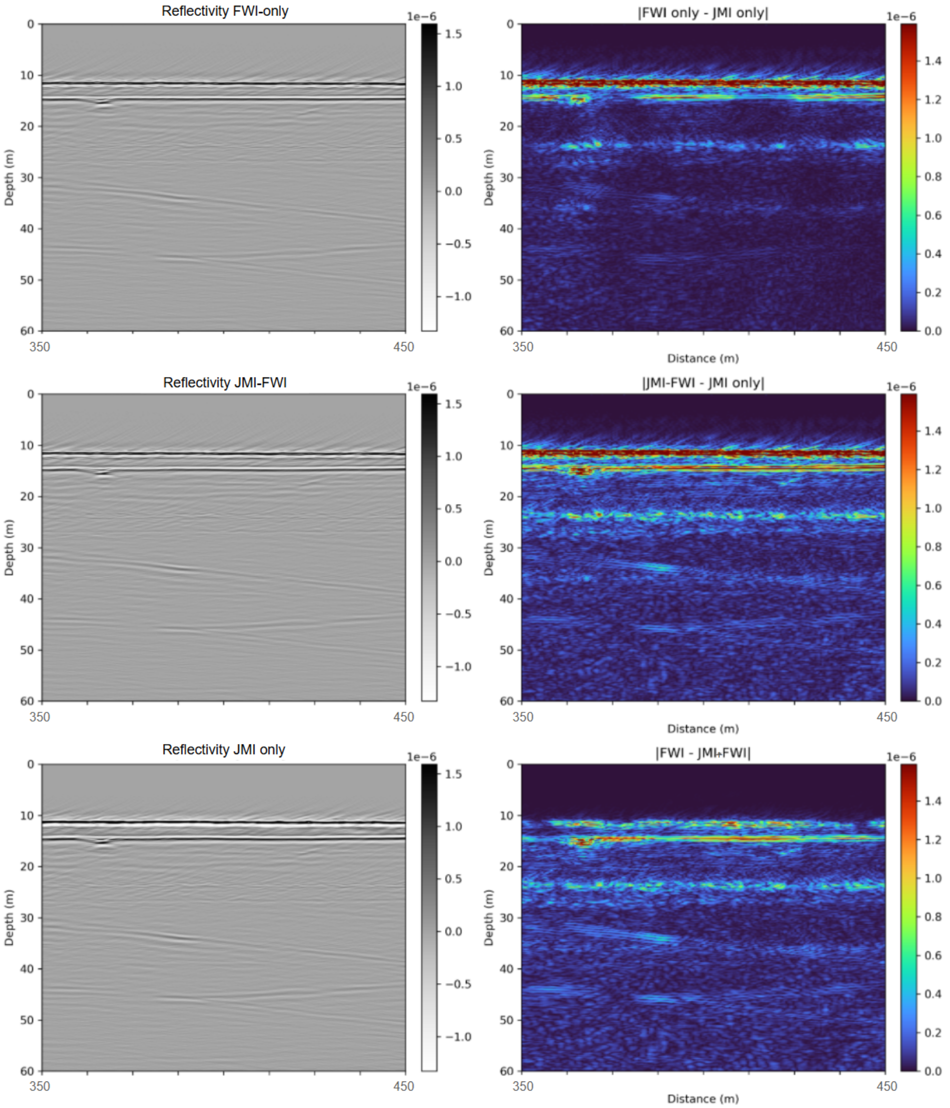

FIGURE 3.12. – *Same as Figure 3.11, zoomed in.*

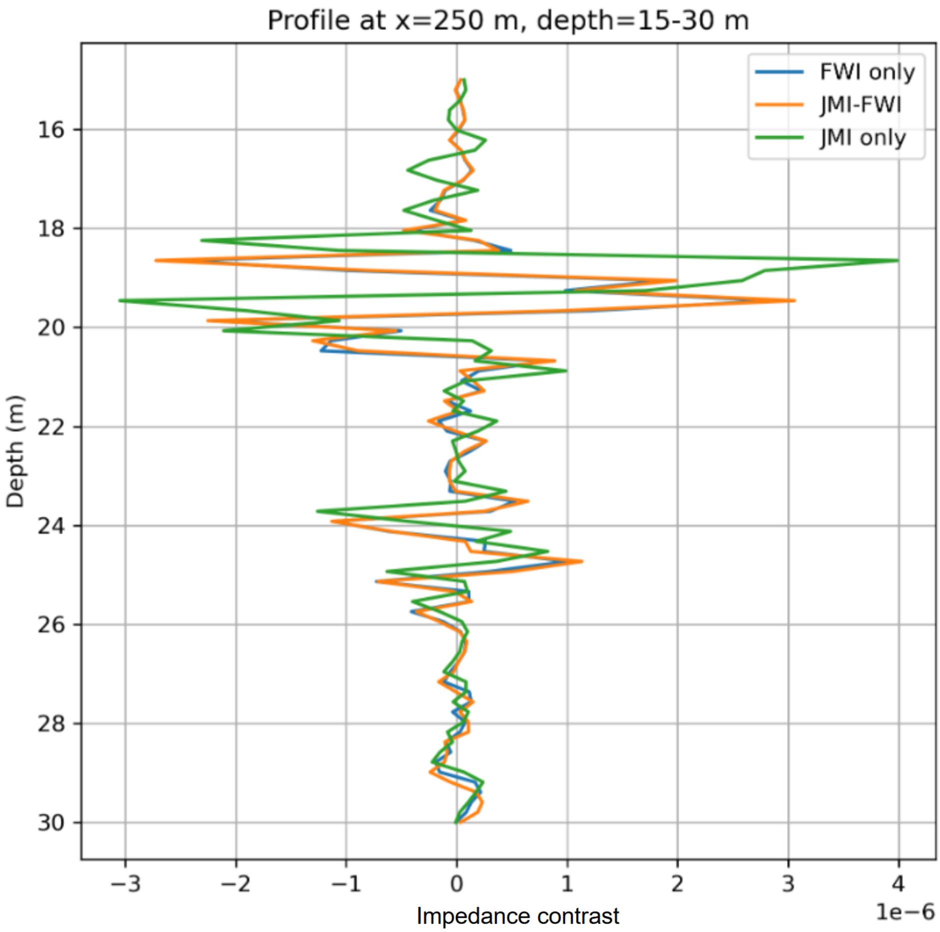

FIGURE 3.13. – *Profiles of the reflectivity at x=250m for depths 15-30 m. The blue profile for FWI only lays partially below the orange profile for JMI+FWI.*

difference between the velocity profiles affect the amplitudes of the impedance and the depths associated with the reflectors, as can be seen in the impedance profile in Figure 3.13. Additionally, the reflectivity derived for the FWI only and the FWI with JMI case are near-identical above 15 meters (bottom right plot of Figure 3.11 and 3.12) which explains why the profiles almost perfectly overlap in Figure 3.13. The impedence contrast is so similar in this shallow layer due to the mask constraint applied in the water layer that can be seen in Figure 3.8.

3.5. DISCUSSION

When refracted waves are missing from the data used in FWI, the inversion loses critical information about the low-wavenumber components of the velocity model. Refracted waves propagate along deeper paths and sample the long-wavelength structures of the subsurface, which are essential for accurately recovering the background velocity. Without them, the gradient of the FWI objective-function becomes dominated by high-wavenumber contributions from reflected waves. This leads to cycle-skipping issues : the misfit surface develops local minima that trap the inversion, preventing the reconstruction of the true low-wavenumber model. In practical terms, the inversion may converge to a model that fits the reflections but has incorrect overall velocities, which can severely affect subsequent imaging and interpretation, as we have seen in the results of this experiment.

This problem is visually represented by the so-called 'bunny-ears' artifact in FWI. When the objective function gradient is dominated by reflections, the energy in the gradient splits along the two edges of the reflection path, as shown in Figure 3.14. This occurs because reflections are sensitive mainly to contrasts rather than smooth background velocities, creating high-wavenumber updates on either side of the true interface. The bunny-ears pattern is a direct consequence of the derivative of the misfit function with respect to the model parameters : it reflects where the data residuals correlate with the wavefield, but lacks the directional information provided by refracted or diving waves. A method that can utilise this is Reflection Waveform Inversion (RWI), which separates the inversion into a background model update and a reflectivity update, allowing the inversion to partially recover low-wavenumber structures even when refracted waves are weak or missing [13]. Essentially, RWI employs the same logic as JMI, making the primary difference between the two the forward-modelling and migration engines (i.e., FDM vs FWMod and least-squares reverse time migration vs FWM).

3.6. CONCLUSIONS

Compared to our examples on synthetic data, the application of the JMI-FWI workflow failed with this specific North Sea windfarm dataset. Simply assessed, FWI cannot update velocities without the refracted and diving waves, which were not captured with the 120 m maximum acquisition offset (compared to 300 m in the synthetic examples). Diving waves that may have been presents for shallower depths (until 30m), may not have been accessible due to the data quality and could have been lost during the data processing, affecting the performance of FWI, even at shallower depths. Objectively looking at these results, we must conclude that the industry-standard FWI should not be the method of choice to retrieve velocity information in these kinds of UHR surveys. RWI may be able to exploit the reflected waves and improve the convergence; however, this is still dependent on the relative offset in the data and is a method that is even more expensive than FWI. In contrast, JMI did perform sufficiently well on its own. Specifically, information about the presence of a high-velocity layer at the depth seen in this dataset may be extremely relevant to geotechnical applications; for example, for the installation of windfarm monopiles that are driven up to 20 m below the seabed.

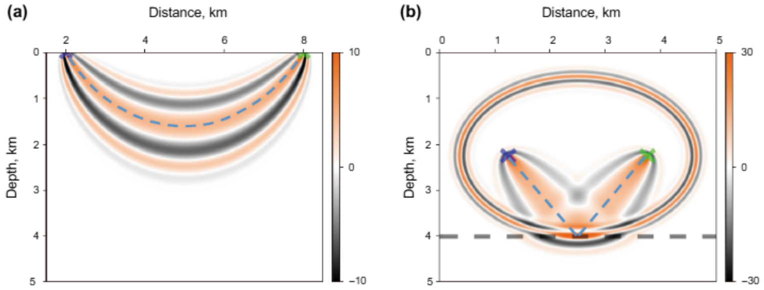

FIGURE 3.14. – *Figure from [13] showing the sensitivity kernels of transmitted waves (a) and reflected waves (b) in conventional FWI.*

It is undeniable that the JMI-derived velocity model is still overly smooth and poorly constrained at depth. It could certainly be further improved by improving the data processing, introducing gradient conditioning methods (see Chapter 7), using a more accurate starting velocity model and the presence of more and stronger deep reflectors. Improving the data processing may include : shot-by-shot effective wavelet estimation directly from the data and improved free-surface multiple and ship-related noise suppression. When it comes to the removal of free-surface multiples, SRME is a robust method that would have been sufficient in exploration acquisition set-ups; however, the performance here was unusually poor. We suspect that this is caused by the effects of wave height on the streamer, the relatively large missing near-offset gap, and the poor control over hydrophone position and depth during the survey. The latter is a topic that we will explore in more detail in the next chapter.

RÉFÉRENCES

[1] W. MULDER et R.-E. PLESSIX, « Exploring some issues in acoustic full waveform inversion », *Geophysical Prospecting*, t. 56, n° 6, p. 827-841, 2008. DOI : https://doi.org/10.1111/j.1365-2478.2008.00708.x. eprint : https://onlinelibrary.wiley.com/doi/pdf/10.1111/j.1365-2478.2008.00708.x. adresse : https://onlinelibrary.wiley.com/doi/abs/10.1111/j.1365-2478.2008.00708.x.

[2] D. TEODOR, C. COMINA, F. K. ANJOM, R. BROSSIER, L. V. SOCCO et J. VIRIEUX, « Challenges in shallow target reconstruction by 3D elastic full-waveform inversion — Which initial model? », *GEOPHYSICS*, t. 86, n° 4, R433-R446, 2021. DOI : 10.1190/geo2019-0523.1. eprint : https://doi.org/10.1190/geo2019-0523.1. adresse : https://doi.org/10.1190/geo2019-0523.1.

[3] Y. SUN, Y. S. KIM, S. QU et E. VERSCHUUR, « Joint migration inversion : features and challenges », *Journal of Geophysics and Engineering*, t. 17, n° 3, p. 525-538, mars 2020, ISSN : 1742-2132. DOI : 10.1093/jge/gxaa012. eprint : https://academic.oup.com/jge/article-pdf/17/3/525/33034983/gxaa012.pdf. adresse : https://doi.org/10.1093/jge/gxaa012.

[4] G. EISENBERG, E. SCHUENEMANN, G. GIERSE, E. VERSCHUUR et S. QU, « Robust velocity estimation via joint migration inversion and full waveform inversion », in *SEG Technical Program Expanded Abstracts 2019*. 2019, p. 1224-1228. DOI : 10.1190/segam2019-3216236.1. eprint : https://library.seg.org/doi/pdf/10.1190/segam2019-3216236.1. adresse : https://library.seg.org/doi/abs/10.1190/segam2019-3216236.1.

[5] RIJKSDIENST VOOR ONDERNEMEND NEDERLAND (RVO), *Offshore Wind Datahub*, Accessed : 2024-09, 2025. adresse : https://datahub.pleio.nl/.

[6] s. XU, Y. ZHANG, D. PHAM et G. LAMBARÉ, « Antileakage Fourier transform for seismic data regularization », *Geophysics*, t. 70, p. V87-V95, juill. 2005. DOI : 10.1190/1.1993713.

[7] D. VERSCHUUR et A. BERKHOUT, « Estimation of multiple scattering by iterative inversion, Part II : Practical aspects and exemples. », Undefined/Unknown, *Geophysics*, t. 62, n° 5, p. 1596-1611, 1997, ISSN : 0016-8033, ISSN : 0016-8033.

[8] G. BLACQUIÈRE et H. Ö. SERTLEK, « Modeling and assessing the effects of the sea surface, from being flat to being rough and dynamic », *GEOPHYSICS*, t. 84, n° 2, T13-T27, 2019. DOI : 10.1190/geo2018-0294.1. eprint : https://doi.org/10.1190/geo2018-0294.1. adresse : https://doi.org/10.1190/geo2018-0294.1.

[9] D. J. VERSCHUUR, A. J. BERKHOUT et C. P. A. WAPENAAR, « Adaptive surface-related multiple elimination », *Geophysics*, t. 57, n° 9, p. 1166-1177, 1992. DOI : 10.1190/1.1443330.

[10] S. MASAYA et D. J. VERSCHUUR, « Iterative reflectivity-constrained velocity estimation for seismic imaging », *Geophysical Journal International*, t. 214, n° 1, p. 1-13, mars 2018, ISSN : 0956-540X. DOI : 10.1093/gji/ggy105. eprint : https://academic.oup.com/gji/article-pdf/214/1/1/27718536/ggy105.pdf. adresse : https://doi.org/10.1093/gji/ggy105.

[11] D.-H. SHEEN, K. TUNCAY, C.-E. BAAG et P. J. ORTOLEVA, « Time domain Gauss—Newton seismic waveform inversion in elastic media », *Geophysical Journal International*, t. 167, n° 3, p. 1373-1384, déc. 2006, ISSN : 0956-540X. DOI : 10.1111/j.1365-246X.2006.03162.x. eprint : https://academic.oup.com/gji/article-pdf/167/3/1373/6003926/167-3-1373.pdf. adresse : https://doi.org/10.1111/j.1365-246X.2006.03162.x.

[12] G. YAO et D. WU, « Reflection full waveform inversion », *Science China Earth Sciences*, t. 60, p. 1-12, sept. 2017. DOI : 10.1007/s11430-016-9091-9.

[13] G. YAO, D. WU et S. X. WANG, « A review on reflection-waveform inversion », *Petroleum Science*, t. 17, p. 334-351, 2020. DOI : 10.1007/s12182-020-00431-3. adresse : https://doi.org/10.1007/s12182-020-00431-3.

4

STREAMER-POSITIONING PROBLEMS DURING FIELD UHR ACQUISITION

In UHR seismic acquisition, the inability to accurately track streamer depth and shape in real-time creates major ambiguities in hydrophone positioning.These errors degrade the quality of the data, hindering the results of processes that depend on relative source-receiver positions.

This chapter serves as an introduction and justification to the work presented in Chapters 5 and 6.

By attending conference sessions on the offshore near-surface, we were marked by some of the practical issues that separate the synthetic examples shown in Chapter 2 and the field data shown in Chapter 3. Firstly, several of the talks were given by industry participants rather than academic or institute researchers, which indicated a strong interest in near-surface offshore imaging and characterization for the energy and geotechnical industries. Secondly, several papers highlighted the specific schemes employed on near-surface field datasets to tackle their intricacies [1], [2]. While these observations validated the analysis underpinning the parametrization of the synthetic datasets and the rationale for a JMI-FWI workflow, there was one issue that we had not yet considered in this research. This problem was, in fact, the origin of severe damage and statics in the data. An emphasis on this issue is published in the conclusions of a paper by Henrique Duarte et al. on Advanced processing for UHR3D shallow marine seismic surveys[1] :

---

[1] Because this paper is available online behind a paywall, the untruncated quote from the conclusions of Duarte et al., 2017 [1] can be found after the bibliography of this chapter.

> *"[...] Future work should focus on the implementation within the hardware of real-time computation of the motion corrections, for improved online QC and overall better quality data delivered from the vessel. [...] Pre-stack receiver deghosting, in particular, remains challenging because of the effect of wave motion on receiver ghost variability. It should be tackled both at the hardware level (e.g., development of suitable accelerometer sensors, increase in the number of receivers, and decrease in the receiver interval) and at the level of efficient pre-stack receiver deghosting techniques."* [1]

The problem is that, unlike conventional seismic streamers, the streamers used for UHR offshore seismic acquisition contain no coordinate measurement systems like Real-Time-Kinematic (RTK) or Global Positioning Systems (GPS) and no underwater positioning modules like Inertial Navigation Sytems (INS) along the streamer. This problem implies that the locations and depths of the hydrophones must be interpolated between the head and tail buoys of the streamer.

In (U)HR seismics, methods are generally comparable to exploration seismics using higher-frequency sources where the wavefields are spatially and temporally sampled at a higher rate to avoid aliasing effects in the data. Source and receiver spacing is therefore significantly shortened with typical array length <100 m and bin sizes <5 m, as shown in Figure 4.1. The arrays are also typically towed at the surface or at shallow depths, as was seen in Chapter 3, to avoid ghost notches in the frequencies of interest in the data. Marine (U)HR seismic literature presents complex processing schemes, which require significant time, computational power, and human input to resolve high-resolution marine statics, complex receiver ghosts, and poor regularization that do not respond to typical processing methods due to limited far-offsets, missing low frequencies and mitigating factors during acquisition [1], [2], [4]. These issues are further exacerbated by the industry's transitions to full 3D (U)HR systems and could be remediated by improving the quality of the positioning of the data and real-time depth QC during acquisition [5].

Without conventional positioning systems available on the streamer itself, poor knowledge of the lateral and vertical receiver positions is primarily caused by weather conditions, steering, and pitch/yaw movement of the vessel [6], [7]. Weather specifically has become a severe limiting factor regarding the execution of (U)HR surveys causing significant costs due to delays when conditions are not favorable, as shown in Figure 4.2. Furthermore, vessel steering often prevents the survey from being continuous as data can only be recorded when the vessel is traveling at a relatively constant speed and

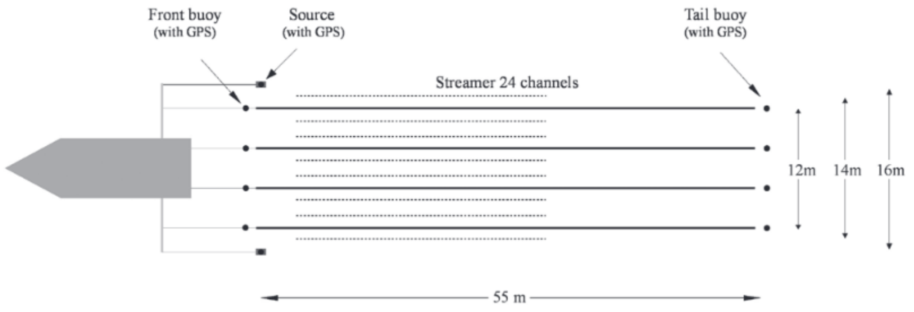

FIGURE 4.1. – *Illustration of a UHR3D streamer presented by Monrigal et al. [3] showing that GPS beacons are only present at the sources and head/tail buoys of the multi-channel streamers.*

in a relatively straight line since the position of the hydrophone in the water must be interpolated between the head and the tail buoy. These factors may cause significant issues regarding repeatability as the exact position of the receivers may deviate from the streamer models used in data processing.

According to Wardell et al. [8] when source frequencies reach 1kHz, the positioning resolution should be <10 cm. Current high-resolution global-positioning methods fall within two categories : satellite-based and fixed-point-based. Global Navigation Satellite System like GPS provide good coverage around the globe but may suffer from lower accuracy (>10 cm) while higher accuracy systems like RTK provide centimeter-level accuracy but require nearby referral stations. Positioning providers can provide very high-resolution global positioning by combining these methods resulting in an accuracy of 3 cm and 6 cm in the horizontal and vertical planes, respectively [9], [10]. Inertial Navigation Systems (INS) are also commonly found on conventional seismic streamers. They are made-up of a set of instruments that typically include gyroscopes, accelerometers and pressure gauges, using dead-reckoning methods to continuously track the positions of hydrophones during a surveys. These systems rely on discrete measurements that can suffer from accuracy drift over time due to environmental factors and sensor limitations [11], [12]. These sensors further struggle to compensate for lateral drift and wave height when the streamer is floating on the surface. Moreover, they provide discrete point measurements, contributing to increased equipment costs and load on the vessel. Therefore, none of these established exploration seismic technologies have made it to UHR streamer surveys while the short arrays, high sampling, and near-surface towing make

FIGURE 4.2. – *Examples of weather conditions during UHR seismic surveys in the field, with calm weather conditions (left) and rougher weather conditions (right). Images courtesy of GEOMarine Survey Systems.*

UHR seismics uniquely sensitive to even small motion and positioning errors.

In general, receiver positioning is critical for a wide range of seismic processing workflows because the geometry of the acquisition directly influences how recorded wavefields are interpreted and combined. In migration and imaging, for example, the exact locations of sources and receivers determine the calculated travel times and raypaths, and even small positioning errors can lead to misaligned reflections, blurred images, or artifacts. Similarly, in velocity analysis and tomographic inversion, receiver mispositioning propagates into inaccurate velocity models, which in turn degrade the resolution of the final subsurface image. Multiple processing steps that rely on coherent stacking, such as common-midpoint stacking, also assume precise receiver locations to correctly align traces from different offsets; misalignment reduces the signal-to-noise ratio and can distort the amplitude. Furthermore, advanced techniques like pre-stack depth migration, reverse-time migration, and FWI are especially sensitive to receiver geometry, as their algorithms explicitly model wave propagation and scattering; errors in the positioning can produce erroneous wavefield predictions, slow convergence, or false structures in the inverted model. Even in processes like deghosting or AVO analysis, knowing the exact receiver depth and lateral position is useful to correctly account for interference effects and amplitude variations. Overall, the fidelity of nearly every modern seismic processing workflow hinges on precise receiver positioning, making it a fundamental requirement for both imaging accuracy and quantitative interpretation.

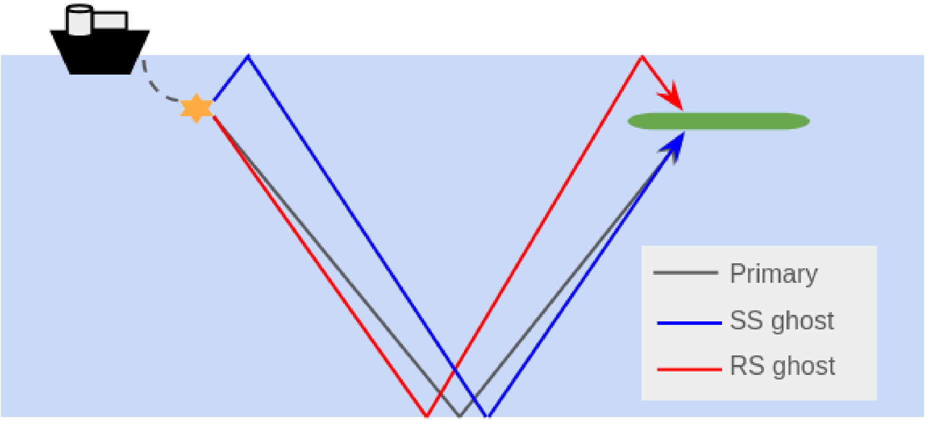

FIGURE 4.3. – *Acoustic wave paths causing interference (or ghosts) in UHR seismic data. . The star represents a seismic source, the green bar represents the streamer. SS stands for Source-Side and RS stands for Receiver-Side.*

When dealing with spatially poorly constrained UHR data, the interference caused by Source-Side (SS) and Receiver-Side (RS) ghost notches in the frequency spectra needs to be corrected. Even though, sometimes this data-degradation effect can be used to estimate the depth of hydrophones, it does not resolve lateral positioning uncertainty. Ghosts occurs when energy reflected from the sea surface interferes with the primary wavefield when the source and/or the hydrophone lies below the surface during acquisition. In this scenario, the sea surface acts as a near-perfect reflecting free-surface. Figure 4.3 illustrates the different raypaths that a wavefield could take from the source to the hydrophone; any reflection from the water–air interface is almost fully sent back toward the seafloor but with a reversed phase. The delayed, phase-inverted ghost arrival interferes destructively with the direct arrival, carving out equidistant notches in the frequency spectrum.

Looking at the North Sea dataset presented in Chapter 3, the effects of RS ghosts were limited to the upper edge of the frequency spectrum by towing the streamer at shallow depth. Any ghosts that would be present in the data would vary with offset as the streamer is flexible. During the survey, a QC step was performed to ensure that the interpolated receiver depths stay at 0.5 ± 0.1 m. We can use a trace-by-trace inversion approach of the apparent ghost notch to invert for the apparent receiver depth in the data and compare

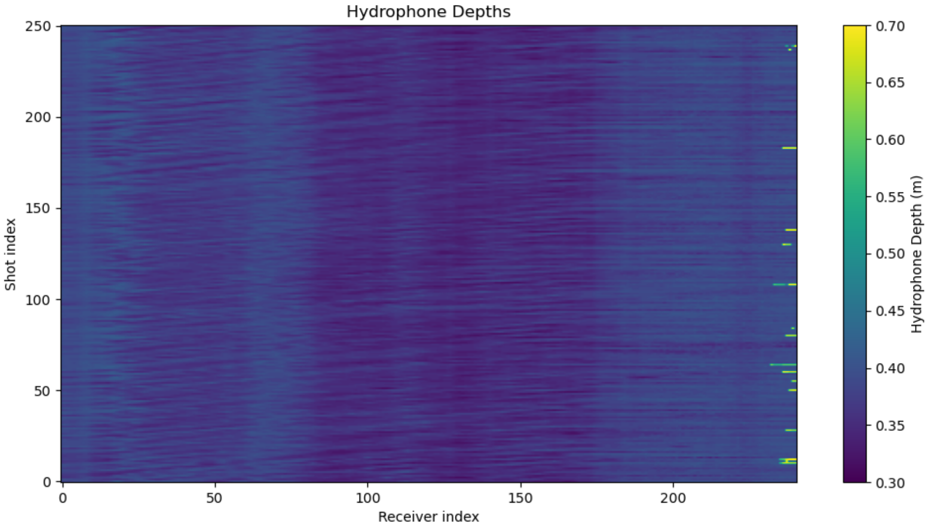

FIGURE 4.4. – *Hydrophone depth estimated using trace-by-trace ghost delay inversion assuming vertical propagation from the free-surface.*

them to the recorded depths.

The ghost appears as a delayed and inverted copy of the source signal, with its delay determined by the hydrophone depth. In the literature they can be used to determine the hydrophone depths like in the approach demonstrated by Vrolijk et al. 2017 [13] taking into account sea-surface wave effects or the approach from Provenzano et al. 2020 that successfully demonstrates using the depth- and angle-dependent estimated ghost operator to subsequently attenuate the ghost notches in the spectrum and recover original bandwidth. A more simplistic analysis was performed on the windfarm field data discussed in Chapter 3. The recorded pressure trace $p(t)$ can be modeled as

$$p(t) = s(t) - a\,s(t-\tau), \tag{4.1}$$

where $s(t)$ is the source wavelet, τ is the two-way travel time (ghost delay) from the hydrophone to the sea surface, and a is the ghost amplitude scaling. To invert for the maximum effective depth of the hydrophones per shot [14], we will consider the case of perfect vertical reflection from the free-surface. In other words, the case the ghost time delay is only caused by vertical propagation. This assumption is mostly valid for the very shallow reported towing depth of 0.5 m ±0.1 m and the relative short offsets of 120 m. In this case, assuming vertical propagation, the hydrophone depth d can be related to the ghost time delay by

$$\tau = \frac{2d}{c}, \tag{4.2}$$

with c being the sound speed in water. In the frequency domain,

$$P(\omega) = S(\omega)\left[1 - a e^{-i\omega\tau}\right], \tag{4.3}$$

where the bracketed term acts as a ghost filter $G(\omega) = 1 - a e^{-i\omega\tau}$ modifying the source spectrum. To invert for τ, the deghosted spectrum of the primary is defined as

$$P_{deghost}(\omega) = P(\omega) \cdot \frac{G^*(\omega)}{|G(\omega)|^2 + \epsilon} \quad , \tag{4.4}$$

where $G^*(\omega)$ represents the complex conjugate of the ghost filter, and ϵ is a stabilisation factor. The residual between the modelled and observed spectra is then given by

$$R(\omega) = P(\omega) - P_{deghost}(\omega) \tag{4.5}$$

$$= P(\omega) - P(\omega) \cdot \frac{G^*(\omega)}{|G(\omega)|^2 + \epsilon}. \tag{4.6}$$

The objective function measures the fraction of the signal explained by the ghost model :

$$F_{obj}(\tau, a) = 1 - \frac{\sum_{\omega \in \text{band}} |R(\omega)|^2}{\sum_{\omega \in \text{band}} |P(\omega)|^2}. \tag{4.7}$$

Maximizing this function over candidate τ values identifies the best ghost parameters. The hydrophone depth is then computed directly as

$$d = \frac{c\,\tau_{\text{best}}}{2}. \tag{4.8}$$

For the North Sea windfarm UHR data, the search range for τ were defined based on the expected reported towing depth (including a margin) such that

$$\tau_{\text{min}} = 0.0005 \text{ s}, \quad \tau_{\text{max}} = 0.0009 \text{ s}, \quad N_\tau = 120.$$

Results of the inversion are shown in Figure 4.4. Although the frequency-domain inversion retrieved realistic depth variations, the results did not match the reported streamer depths within their stated uncertainty. In fact, the inverted hydrophone depths were often shallower than the nominal towing depth of 0.5±0.1, as seen in Figure 4.6. In this workflow, the hydrophone depth is derived from the time delay assuming vertical propagation only (Equation

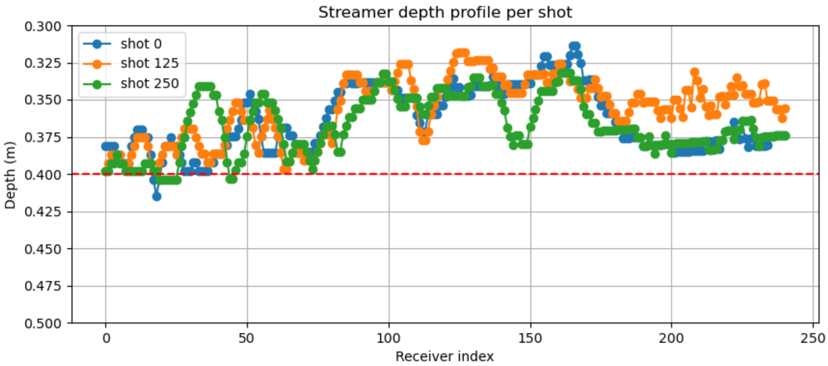

FIGURE 4.5. – *Inverted hydrophone depths for shot index 0, 125 and 250; the dotted red line shows the recorded minimum towing depth during the survey.*

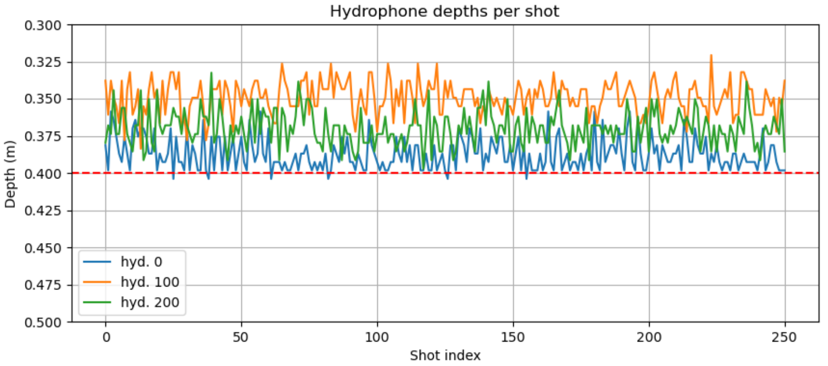

FIGURE 4.6. – *Inverted depths over all shots for hydrophone index 0, 100 and 200; the dotted red line shows the recorded minimum towing depth during the survey.*

4.2). When taking into account horizontal offsets from the angle of reflection α where the time delay becomes

$$\tau = \frac{2d \cdot \cos(\alpha)}{c} \tag{4.9}$$

where α is the reflection (or incidence) angle. The inversion therefore retrieves an effective depth $d' = d\cos(\alpha)$, rather than the true streamer depth d. As α increases with offset, d' decreases, which explains why the frequency-domain inversion predicts systematically shallower hydrophone depths at larger offsets, explaining the trend visible in Figure 4.5 from hydrophone index

0-150. In other words, the observed trend in the inverted depths is a geometric artifact arising from angle-dependent propagation. This also clarifies why the inverted depth begins to increase again at the far offsets. For the field data, deeper primaries that are associated with smaller reflection angles, become more dominant than the large-angle surface-related multiples at wide offsets. As a result, the effective d' approaches the true depth again, consistent with the upturn seen in Figure 4.5. Thus, the overall shape of the inverted curve is physically reasonable and expected from the angle-dependent formulation.

This does not exclude the presence of genuine depth variations along the streamer, such as the smaller-scale ‘wiggles’ observed in the inversion results. Figure 4.4 shows some coherent striping along the receiver index which is supported by Figures 4.5 and 4.6. This pattern could reflect hydrophone sensitivity variations or calibration inconsistencies, and possibly residual geometric effects from kinking or uneven tension in the streamer during storage or deployment. It must be said that estimating receiver depth from ghost notches becomes unreliable when both source- and receiver-side ghosts overlap or vary across offsets due to the reflection angle α during deep towing or when survey conditions become too "rough" when shallow towing. In the case of the former, the spectral notches merge or shift, creating non-unique solutions for the ghost delay. In the case of the latter, complications arise from amplitude variations caused by sea-surface roughness and streamer flexing, which violate the assumptions of a single, stationary ghost delay per trace. These factors limit the effectiveness of purely processing-based receiver-depth estimation in real UHR acquisition environments.

The field experience and inversion results collectively point toward a broader conclusion : improving UHR imaging quality may depend more on acquisition design than on post-processing. Real-time motion sensing, denser receiver arrays, and improved streamer stabilisation could reduce the variability that processing must later correct. By addressing positioning and ghost issues during acquisition, rather than compensating for them afterward, UHR surveys could achieve more consistent resolution and repeatability—pushing the practical limits of shallow-marine imaging.

Based on the limitations of UHR seismic surveys in practice presented above, our focus shifted toward developing methods to accurately determine receiver positions and trim variations along a streamer during UHR seismic surveys. We focused on developping methods that would support the low-cost, fast turn-around philosophy that often applies to projects requiring offshore

UHR seismic surveys. In Chapters 5 and 6, we present a methodology based on Fiber Optic Shape Sensing (FOSS) technology, whereby distributed strain measurements along an embedded optical fibre are employed to reconstruct the 3D geometry of the streamer, instantaneously and in real-time. This approach may enable precise monitoring of streamer deformation and hydrophone placement, providing a direct means to improve the fidelity of UHR data acquisition and subsequent processing.

RÉFÉRENCES

[1] H. DUARTE, N. WARDELL et O. MONRIGAL, « Advanced processing for UHR3D shallow marine seismic surveys », *Near Surface Geophysics*, t. 15, n° 4, p. 347-358, 2017, ISSN : 1873-0604. DOI : `https://doi.org/10.3997/1873-0604.2017022`. adresse : `https://www.earthdoc.org/content/journals/10.3997/1873-0604.2017022`.

[2] S. V. BURYAK et S. A. VAKULENKO, « Challenges and modern techniques of multichannel shallow marine seismic processing », t. 2019, n° 1, p. 1-5, 2019, ISSN : 2214-4609. DOI : `https://doi.org/10.4133/sageep.32-078`. adresse : `https://www.earthdoc.org/content/papers/10.4133/sageep.32-078`.

[3] O. MONRIGAL, I. de JONG et H. DUARTE, « An ultra-high-resolution 3D marine seismic system for detailed site investigation », *Near Surface Geophysics*, t. 15, n° 4, p. 335-345, 2017. DOI : `https://doi.org/10.3997/1873-0604.2017025`. eprint : `https://onlinelibrary.wiley.com/doi/pdf/10.3997/1873-0604.2017025`. adresse : `https://onlinelibrary.wiley.com/doi/abs/10.3997/1873-0604.2017025`.

[4] M. J. FAGGETTER, M. E. VARDY, J. K. DIX, J. M. BULL et T. J. HENSTOCK, « Time-lapse imaging using 3D ultra-high-frequency marine seismic reflection data », *GEOPHYSICS*, t. 85, n° 2, P13-P25, 2020. DOI : `10.1190/geo2019-0258.1`. eprint : `https://doi.org/10.1190/geo2019-0258.1`. adresse : `https://doi.org/10.1190/geo2019-0258.1`.

[5] L. MACGREGOR, L. SCOTT, R. COOPER et J. NICHOLLS, « Ultra-High Resolution Seismic : Applications of P-Cable in the Energy Transition », *First Break*, t. 40, n° 11, p. 67-70, 2022, ISSN : 1365-2397. DOI : `https://doi.org/10.3997/1365-2397.fb2022096`. adresse : `https://www.earthdoc.org/content/journals/10.3997/1365-2397.fb2022096`.

[6] V. HLEBNIKOV, T. ELBOTH, V. VINJE et L.-J. GELIUS, « Noise types and their attenuation in towed marine seismic : A tutorial », *GEOPHYSICS*, t. 86, n° 2, W1-W19, 2021. DOI : `10.1190/geo2019-0808.1`. eprint : `https://doi.org/10.1190/geo2019-0808.1`. adresse : `https://doi.org/10.1190/geo2019-0808.1`.

[7] G. BLACQUIÈRE et H. Ö. SERTLEK, « Modeling and assessing the effects of the sea surface, from being flat to being rough and dynamic », *GEOPHYSICS*, t. 84, n° 2, T13-T27, 2019. DOI : 10.1190/geo2018-0294.1. eprint : https://doi.org/10.1190/geo2018-0294.1. adresse : https://doi.org/10.1190/geo2018-0294.1.

[8] N. WARDELL, P. DIVIACCO et R. SINCERI, « 3D pre-processing techniques for marine VHR seismic data », *First Break*, t. 20, août 2002. DOI : 10.1046/j.1365-2397.2002.00291.x.

[9] C. SPECHT, J. PAWELSKI, L. SMOLAREK, M. SPECHT et P. DĄBROWSKI, « Assessment of the Positioning Accuracy of DGPS and EGNOS Systems in the Bay of Gdansk using Maritime Dynamic Measurements », *Journal of Navigation*, t. 72, p. 575-587, mai 2019. DOI : 10.1017/S0373463318000838.

[10] FUGRO, *Fugro Starfix®*, Brochure. adresse : https://www.fugro.com/our-services/marine-asset-integrity/satellite-positioning/starfix#tabbed4.

[11] U. JURADO, P. WILSON, P. BLONDEL *et al.*, « Underwater Localization System for Marine Seismic Airgun Arrays Validated Through Robotics », *International Journal of Intelligent Robotics and Applications*, t. 9, p. 1255-1267, 2025. DOI : 10.1007/s41315-025-00429-3.

[12] H. ZHANG, K. SANG, B. YANG, C. DUAN, L. LV, C. KUANG et H. LIU, *A Spline Curve Fitting Model for Towed Streamer Positioning in Marine Seismic Exploration*, 2025. DOI : 10.3390/s25165114. adresse : https://www.mdpi.com/1424-8220/25/16/5114.

[13] J.-W. VROLIJK et G. BLACQUIERE, « Shot-based deghosting for variable sea surface and receiver depth », p. 4887-4892, août 2017. DOI : 10.1190/segam2017-17742156.1.

[14] G. PROVENZANO, T. J. HENSTOCK, J. M. BULL *et al.*, « Attenuation of receiver ghosts in variable-depth streamer high-resolution seismic reflection data », *Marine Geophysical Research*, t. 41, p. 11, 2020. DOI : 10.1007/s11001-020-09407-9. adresse : https://doi.org/10.1007/s11001-020-09407-9.

The full quote from the conclusions of Duarte et al., 2017, on the focus of future work in UHR3D acquisition :

> "The most recent processing results of 3D data acquired in seas with waves in excess of 1.5–2 m are particularly telling. The imaging quality after migration is strong evidence that processing flows, tailored to the specificities of UHRS data, can actually preserve signal resolution and significantly improve signal-to-noise ratio (Figure 13). In its current status, UHRS processing already preserves amplitude and phase with enough fidelity for relevant analysis of attributes of horizons for various applications such as the study of the foundations of shallow-water structures such as bridges and wind turbines (Figure 14).
>
> Future work should focus on the implementation within the hardware of real-time computation of the motion corrections, for improved online QC and overall better quality data delivered from the vessel. Furthermore, processing of broadband UHRS should address the importance of minimising artefacts from the deghosting process, already identified for lower resolution broadband applications (Reilly 2016). Pre-stack receiver deghosting, in particular, remains challenging because of the effect of wave motion on receiver ghost variability. It should be tackled both at the hardware level (e.g., development of suitable accelerometer sensors, increase in the number of receivers, and decrease in the receiver interval) and at the level of efficient pre-stack receiver deghosting techniques."

5

FOSS FOR STREAMER-SHAPE TRACKING : THEORY AND SENSOR DESIGN

The technology of FO shape sensors allows remote and instantaneous monitoring of the path taken by the sensor in a dynamic environment. It follows that, perhaps, this technology could be useful to resolve the hydrophone positioning problem in UHR marine seismic data.

In this chapter, we explore the basic theory of fibre optic shape-sensing and describe the procedures and considerations involved in the process of deployment and the steps required for reliable and repeatable measurements for geotechnical applications.

5.1. INTRODUCTION

Fiber Optic (FO) sensing has emerged as an indispensable technology as it enables the precise and real-time monitoring of various physical parameters. FO sensing leverages the inherent advantages of extruded silica, including flexibility, durability, immunity to electromagnetic interference, high sensitivity, and low signal loss over long distances [1], [2]. FO sensing operates on the principle of exploiting changes in light characteristics, as the light propagates through the fibre. These changes can be induced by a variety of physical phenomena, including strain, temperature, pressure, and vibration. In geophysics and seismology, FO sensing is often synonymous with Distributed Acoustic Sensing (DAS) where it is used to detect external acoustic wavefields propagating through the fibreglass medium [3], [4]. Another application of FO sensing is Fiber Optic Shape-Sensing (FOSS), which enables the reconstruction of the path taken by an object remotely, instantaneously, and in 3D. Although the hardware is similar to that used in DAS, the aim of FOSS is to measure the strain caused by the bending of a sensor itself and reduce/eliminate the effects of external wavefields and environmental noise. This technology was originally developed in robotics, in the medical fields to enable the precise tracking of catheters or endoscopes within the human body and in the industrial engineering field to monitor structural health and movement over time [5]-[7].

The form of a FOSS sensor will differ between applications. For example, when attached to a catheter, the goal is to attain extremely high accuracy and resolution over short sensing lengths in order to precisely reconstruct the path taken by the instrument. Meanwhile, in industrial engineering, the focus is to extend the sensing length to monitor the deflection of large structures like railways and bridges [9]. Inherently, these different forms of FOSS result in specialized sensing methods and sensor designs, which best suit the respective sensing requirements. Medical FO shape sensors are typically engineered from highly specialized fibres, from which the individual extended-range cores are carved out on a micrometer scale [10]. These specialized fibres are then often optically marked with Fiber Bragg Gratings, enabling precise strain measurements discretely along the sensor, as shown in Figure 5.1. These sensors are centimeters to a few meters long and designed to monitor the path of the instrument remotely, in real-time, and in the highly dynamic environment that is the human body [11]. On the other end, in civil engineering, FO shape sensors may take the form of long telecommunication optical fibres that are permanently embedded into a structure in various patterns, as shown in Figure 5.2. These sensors will be tens to hundreds of meters long and cannot rely on high-precision FBG strain sensing due to optical signal attenuation. Instead, Distributed Fiber Optics Sensors (DOFS) are used, which offer spatially resolved data along the entire length of the optical fibre. These sensors provide lower spatial resolution and accuracy but greatly increase the useful sensing length. They also regularly exploit the plug-and-play feature of FO sensing by permanently leaving the sensor inside structures and only interrogating the fibres based on the monitoring schedule [12], [13]. Looking at the applications available to FOSS technology in the geophysical and geotechnical fields, it is important to consider the design and

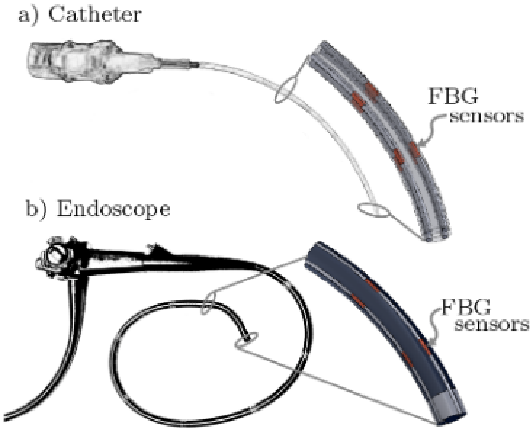

FIGURE 5.1. – *Figure sourced from [8] : "Multi-core optical fibres can be placed in numerous flexible medical instruments due to their small size, flexibility, light weight, immunity to electromagnetic interference and compatibility with medical-imaging modalities. Fibers with Bragg Gratings (FBG) are shown embedded in a) a catheter and b) an endoscope." This figure shows the typical application of FOSS in medical instruments, specifically the short sensing length, use of FBGs, limited sensor width and free floating shape-sensing of flexible structures.*

implementation of the sensor.

5.2. THEORY OF FIBER OPTIC SHAPE-SENSING

Using FOSS, we can remotely monitor the curvature and 3D shape of an element or instrument over increased sensing length. This is enabled by measuring the mechanical strain in individual fibreglass cores using a technique called FO strain sensing. A typical FOSS sensor contains several cores which act as independent extended-range elements. Figure 5.3 shows a conceptual bending of a rod with two embedded strain-sensing cores. Cores above the neutral plane of bending (laying at the geometrical center of the sensor) would experience extensional strain while cores below this plane would experience compressional strain. Evaluating the strain of multiple cores at all points along the cores allows us to compute the bending throughout the sensor. The minimum number of cores necessary for 3D-FOSS is three but the more cores are embedded, the higher the accuracy of the shape

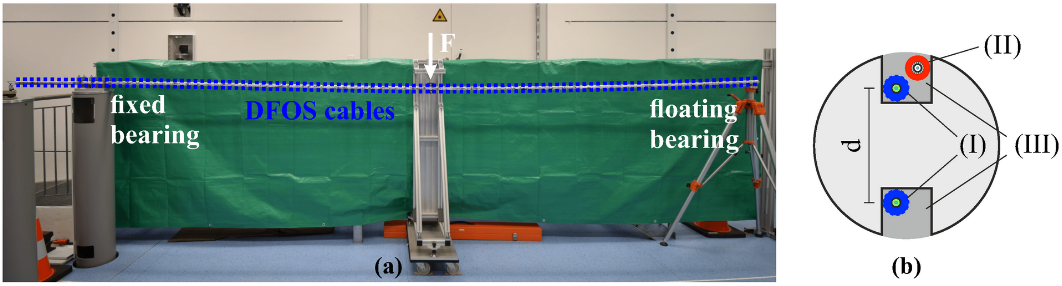

FIGURE 5.2. – *Figure source from [9] : "Laboratory testing of steel rod specimen perfomed by [5] : (a) Practical test setup. (b) Installation scheme with (I) extended-range cable, (II) temperature sensing cable, and (III) gluing groove." This figure shows the typical application of FOSS in structural-health monitoring, specifically the extended sensing length, use of Distributed Fiber Optic Sensors (DFOS), the embedding into solid structures, and necessary sensitivity to small curvature differentials.*

reconstruction. The cores are most often placed radially symmetrically and must be attached at all points to their common cladding to ensure the entire sensor system deforms as a uniform unit. The shape reconstruction of a sensor using FOSS occurs in three stages : strain-sensing along all fibre cores, computing path variables from strain measurements, and shape reconstruction using differential geometry methods.

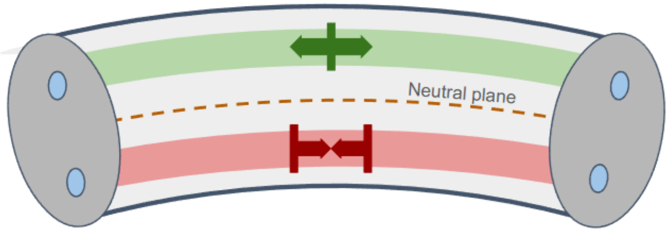

FIGURE 5.3. – *Conceptual bent rod showing two embedded cores (light blue circles) and the neutral plane of bending (orange dashed line). The core above the neutral plane experiences extensional strain (green) while the core below the plane experiences compressional strain (red) due to bending.*

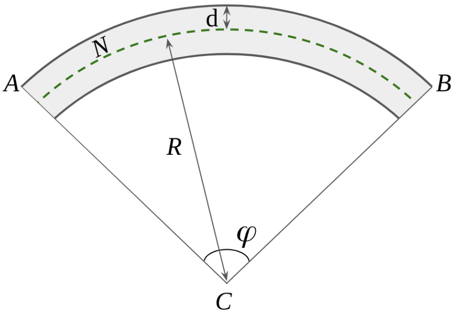

FIGURE 5.4. – *Rectangular cross-section of a rod under bending strain. The neutral plane of bending N is denoted by the dotted green line with a radius of curvature R from the center of rotation C. The angular distance due to bending from A to B is the angle of rotation φ. The outer boundary of the beam AB lays at a distance d from the neutral axis.*

5.2.1. DERIVING PATH VARIABLES FROM STRAIN VALUES OF MULTIPLE CORES

Firstly, we aim to derive the discrete sets of curvature (κ) and bend direction (θ_b) at specific measurement locations (s) along the fibre which correspond to the strain measurements of multiple cores. To understand this process, we first observe the relationship between strain and curvature of a 3D rod. Strain (ε) can be described as the relative change in length of a material due to deformation such that $\varepsilon = \frac{\Delta L}{L}$. Figure 5.4 represents the rectangular cross-section of a rod undergoing bending. The neutral axis N passes through the geometrical center of the rod and experiences no strain during deformation. Any material laying above or below N will experience positive or negative strain, equivalent to extensional and compressional strain, respectively. In this case, the strain at the outer boundary AB can be described as

$$\varepsilon_{AB} = \frac{\Delta L}{L} = \frac{AB - N}{N} = \frac{(R+d)\varphi - R\varphi}{R\varphi} = \frac{d}{R}, \tag{5.1}$$

where R is the radius of curvature, φ is the angle of rotation at the center of rotation C and d is the distance from the neutral plane. The radius of curvature R can be expressed as the inverse of the curvature modulus κ, which allows us to express the strain in terms of the curvature and distance from the neutral plane :

$$\varepsilon_{AB} = \kappa d. \tag{5.2}$$

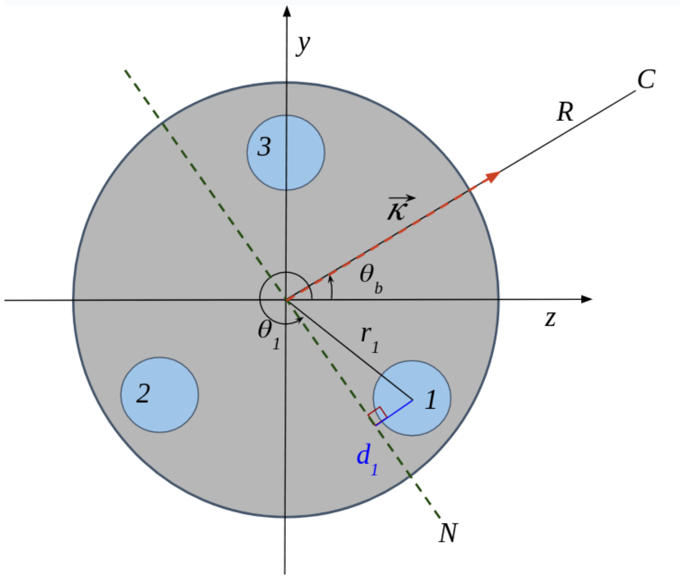

FIGURE 5.5. – *Circular cross-section of a bent rod containing three strain-sensing cores at a distance r from the center of the rod. The curvature vector $\vec{\kappa}$ has the length κ that is the inverse of the radius of bending R and points towards the center of rotation C. The neutral plane N passes through the geometrical center of the rod, perpendicular to the direction of curvature. θ_b and θ_1 are the angular distance of the curvature vector and the 1st core from the z-axis in the arbitrary reference frame respectively.*

In the case of FO shape sensors, we are considering the strain measurements with three cores, evenly radially distributed in the sensor sheath. As the sensor is bent, the cores and sheath deform as a uniform unit, also known as a Kirchhoff rod [14]. Figure 5.5 shows the circular cross-section of this hypothetical sensor being bent towards the center of rotation C. Again, the neutral plane runs through the geometrical center of the system, perpendicular to the curvature vector $\vec{\kappa}$ (with curvature modulus κ), which points in the direction of the center of rotation C. In this case, we observe that the distance from the neutral plane of each core d_i is the shortest perpendicular distance from each core to N. As can be seen in the angles shown in Figure 5.5, for a core i, we can say that

$$d_i = r_i \cos(\theta_b - \theta_i), \tag{5.3}$$

and, therefore,

$$\varepsilon_i = \kappa r_i \cos(\theta_b - \theta_i), \tag{5.4}$$

where θ_b and θ_i are the angular distance of the curvature vector ($\vec{\kappa}$) and the i-th core from the z-axis in the arbitrary reference frame, respectively. Using this formulation, we have expressed the strain of a core in terms of the components of the curvature vector $\vec{\kappa}$: its direction θ_b and modulus κ. All other variables are known from the geometry of the sensor and the location of each core in terms of an arbitrary frame. However, the solution for Equation 5.4 is non-unique due to the nature of the cosine function; therefore, the true direction of bending θ_b cannot be properly evaluated. To retrieve a unique solution, we can combine the curvature components into a closed-form solution, expressing the complete curvature vector $\vec{\kappa}$ for a single core i in terms of its local axis components [15]

$$\vec{\kappa}_i = \frac{\varepsilon_i}{r_i}(\cos(\theta_i)\hat{j} + \sin(\theta_i)\hat{k}), \tag{5.5}$$

where $\vec{j}$ and $\vec{k}$ are orthogonal unit vectors, which align with axes of the local frame. To compute the total apparent curvature $\vec{\kappa}$ using strain information from all cores N_c, we can simply sum all respective curvatures as

$$\vec{\kappa} = \sum_{i=1}^{N_c} \frac{\varepsilon_i}{r_i}\cos(\theta_i)\hat{j} + \sum_{i=1}^{N_c} \frac{\varepsilon_i}{r_i}\sin(\theta_i)\hat{k}. \tag{5.6}$$

As previously mentioned, the curvature $||\kappa||$ corresponds to the length of the curvature vector and the bending angle θ_b is the angle of the curvature vector compared to the reference frame :

$$||\kappa|| = \sqrt{\kappa_y^2 + \kappa_z^2}, \tag{5.7}$$

$$\theta_b = \text{angle}(\vec{\kappa}) = \arctan(\frac{\kappa_z}{\kappa_y}). \tag{5.8}$$

Further, we can derive the angle of rotation φ and the radius of curvature R by using the distance between two strain measurements Δs, similar to the distance between A and B in Figure 5.4, as well as torsion, which is the 1D spatial derivative of θ_b along the fiber [15] :

$$R = \frac{1}{\kappa}, \tag{5.9}$$

$$\varphi = \frac{\Delta s}{R}, \tag{5.10}$$

$$\tau = \theta_b'. \tag{5.11}$$

With these equations, we obtain the local curvature, angle of bending, radius of curvature and the rotation angles which correspond to strain measurements taken by extended-range cores at specific locations along the sensor. This operation requires precise knowledge of the geometry of the sensor, including the distance between consecutive measurements as well as the angular and radial distance of each core from the geometrical center of the sensor. With multiple strain measurements throughout the sensor, it is possible to reconstruct the 3D path taken by the sensor using different numerical methods detailed in the next subsection.

5.2.2. NUMERICAL METHODS FOR PATH RECONSTRUCTION

FRENET-SERRET FRAMES

Every point s along a fibre can be described by a 3D orthogonal frame with respect to the observation frame [16]. The orthogonal frame is composed of its normal $\vec{N}(s)$, tangent $\vec{T}(s)$ and binormal $\vec{B}(s)$, as shown in Figure 5.6. The relationship between the unit vector orthogonal components can be described using the previously derived curvature modulus κ and torsion τ such that

$$\begin{aligned} \vec{T}'(s) &= \kappa(s)\vec{N}(s), \\ \vec{N}'(s) &= -\kappa(s)\vec{T}(s) + \tau(s)\vec{B}(s), \\ \vec{B}'(s) &= -\tau(s)\vec{N}(s), \end{aligned} \tag{5.12}$$

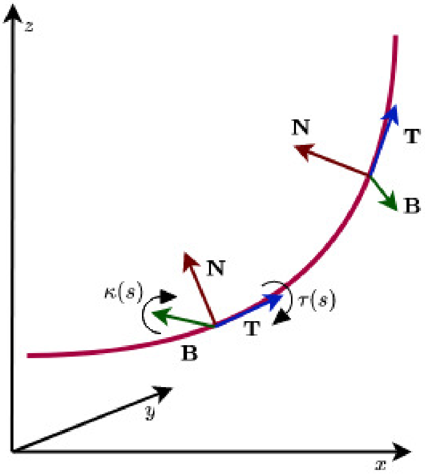

FIGURE 5.6. – *Example of Frenet-Serret frames along a 3D path showing the tangent vector (blue arrow) modulated by the torsion τ and the binormal vector (green arrow) modulated by the curvature κ between two points along a curve (red line) and their respective normal vector (red arrow).*

where $'$ denotes a differentiation with respect to s and the torsion is derived from the bending direction such that $\tau(s) = \theta'(s)$. If the curvature and torsion are explicitly defined, the Frenet-Serret formulas can be solved and the position of point $\vec{r}(s)$ can be determined using the tangent unit vector :

$$\vec{r}(s) = \int \vec{T}(s)ds + \vec{r}_0. \tag{5.13}$$

where $\vec{r}_0 = \vec{r}(s_0)$ is the origin of the curve. The system of equations that iteratively solves the Frenet-Serret partial differential equations is given by

$$\begin{aligned}
\vec{N}_{i+1} &= \frac{\Delta s(\tau_i\ \vec{B}_i - \kappa_i\ \vec{T}_i)}{1 + \Delta s^2\ \tau_i^2 + \Delta s^2\ \kappa_i^2}, \\
\vec{T}_{i+1} &= \Delta s\ \kappa_i\ \vec{N}_{i+1} + \vec{T}_i, \\
\vec{B}_{i+1} &= -\Delta s\ \tau_i\ \vec{N}_{i+1} + \vec{B}_i, \\
\vec{r}_{i+1} &= \Delta s\ \vec{T}_{i+1} + \vec{r}_i,
\end{aligned} \tag{5.14}$$

where Δs is the distance between the strain measurements along the sensor [17]. To locate the start and orientation of a curve in space, we can define the initial conditions at the origin $\vec{r}_0 = [0,0,0]$ where $\vec{T}_0 = [1,0,0]$, $\vec{N}_0 = [0,1,0]$ and the binormal at the origin is obtained from their cross-product such that $\vec{B}_0 = \vec{T}_0 \times \vec{N}_0$. We also define the initial bending $\tau_0 = 0$ and curvature $\kappa_0 = 0$.

TRANSFORMATION MATRICES

The second commonly used method to reconstruct the path of the fibre is by using transformation-matrices properties. Our explanation replicates the work of [18]. The homogeneous transformation matrix $\mathbf{A}$ is composed of 3 main features : $\mathbf{R}^i_{i+1}$, which is a 3x3 rotation matrix that aligns the rotation of 2 frames; $\mathbf{o}^i_{i+1}$, which is the origin vector of the subsequent frame $i+1$ relative to frame i in 3D and $\mathbf{0}^T_3$, which is a 1x3 null vector

$$\mathbf{A}^i_{i+1} = \begin{bmatrix} \mathbf{R}^i_{i+1} & \mathbf{o}^i_{i+1} \\ \mathbf{0}^T_3 & 1 \end{bmatrix}. \tag{5.15}$$

Matrix $\mathbf{A}^i_{i+1}$ can be used to transform the homogeneous coordinates of a point $\vec{r}$ from origin frame 0 to frame $i+1$ such that

$$\vec{r}^{\,0}_{i+1} = \mathbf{A}^0_1\mathbf{A}^1_2...\mathbf{A}^{i-1}_i\mathbf{A}^i_{i+1}\mathbf{p}^{i+1}_{i+1} = \mathbf{A}^0_{i+1}\vec{r}^{\,i+1}_{i+1}. \tag{5.16}$$

We consider location s_i represented by the unit vectors (x_i, y_i, z_i). Further along the fibre the frame at position s_{i+1} is rotated along $\mathbf{z}_i$ by angle θ_i and around $\mathbf{y}_i$ by ϕ (taking x as the neutral axis in this case). The corresponding rotation matrices $\mathbf{R}$ are given by

$$\mathbf{R}_{z_i}(\theta_i) = \begin{bmatrix} \cos(\theta_i) & -\sin(\theta_i) & 0 \\ \sin(\theta_i) & \cos(\theta_i) & 0 \\ 0 & 0 & 1 \end{bmatrix}, \tag{5.17}$$

where θ corresponds to the bending angle derived from the curvature and ϕ is derived from the radius of curvature R and the distance s between the measurements at i and $i+1$, such that $R_i = \frac{1}{\kappa_i}$ and $\phi_i = \frac{ds}{R_i}$, and

$$\mathbf{R}_{y_i}(\phi_i) = \begin{bmatrix} \cos(\phi_i) & 0 & -\sin(\phi_i) \\ 0 & 1 & 0 \\ -\sin(\phi_i) & 0 & \cos(\phi_i) \end{bmatrix}. \tag{5.18}$$

The original frame at $i+1$ in terms of frame i can be described using the trigonometric relationship :

$$\boldsymbol{o}^i_{i+1} = \begin{bmatrix} R_i(1 - R_i\cos(\phi_\mathrm{i}))\cos(\theta_i) \\ R_i(1 - R_i\cos(\phi_\mathrm{i}))\cos(\theta_i) \\ R_i\sin(\phi_i) \end{bmatrix}. \tag{5.19}$$

Using these expressions, we can reformulate matrix $\boldsymbol{A}^i_{i+1}$:

$$\boldsymbol{A}^i_{i+1} = \begin{bmatrix} \cos(\theta_i)\cos\left(\phi_i\right) & -\sin(\theta_i) & \cos(\theta_i)\sin\left(\phi_i\right) & R_i\left(1-\cos\left(\phi_i\right)\right)\cos(\theta_i) \\ \sin(\theta_i)\cos\left(\phi_i\right) & \cos(\theta_i) & \sin(\theta_i)\sin\left(\phi_i\right) & R_i\left(1-\cos\left(\phi_i\right)\right)\sin(\theta_i) \\ -\sin\left(\phi_i\right) & 0 & \cos\left(\phi_i\right) & R_i\sin\left(\phi_i\right) \\ 0 & 0 & 0 & 1 \end{bmatrix}. \tag{5.20}$$

With a complete transformation matrix from points s_i to s_{i+1} we can reconstruct the complete 3D path of curve using its curvature and bending angle at every point. To reconstruct a complete path, we iteratively compute the transformation matrix $\boldsymbol{A}^i_{i+1}$ and cumulatively multiply all transformation matrices with the origin coordinates like $r_0 = [0,0,0,1]^T$.

5.3. FOSS PROCEDURES AND CONSIDERATIONS

When performing FOSS, regardless of the application type, similar procedural steps must be followed to obtain accurate and repeatable results.

1. **Sensor deployment :** Along with decisions regarding the sensor type and the interrogator type, it is important to consider the manner of embedding the sensor into the structure or instrument to be monitored. This can take the form of bonding the sensor to a part of structure like we have seen in Figure 5.2 or embedding the sensing fibres radially to the instrument itself like in Figure 5.1. Other embedding methods can include a free-floating sensor in air, in a liquid or in a gel or a partially free sensor in a lubricated channel. When considering the ideal embedding methods, certain factors should be considered; these include 1) the relationship between the maximum expected strain versus radial distance of individual cores and 2) the expected environment of deployment and related noise. The relationship between these factors is explained in more detail in Section 5.4.3.
2. **Taring :** Once the sensor is ready for operation, it can be connected to the interrogator and a taring measurement must be executed, which serves two crucial roles. Firstly, the sensor contains inherent background strain from fibre extrusion and sensor production, which is not linear and not predictable but does remain relatively constant. This background strain may change throughout the lifetime of the sensor as it is exposed to extended periods of high strains, thus the taring measurement must be repeated before each new deployment. Secondly, the taring measurement is necessary to record a state of zero differential strain from which to build the shape for the shape-sensing numerical methods. There are no guidelines for what this ‘zero-strain’ shape should be, the only important factor is that the shape is accurately recorded and can be numerically modelled.
3. **Strain measurements :** Once the tare measurement is made and the sensor is deployed, strain measurements can be executed. Most modern-day interrogators automatically convert the optical return signal into strain measurements. Due to the tare, all made measurements represent a differential strain state from the tared ‘zero-strain’ shape. Depending on the application, the strain measurements can be made continuously (e.g., in the case of monitoring a catheter in real-time during an operation) or instantaneously (e.g., monitoring the structural health of a beam or underground cable). The measurements can be made over a few seconds or over several years, which is one of the advantages of durable, FO-based sensors.
4. **Data processing :** Once the strain data is acquired, minimal processing is required to be able to perform a shape reconstruction. A typical

processing workflow will include removal of anomalous values and NaNs, interpolation and smoothing. Due to the nature of the strain being continuous in space and time as well as related between cores, we can imagine effective interpolation procedures including 2D interpolation and machine-learning-based interpolation schemes. A crucial factor in the accuracy and repeatability of the shape-sensing method is the inclusion of a central core in the shape sensor design, which allows the mitigation of elongation and compression of the sensor as well as environmental stimuli in order to isolate the strain caused by bending during data processing. Moreover, for some free-floating sensor applications, the inclusion of helically wound cores is crucial to model and mitigate twisting effects of the sensor. These effects would be handled during the data processing steps, they are explained in more detail in Section 5.4.2.

5. **Shape-sensing :** Once the strain due to bending has been isolated, the shape-sensing procedure can then be performed using the 'zero-strain' state as the shape to be subtracted from the reconstructed shape. Computationally, the data processing and shape reconstruction operations are negligible, allowing the shape reconstruction to be performed in real-time.
6. **Orientation in 3D space :** Finally, once the 3D shape of the sensor has been reconstructed, it must be placed in context of the monitored structure or within an understood geographical frame. This is achieved by aligning the first tangential vector to the correct orientation. This procedure may be rather trivial if the orientation of the sensor remains unchanged like when embedded into a large structure. On the other hand, this procedure may require additional positioning instruments or orientation reference frames for dynamic shape-sensing. These possibilities are discussed in more detail in Section 5.4.4.

5.4. DESIGNING A FOSS SENSOR FOR GEOPHYSICAL APPLICATIONS

As established above, the form of a FOSS sensor varies strongly based on the application and deployment, not only in the fibre embedding and sensor design but also in the interrogation method used to measure strain. It is useful to establish some design guidelines appropriate for geophysical and geotechnical applications based on current technologies, to inform the future implementations of FOSS in these fields. We expect to encounter two major components that would broadly characterize the usage of FOSS in geophysics (i.e., streamer-shape tracking) : extended sensing range and highly dynamic environment. We can thus immediately recognize the necessity to abstract specific aspects of existing FOSS technologies and adapt them to these new applications.

5.4.1. CHOICE OF INTERROGATOR

The choice of interrogator is crucial to enable the extended sensing range for geophysical applications. we propose that DOFS, that detect the spatial distribution of a measurand along the fibre, are best suited for large-scale FOSS. This is contrary to discrete measurements, like with FBGs. Despite the higher accuracy of the latter, the primary reasoning behind this determination is the inherent loss of signal over consecutive gratings preventing a successful high-resolution strain-sensing over large distances without requiring excessive interpolation between individual measurements [19]. DOFSs rely on inherent photonic scattering in an imperfect medium where atomic-scale variations act as scatter centers and the responses of several adjacent centers are combined to provide a measurement over a pre-determined length, called a gauge. As a photonic signal propagates along a transparent medium, it will scatter when encountering an imperfection in the atomic matrix and part of the energy will be backscattered towards the laser input. Backscattered light will experience some form of modulation like a shift in wavelength, which can be detected and attributed to a specific gauge along the fibre [1]. The key parameter to consider when selecting a DOFS technology is the strain sampling density- or the length of individual gauges. Shape reconstruction errors accumulate along the sensor, with accuracy highest at the beginning and decreasing toward the end. Ignoring instrument error and environmental noise, numerical experiments show that lower measurement resolution leads to a higher rate of compounded shape-sensing error, as shown as a unit-less numerical example in Figure 5.7. Since DFOSs average strain over the gauge length rather than measuring discrete local strain, high spatial resolution is essential for reliable shape reconstruction.

Based on available DOFS technologies, Optical Frequency Domain Reflectometry (OFDR) and Pulse-PrePump Brillouin Optical Time Domain Analysis (PPP-BOTDA) offer relatively long sensing lengths and small gauge lengths. A more detailed description of DOFS methods and OFDR is provided in Appendix A.

Based on current market availability, resolution, and sensing-range requirements, at the time of writing this chapter, we identify the LUNA

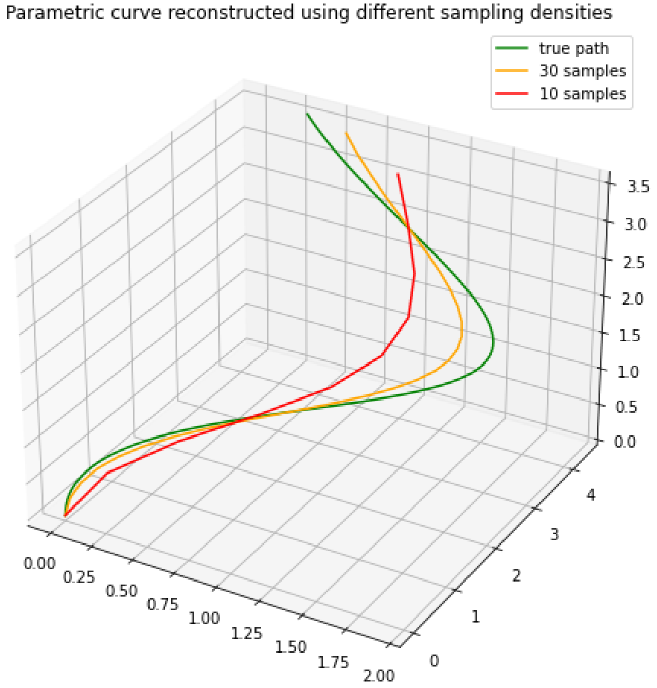

FIGURE 5.7. – *Numerical example showing the effect of reduced sampling density on the shape reconstruction of a parametric curve.*

ODISI™ series as most appropriate for extended-range and dynamic FOSS applications. Specifically, the 6000 series can simultaneously monitor up to 8 individual channels (which would correspond to individual cores) over 100 m with stand-off cables up to 50 m. This interrogator detects Rayleigh scattering and operates using OFDR, which provides an acceptable compromise between spatial resolutions and sensing range compared to other methods. The performance of an OFDR interrogator for FOSS in the range of 20 m was demonstrated by [20] using a LUNA interrogator. In this application, the shape sensor is a proprietary technology of LUNA and not commercially available. Another contending interrogator technology for FOSS, which is yet to be demonstrated in literature, is Pulse-Pre-Pump Brillouin Optical Time Domain Analysis (PPP-BOTDA), specifically through the Neubroscope instrument series by Neubrex [21]. This instrument benefits of sensing lengths up to 500 m, making a compromise on the measurand spatial resolution maxing out at 2 cm and temporal resolution at a few seconds. However, it is currently only available for single-channel measurements, which implies that either multiple interrogators must be used to interrogate a single shape sensor or that the multiple cores must consist of a single-looped fibre which severely hinders sensing length.

5.4.2. GEOMETRY

The geometry of a shape-sensing unit does not affect the shape-sensing ability of the system, as long as the geometric parameters are known. Specifically, if certain geometries are advantageous due to embedding requirements, it is possible to create a sensor with a non-circular cross-section, as shown in Figure 5.8. An example of a recommended geometry is a triangular cross-section sensor, as it provides additional control over core locations and twist during deployment. Regardless of the cross-section geometry and number of sensing cores, certain factors must be investigated prior to the production of the sensor, including : 1) the inclusion of a central core for mitigating elongation, compression and external stimuli effects; 2) the distance of the radial cores from the neutral plane and the expected sensitivity of the sensor; 3) the inclusion of helically wound cores for detecting twist in free-floating sensors.

ADVANTAGES OF INCLUDING A CENTRAL CORE

The distribution of the optical cores is important to the performance and ability of a shape sensor. As motioned above, the minimum number of cores required to enable shape-sensing is 3. However, increasing the number of cores improves the accuracy of the shape reconstruction process as the apparent curvature is derived from the averaged contribution of each core (equation 5.6), thereby minimizing the effect of instrument noise or environmental effects. Typically, the shape-sensing cores are distributed radially symmetrically around the geometrical center of the sensor, which allows simplified computation of the shape-sensing variables and ensures even directional sensitivity. An additional core can be added to the center of the configuration on the neutral axis. This core does not contribute to shape reconstruction but it is instead able to record any strain which does not originate from bending. As we have seen in Section 5.4.1, Rayleigh photon scattering is sensitive to strain as well as temperature. This means that local temperature variations will be spuriously converted to a strain response by the interrogator if not accounted for. Similarly, strain caused by effects other than bending such as point pressure, vibrations, elongation, and compression of the sensor will be present in the data and may be challenging to identify and isolate. The central core being insusceptible to strain due to bending

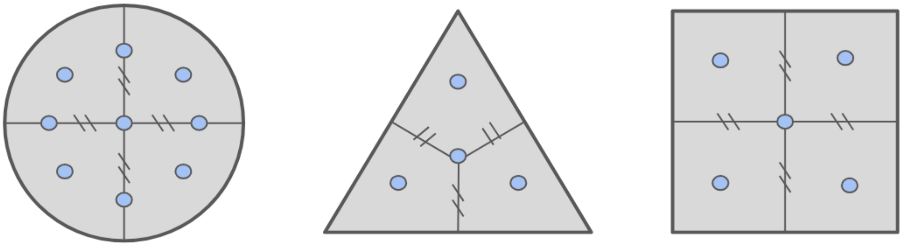

FIGURE 5.8. – *Examples of FO shape sensor geometries with variable numbers of cores and a central core design.*

will instead record all strain due to unwanted stimuli and can be used to process the strain data to abstract purely strain due to bending. An example of the strain recorded by all cores in a sensor undergoing elongation and the resultant shape-sensing after processing the strain data using central core strains is shown in Figure 5.9.

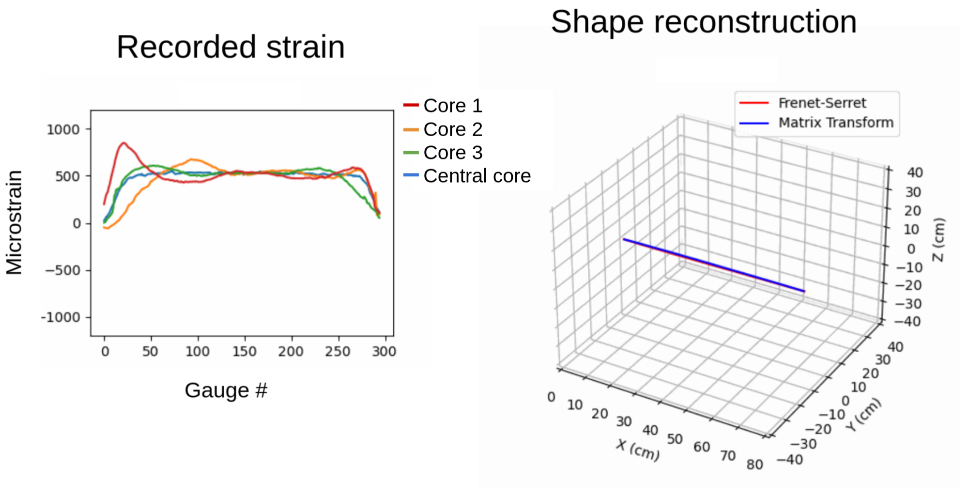

FIGURE 5.9. – *On the left, the strain measured for a shape sensor being elongated while being in a straight position. On the right, the reconstructed shape of the sensor after negating the strain recorded by the central core from the radial cores.*

HELICALLY WOUND RADIAL CORES FOR TWIST DETECTION

One variable that cannot be detected by the radial cores or a central core under the previously discussed configuration is twisting. This aspect is particularly relevant in highly dynamic environments, as twisting that is not accounted for will cause the path reconstruction to be built in the wrong direction. It is possible to mitigate twisting altogether by deploying the sensor in a manner where twist is prevented (see Section 5.4.3) [7]. However, free-floating flexible instruments like those used in the medical field cannot be prevented from twisting while employed. A method that is becoming common place in these FO shape sensors is to embed the radial cores in a helically wound manner [8], [22]-[24]. With this implementation, it is possible to detect twist if all radial cores are experiencing a common strain factor which is not present in the central core data. We can imagine a spring with a clockwise winding : if the end of the spring is twisted in the clockwise direction, the material will experience positive strain (similar to elongation); on the other hand, if the end of the spring is twisted in the counterclockwise direction, the material will experience negative strain (similar to compression). According to the workflow of [24], pure shear strain γ due to twist is given by

$$\gamma = r\frac{d\omega}{ds}, \tag{5.20}$$

where ω is the angle of twist and r, again, is the distance of a radial core from the center of the sensor. Since γ is proportional to r, we can again expect the central core to not experience strain due to twist. It is important to note that the twist angle ω should not be confused with the geometrical torsion of a path τ we have seen earlier. The distance between two measurements Δs can be described as a circular helix :

$$\Delta s = \sqrt{h^2 + r^2\omega^2}, \tag{5.21}$$

where h is the vertical distance between two measurements. We can use this expression to evaluate the longitudinal strain of a radial core due to twisting, referring back to Equation 5.1 :

$$\varepsilon_{twist} = \frac{\Delta L}{L} = \frac{\Delta s - h}{h} = \frac{\sqrt{h^2 + r^2\omega^2} - h}{h}. \tag{5.22}$$

When dealing with a FOSS sensor recording strain due to bending, twist and other factors, we can describe the isolated strain component due to twisting from the overall strain recorded by radial cores as

$$\varepsilon_{twist} = \frac{\sum_{i=1}^{n} \varepsilon_i^{radial}}{n} - \varepsilon_{central}. \tag{5.23}$$

Combining Equations 5.22 and 5.23, we can derive an expression which allows us to evaluate the angle of twist ω for a given measurement as

$$\omega = \sqrt{\frac{h^2\varepsilon_{twist} + 2h^2\varepsilon_{twist}}{r^2}}. \tag{5.24}$$

This value can then be used as an additional directional input in the shape-reconstruction methods by adjusting the angle of bending $\theta_{b+twist}$ such that

$$\theta_{b+twist} = \theta_b - \omega. \tag{5.25}$$

It is important to note that the production of a sensor with helically wound fibres of a constant period is a non-trivial problem, making this method less accessible than simply preventing the sensor from mechanically twisting.

CORE DISTANCE FROM THE NEUTRAL PLANE

As described in section 5.2 and specifically in Figure 5.3, the neutral plane runs through the centre of mass of the sensor and experiences zero strain due to bending. The distance of a core from the neutral plane dictates the amplitude of strain it will experience as the sensor deforms as a uniform unit. As we have seen in Equation 5.1, the strain is positively proportional to d, implying that we can increase sensitivity to a large radius of bending by placing the cores further away from the neutral plane. This would be advantageous to detect small shape variations over large distances. However, it is important to note the material strength of the fibreglass cores that deform in the elastic domain at strain levels lower than 0.2%, which is around 2000 $\mu\varepsilon$ [25]. High strains over short periods of time are acceptable but prolonged periods of high strain may cause permanent plastic deformation of the sensor and even tensile failure and fracture of the cores. Therefore, it is important to consider the expected magnitude of bending when deciding how to radially distribute the shape-sensing cores in a sensor.

5.4.3. EMBEDDING INTO OTHER STRUCTURES

Embedding the sensor into a structure or instrument to be monitored also requires special attention. There are different options available, each with benefits and draw-backs, which should be considered based on the application of the FOSS sensor.

1. **The sensor is bonded to a structure :** This case can only be used for a structure with large expected radius of bending or short distance between radial cores. This is because the absolute strain experienced

by an individual core will be proportional to the distance from the geometrical center of the entire structure and sensor as they deform as a combined unit. Moreover, it should be taken into account the amount of stretching that is expected from the structure as it will contribute to the total strain experienced by each core.

2. **The sensor is inserted through a dedicated channel :** It is possible to create a dedicated channel for the FOSS sensor which itself is bonded to a structure to be monitored. With correct lubrication, this method can help mitigate strain due to stretching of the structure, allowing for the sensor to be partially decoupled from the structure.
3. **The sensor is free-floating :** It is preferable that a free-floating sensor be deployed in a liquid or gel-like medium. This allows for slower rates of deformations and reduced environmental vibrations due to friction. For increased stability of the sensor, it can be advantageous to select a cladding material with a relatively high shore-A hardness (above 50A).

Other advantages can arise from a cladding or embedding method. A flexible, pressure-insensitive casing was demonstrated, allowing the mitigation of hydrostatic or environmental pressure noise[26]. The selection of an embedding method is entirely dependent on the condition of deployment and purpose of the sensor.

5.4.4. ORIENTING A SHAPE IN A GLOBAL 3D FRAME

Even with the best possible shape reconstruction, it is crucial to be able to correctly orient the path in space and put it in the context of a known local frame. To this end, three criteria must be satisfied :

1. **Sensor geometry :** The radial location of the cores used to derive the path variables like the curvature modulus κ or direction of bending θ_b must agree with the orientation of the cores as the sensor is deployed on the structure to be monitored.
2. **Location :** The location in 3D space must be known for the origin of the sensor.
3. **Orientation :** The orientation at origin must be known. Thinking back to the TNB frames discussed in Section 5.2.2, the normal and binormal vectors of the origin of the sensor are dictated by the geometry of the cores, given that the orientation of the beginning of the sensor does not rotate. However, the original tangent vector ($\vec{T}_0$) must be used to align the path to its correct direction. This effect is shown in Figure 5.10

where the same parametric curve is plotted with two different tangential orientations, leading to highly varied locations at the end of the sensor.

Depending on the deployment of the sensor, fulfilling these criteria may be as trivial as setting the origin to $\vec{r}_0 = [0,0,0]$ and the first tangent vector to $\vec{T}_0 = [1,0,0]$ or as complex as using a GPS/RTK measurements combined with INS to track the evolving location and orientation of the sensor. FOSS would therefore not be a stand-alone method but rather, be a technology that fits within existing positioning methods deployed in geophysical and geotechnical applications.

5.5. OUTLOOK TO GEOTECHNICAL AND GEOPHYSICAL APPLICATIONS OF FOSS

The material costs for manufacturing a multi-core optical fibre are negligible; however, creating a FOSS sensor to the specifications necessary for geophysical and geotechnical applications increases the costs considerably. For example, manufacturing an extended-range sensor with short radial core distance and hellically wound cores will be severely more costly than a similar range sensor with wider radial core distribution and a design preventing twist. We estimate that economies of scales would reduce these costs as they are adopted into the industry standard. The interrogators present the highest expenditure; however, due to the plug-and-play nature of FOs, a single interrogator could serve multiple permanently embedded FOSS sensors.

Today, the sensing ranges are limiting the application of FOSS to 100 m. However, there are strategies that could be employed to help improve shape-sensing results despite poorly sampled strain measurements over extreme distances. Notably, these methods are yet to be explicitly demonstrated :

- **Mixed positioning systems :** Using discrete positioning systems like satellite coordinate measurements (i.e, GPS/RTK) combined with INS measurements along the shape sensor can help support and correct the shape-sensing results over extended distances. These instruments are common practice in geophysical and geotechnical applications and regularly used conjointly. Combining multiple positioning methods is common practice to ensure high measurement accuracy in the field.
- **Temporally continuous strain measurements :** Rather than taking instantaneous strain measurements, taking multiple continuous measurements over a realistic and relevant time frame (based on the expected rate of deformation or shooting rate) can help mitigate instrument error as well as environmental factors if raw strains are averaged.

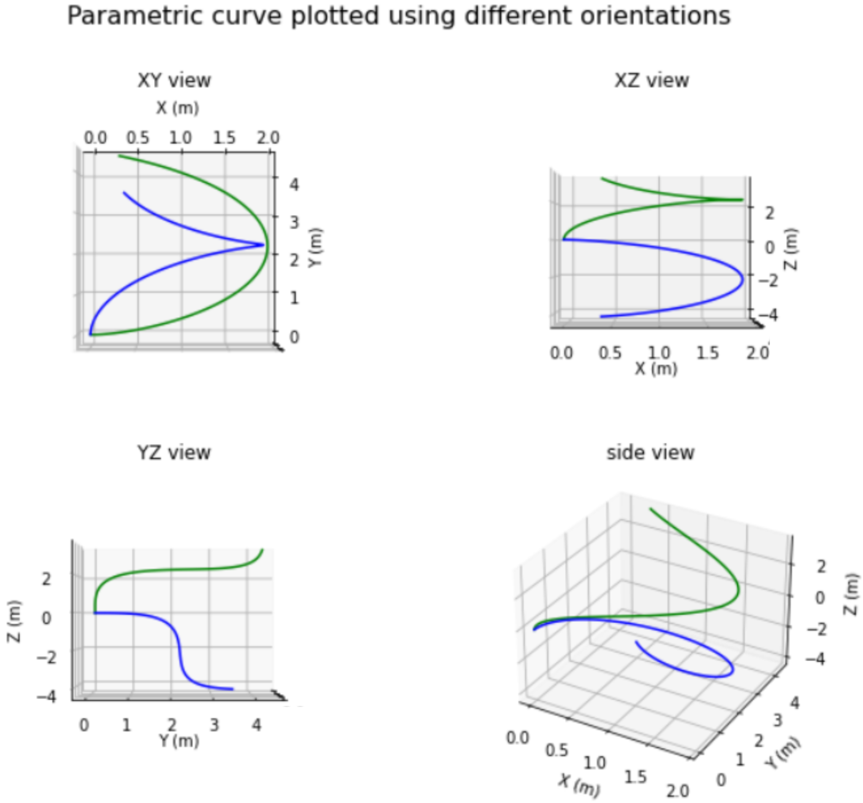

FIGURE 5.10. – *Example of a parametric helix plotted using different tangential orientations at the origin. Blue curve is plotted with* $\vec{T}_0 = [0,1,0]$ *and green curve with* $\vec{T}_0 = [1,1,1]$.

Considering the continuous nature of deformation in time, multiple measurements can also be helpful to develop rigorous time-dependent strain interpolation schemes for noisy data. Finally, if mixed positioning systems are used, multiple shape reconstructions can be performed from several continuous strain measurements, and, by comparing the accuracy of the shape reconstruction against other positioning systems, a 'best-fit' solution can be selected.

— **Shape-sensing error envelope :** Although the shape-reconstruction method is prone to spatial accumulation of the error, that is not the case for the sensitivity and accuracy of the strain measurements throughout each optical core. It is thus possible to accurately reconstruct the path of a sensor starting at any gauge and building the shape in any direction.

However, the shape reconstruction must be contextualized in the global geographical frame which, again, must be done using additional instrumental inputs like satellite positioning or INS measurements. Interestingly, as the shape reconstruction can be applied in both forwards and backwards directions, it would be possible to create an envelope of shape-reconstruction error with higher uncertainty near the center of the reconstructed segment.

- **Staggered gauge layout and interpolation schemes :** Since the strain recorded by individual cores is inevitably correlated as the sensor deforms as a uniform system, we could imagine a staggered gauge layout accompanied by an interrelated interpolation scheme enabling more reliable interpolation. This option would be specifically viable to sensors with more than four shape-sensing cores.

5.6. CONCLUSIONS

In this chapter we outlined the theory and practical requirements for applying FOSS to extended sensing lengths and dynamic environments. We demonstrated how distributed strain from multi-core fibres can be converted into curvature, bending direction and torsion to reconstruct 3D fibre trajectories using frameworks such as the Frenet–Serret frames or matrix transforms. We then identified some key practical factors affecting reconstruction accuracy, including, the interrogator performance, the gauge density, the taring and conditioning procedures, and the fibre geometry. Design considerations such as central-core strain referencing, radial core spacing, and twist sensitivity were discussed to be particularly important in dynamic settings. Although current interrogator limits constrain practical sensing lengths, several strategies—such as hybrid positioning, directional averaging, and tailored gauge layouts—can extend the usable range for geophysical and geotechnical applications.

As the diversity in fibre optic sensing technologies continues to gain traction and the development of fibre optic extended-range instruments allows for more accessible and higher performance, we believe that FOSS will become an attractive solution to shape-sensing problems in geotechnical and geophysical applications. Linking back to the practical issues during UHR surveys, FOSS could be an attractive low-profile sensor to include in the small diameter UHR streamer to continuously (both spatially and temporally) monitor their shape during acquisition in 3D.

5.7. ACKNOWLEDGMENTS

For this section of my thesis, we would like to thank all the contributors that have provided thought provoking discussions to develop the ideas that accumulated to this guide to start developing Long-Distance FOSS. Firstly, Marinus van der Hoek from van der Hoek Photonics as well as Manos Pefkos from Deltares and J. Andres Chavarria from LUNA Innovations.

RÉFÉRENCES

[1] A. HARTOG, *An introduction to distributed optical fibre sensors*. CRC Press, Taylor amp; Francis Group, 2018.

[2] I. FLORIS, J. ADAM, P. CALDERÓN et S. SALES, « Fiber Optic Shape Sensors : A comprehensive review », *Optics and Lasers in Engineering*, t. 139, avr. 2021. DOI : 10.1016/j.optlaseng.2020.106508.

[3] K. TAWEESINTANANON, M. LANDRØ, J. K. BRENNE et A. HAUKANES, « Distributed acoustic sensing for near-surface imaging using submarine telecommunication cable : A case study in the Trondheimsfjord, Norway », *GEOPHYSICS*, t. 86, n° 5, B303-B320, 2021. DOI : 10.1190/geo2020-0834.1. eprint : https://doi.org/10.1190/geo2020-0834.1. adresse : https://doi.org/10.1190/geo2020-0834.1.

[4] B. G. GORSHKOV, K. YÜKSEL, A. A. FOTIADI, M. WUILPART, D. A. KOROBKO, A. A. ZHIRNOV, K. V. STEPANOV, A. T. TUROV, Y. A. KONSTANTINOV et I. A. LOBACH, « Scientific Applications of Distributed Acoustic Sensing : State-of-the-Art Review and Perspective », *Sensors (Basel, Switzerland)*, t. 22, 2022.

[5] C. M. MONSBERGER et W. LIENHART, « Design, Testing, and Realization of a Distributed Fiber Optic Monitoring System to Assess Bending Characteristics Along Grouted Anchors », *Journal of Lightwave Technology*, t. 37, n° 18, p. 4603-4609, 2019. DOI : 10.1109/JLT.2019.2913907.

[6] C. XIAOMIN, W. MINGJUN et Y. XINHUA, « Deformation sensing of colonoscope on FBG sensor net », *TELKOMNIKA : Indonesian Journal of Electrical Engineering*, t. 10, déc. 2012. DOI : 10.11591/telkomnika.v10i8.1693.

[7] O. AL-AHMAD, M. OURAK, J. VAN ROOSBROECK, J. VLEKKEN et E. V. POORTEN, « Improved FBG-Based Shape Sensing Methods for Vascular Catheterization Treatment », *IEEE Robotics and Automation Letters*, t. 5, n° 3, p. 4687-4694, 2020. DOI : 10.1109/LRA.2020.3003291.

[8] F. KHAN, A. DENASI, D. BARRERA, J. MADRIGAL, S. SALES et S. MISRA, « Multi-Core Optical Fibers With Bragg Gratings as Shape Sensor for Flexible Medical Instruments », *IEEE Sensors Journal*, t. 19, n° 14, p. 5878-5884, 2019. DOI : 10.1109/JSEN.2019.2905010.

[9] C. M. MONSBERGER et W. LIENHART, « Distributed Fiber Optic Shape Sensing of Concrete Structures », *Sensors*, t. 21, n^o 18, 2021, ISSN : 1424-8220. DOI : 10.3390/s21186098. adresse : https://www.mdpi.com/1424-8220/21/18/6098.

[10] OFS, *Shape Sensing Solutions, Twisted Multicore Fiber with Continuous Grating*, English, OFS, 2020, 2 p.

[11] P. WESTBROOK, K. FEDER, T. KREMP, W. KO, H. WU, E. MONBERG, D. SIMOFF, K. BRADLEY et R. ORTIZ, « Distributed sensing over meter lengths using twisted multicore optical fiber with continuous bragg gratings », *Furukawa Review*, p. 26-32, mars 2017.

[12] E. M. LALLY, M. REAVES, E. HORRELL, S. KLUTE et M. E. FROGGATT, « Fiber optic shape sensing for monitoring of flexible structures », in *Sensors and Smart Structures Technologies for Civil, Mechanical, and Aerospace Systems 2012*, M. TOMIZUKA, C.-B. YUN et J. P. LYNCH, éd., International Society for Optics et Photonics, t. 8345, SPIE, 2012, 83452Y. DOI : 10.1117/12.917490. adresse : https://doi.org/10.1117/12.917490.

[13] C. XU et S. KHODAEI Zahra, « Shape Sensing with Rayleigh Backscattering Fibre Optic Sensor », *Sensors*, t. 20, n^o 14, p. 4040, 2020. DOI : https://doi.org/10.3390/s20144040.

[14] J. LANGER et D. A. SINGER, « Lagrangian Aspects of the Kirchhoff Elastic Rod », *SIAM Review*, t. 38, n^o 4, p. 605-618, 1996. DOI : 10.1137/S0036144593253290. eprint : https://doi.org/10.1137/S0036144593253290. adresse : https://doi.org/10.1137/S0036144593253290.

[15] J. MOORE et M. ROGGE, « Shape sensing using multi-core fiber optic cable and parametric curve solutions », *Optics express*, t. 20, p. 2967-73, jan. 2012. DOI : 10.1364/OE.20.002967.

[16] I. G. BAXTER, « A differential capacitance manometer », *Journal of Scientific Instruments*, t. 30, n^o 10, p. 358, oct. 1953. DOI : 10.1088/0950-7671/30/10/304. adresse : https://dx.doi.org/10.1088/0950-7671/30/10/304.

[17] D. PALOSCHI, K. A. BRONNIKOV, S. KORGANBAYEV, A. A. WOLF, A. DOSTOVALOV et P. SACCOMANDI, « 3D Shape Sensing With Multicore Optical Fibers : Transformation Matrices Versus Frenet-Serret Equations for Real-Time Application », *IEEE Sensors Journal*, t. 21, n^o 4, p. 4599-4609, 2021. DOI : 10.1109/JSEN.2020.3032480.

[18] D. PALOSCHI, K. A. BRONNIKOV, S. KORGANBAYEV, A. A. WOLF, A. DOSTOVALOV et P. SACCOMANDI, « 3D Shape Sensing With Multicore Optical Fibers : Transformation Matrices Versus Frenet-Serret Equations for Real-Time Application », *IEEE Sensors Journal*, t. 21, n^o 4, p. 4599-4609, 2021. DOI : 10.1109/JSEN.2020.3032480.

[19] A. GÜEMES, « Fiber Optics Strain Sensors », *NATO-STO Lecture Series (STO-EN-AVT-220)*, t. 16, 2014.

[20] E. M. Lally, M. Reaves, E. Horrell, S. Klute et M. E. Froggatt, « Fiber optic shape sensing for monitoring of flexible structures », in *Sensors and Smart Structures Technologies for Civil, Mechanical, and Aerospace Systems 2012*, M. Tomizuka, C.-B. Yun et J. P. Lynch, éd., International Society for Optics et Photonics, t. 8345, SPIE, 2012, 83452Y. doi : 10.1117/12.917490. adresse : https://doi.org/10.1117/12.917490.

[21] Neubrex, *Neural Optical Fiber Scope, Neubroscope NBX-7031*, Brochure, 2019. adresse : https://www.neubrex.com/pdf/NBX_7031.pdf.

[22] Y. Liu, A. Zhou et L. Yuan, « Multifunctional fiber-optic sensor, based on helix structure and fiber Bragg gratings, for shape sensing », *Optics Laser Technology*, t. 143, p. 107 327, 2021, issn : 0030-3992. doi : https://doi.org/10.1016/j.optlastec.2021.107327. adresse : https://www.sciencedirect.com/science/article/pii/S0030399221004151.

[23] Y. Zhao, J.-c. Shen, Q. Liu et C.-l. Zhu, « Optical fiber sensor based on helical Fibers : A review », *Measurement*, t. 188, p. 110 400, 2022, issn : 0263-2241. doi : https://doi.org/10.1016/j.measurement.2021.110400. adresse : https://www.sciencedirect.com/science/article/pii/S0263224121012902.

[24] I. Floris, J. Madrigal, S. Sales, P. A. Calderón et J. M. Adam, « Twisting measurement and compensation of optical shape sensor based on spun multicore fiber », *Mechanical Systems and Signal Processing*, t. 140, 106700, p. 106 700, juin 2020. doi : 10.1016/j.ymssp.2020.106700.

[25] A. Piccolo, S. Delepine-Lesoille, E. Friedrich, S. Aziri, Y. Lecieux et D. Leduc, « Mechanical Properties of Optical Fiber Strain Sensing Cables under -Ray Irradiation and Large Strain Influence », *Sensors*, t. 20, n$^{\text{o}}$ 3, p. 696, 2020. doi : 10.3390/s20030696. adresse : https://doi.org/10.3390/s20030696.

[26] H. Godaba, I. Vitanov, F. Aljaber, A. Ataka et K. Althoefer, « A bending sensor insensitive to pressure : soft proprioception based on abraded optical fibres », in *2020 3rd IEEE International Conference on Soft Robotics (RoboSoft)*, 2020, p. 104-109. doi : 10.1109/RoboSoft48309.2020.9115984.

6

FOSS FOR STREAMER-SHAPE TRACKING: PROXY SENSOR MANUFACTURING AND FLUME EXPERIMENTS

To expand on the concept of using FOSS for UHR streamer-shape tracking, we develop a sensor and perform proof-of-concept experiments in a controlled environment.
For the development of the sensor, numerical modelling of core-position uncertainties and laboratory tests under pressure, temperature, and mechanical loading establish the sensor's robustness and key limitations.
In a flume, we demonstrate that the sensor allows to reconstruct streamer deflection and estimate hydrophone positions with sufficient accuracy to support receiver-side deghosting.

6.1. INTRODUCTION

In Chapter 5, we presented FOSS methods and proposed to use this technology to support existing positioning systems for UHR streamers. Specifically, this low-profile solution that continuously monitors the shape of a streamer in real-time and in 3D would be a useful addition to the existing UHR acquistion systems that were discussed in Chapter 4. Based on the research on FOSS theory and sensor design presented in Chapter 5.2, we developed a proxy sensor to deploy in proof-of-concept bench and flume experiments. Namely, key features that are considered include : a suitable interrogator with short gauge length and suitable sensing lengths and temporal resolutions; relatively large distance of the radial cores to the neutral plane to increase sensitivity to large bending radii and the inclusion of a central core to measure and suppress environmental strain not due to bending. In this chapter, we focus on the performance of the sensor as a new method of hydrophone positioning in UHR streamers through bench and flume experiments and the outlook of FOSS technology for this application. A conceptual overview of the FOSS method we propose is given in Figure 6.1

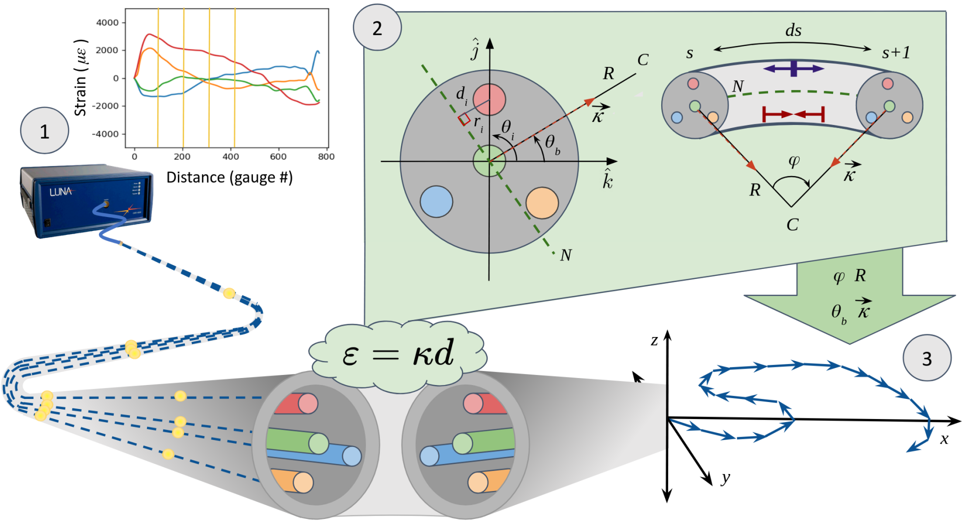

FIGURE 6.1. – *Overview of the FOSS method we propose. 1) The quasi-simultaneous measurement of strains (ε) in a sensor containing four optical cores (red, yellow blue, and green); 2) The derivation of path variables from strain values using sensor geometry at each measurement point. Path variables include : curvature vector $\vec{\kappa}$ with modulus κ and direction θ_b also called the angle of bending, radius of bending R, and angle of rotation φ. Geometry variables include distance d_i from a neutral plane N, the radial distance of the core r_i to the centre of the sensor, the angular distance of the core to the arbitrary z-axis θ_i, and distance between consecutive measurements ds. 3) The iterative reconstruction of the sensor path in 3D using path variables and numerical methods.*

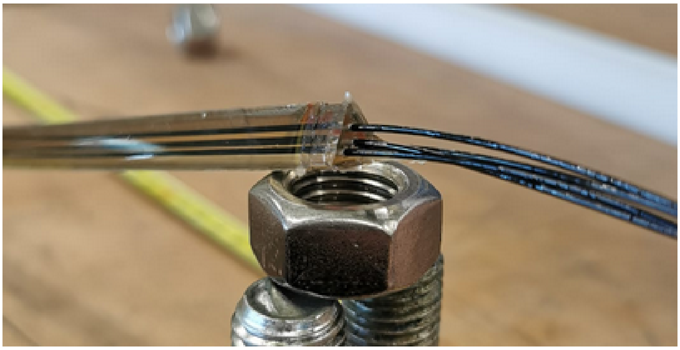

FIGURE 6.2. – *Close-up of the end-phase of the sensor cladding showing the triangular cross-section and the four individual cores including the central core and three radial cores.*

6.2. SSU2000 FEATURES AND DEPLOYMENT

The Shape-Sensing Unit 2000mm (SSU2000) was developed as a proof-of-concept sensor to test the viability of FOSS in dynamic settings for streamer shape-sensing. The sensor is designed to perform with the LUNA ODISI 610x series [1], which is a multichannel, high-sensitivity ($\pm 1\mu\varepsilon$) Optical Frequency Domain Reflectometry interrogator that handles sensing lengths of up to 100 m with measurement sampling of 2.6 mm.

The SSU2000 is designed with a triangular cross-section containing a central core and 3 evenly radially distributed outer cores. The triangular design serves two purposes : firstly, during deployment, there is exact knowledge of the core orientation at the first gauge; and secondly, the taring measurements can be easily performed with certainty that the sensor is free of twist. A diagram of the sensor's set-up and close-up of the sensor's end-phase exhibiting this geometry is shown in Figure 6.2. The distance of the radial cores to the neutral axis of 2±0.2 mm allows for sensitivity to bending radii up to 2000 m according to Equation 5.2. Large bending radii are significant in the context of small curvatures, which can be expected from a streamer being pulled by a vessel. The raw fibres are coated with a black polyurethane which provides a strong bond to the triangular cladding, allowing the sensor to deform as a uniform unit and free of internal friction. Modelling of the SSU2000 was performed in COMSOL, an example of the pre-production COMSOL modelling of the sensor geometry under twisting strain is shown in Figure 6.3. A representative diagram of the complete sensor is shown in Figure 6.4.

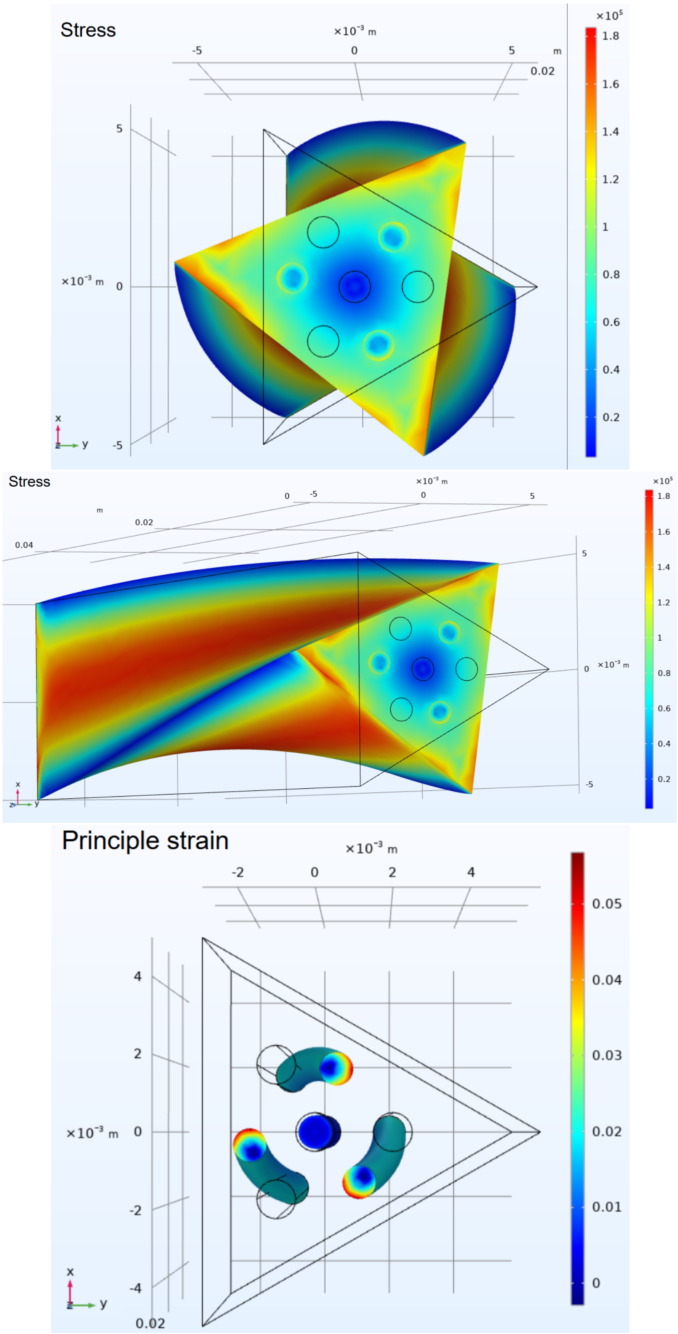

FIGURE 6.3. – *COMSOL model of the SSU2000 under twisting strain showing the stress field (top and middle) and the principle strain field on the cores (bottom)*

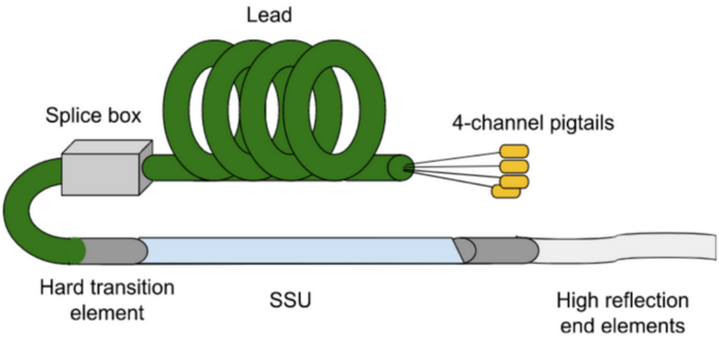

FIGURE 6.4. – *Schematic diagram of the SSU2000 and deployment features where each pigtail is associated with a sensing FO core.*

To evaluate the influence of radial core positioning uncertainties on shape-sensing accuracy, we develop a numerical model, in which, core positions are perturbed randomly and smoothly by up to 10% along the sensor length. An example of this modelling approach is illustrated in Figure 6.5, with a total of 25,000 random drift scenarios simulated. And the modelling algorithm is given in 1. The distribution of the resulting shape-sensing errors is presented in Figure 6.6. Due to the manufacture methods of the proxy sensor, it is not possible to detect the exact core deviations from the intended positions in the SSU-2000, however, this is something that can be controlled in commercial manufacturing. Based on the modelling performed, the maximum drift caused by core placement deviations is approximately 1.5 cm over the 2 m sensor length; we consider the associated error acceptable for the intended flume experiments.

We carry out an experimental validation through a series of bench tests assessing the SSU2000's performance under different external stimuli. The hydrostatic pressure tests, are conducted by immersing the sensor vertically in water to a depth of 1 m and indicate no measurable strain response attributable to pressure. Strain artifacts induced by point loading or elongation are effectively mitigated by the presence of a central core, provided that strain is distributed uniformly across all cores. Temperature experiments demonstrate that the interrogation method is sensitive to gradients as small as 0.1°C. In contrast, torsional effects can not be compensated due to the straight fibre arrangement, highlighting the importance of the embedding sleeve for such corrections. Finally, acoustic wave experiments—designed to replicate Distributed Acoustic Sensing (DAS) conditions—show that with a 3 Hz inter-

Algorithm 1 Stochastic 10% core positioning error simulations algorithm

```
Require: Strain matrix $\varepsilon$, gauge spacing $dx$, core radius $r_{in}$
Ensure: Reconstructed sensor paths with randomly generated core-position error
  Nominal Strain-State and Nominal Shape Computation
  for $i = 1$ to $n_s$ do
      Update angular positions of the three cores
      Construct core location matrix $M$
      Compute pseudo-inverse $M^+$
      Compute $\alpha = M^+\varepsilon_i$
      Compute bending direction $\theta_i$
      Compute curvature magnitude $K_i$
  end for
  Compute torsion $\tau = \nabla|\theta|$
  Compute radius of curvature $R = 1/K$
  Compute twist increment $\phi = ds/R$
  Define initial Frenet frame vectors $T_0$ and $N_0$
  Reconstruct curve using Frenet–Serret integration
  Reconstruct curve using matrix transformation method
  Store nominal paths

  Stochastic Error Analysis
  for $it = 0$ to $it = 30$ do
      for $m = 1$ to $n_s - 1$ do
          Generate $m$ random checkpoints for each core
          Perturb between $0 - 10\%$
          Interpolate checkpoints to create continuous error paths
          for $i = 1$ to $n_s$ do
              Update perturbed core angles and radii
              Construct perturbed location matrix $M$
              Compute pseudo-inverse $M^+$
              Compute $\alpha = M^+\varepsilon_i$
              Compute $\theta_i$ and $K_i$
          end for
          Compute $\tau$, $R$, and $\phi$
          Reconstruct shape using Frenet–Serret method
          Reconstruct shape using matrix transformation method
          Store reconstructed paths
      end for
  end for
```

rogation rate, acoustic wavefields are not detectable in the recorded strain data.

To secure the SSU2000 to a UHR streamer, we design a custom rubber sleeve to allow the sensor to shift longitudinally while preventing twisting. The sleeve consists of two separate elements-a base that can be laced around the streamer and a channel that can house the sensor. The sleeve is made from rubber and is lubricated using vegetable oil during deployment. Circular elements are attached to the interior of the sleeve channel to prevent the sensor from twisting internally during deployment. The sleeve system and fit of the sensor in the channel are shown in Figure 6.7.

6.3. FLUME EXPERIMENTS DESIGN

The goal of the flume experiments is to show that the shape-sensing result using the SSU2000 and its embedding sleeve are capable of detecting the deflection of a streamer in water, in order to improve the quality of the seismic data by correctly estimating the location of the hydrophones. For this purpose, UHR seismic data is collected with a streamer in various states of bending while collecting strain data simultaneously to track the shape of the streamer. By acquiring seismic data with the streamer deployed in a straight configuration near the water surface, we establish a reference dataset that can be used to correct for distortions in the bent-streamer measurements. This approach enables us to recover reflections from the base of the flume and to validate the bent-streamer results against the straight-streamer reference. For additional control and validation, the streamer in only deflected in the vertical plane, simulating hydrophone depths variations and not feathering. This allows for additional manual measurements of the streamer depths along various points. For the SSU-2000 shape reconstruction, no constrains are placed to limit reconstructed bending in the vertical plane, thus a true 3D-bending estimation is still created for these controlled 2D streamer configurations.

The streamer contains 12 hydrophones with a spacing of 30 cm and is sensitive to frequencies up to 5 kHz. The source is a 3-8 kHz transducer that is pointed towards the concrete flooring of the flume. The flume is filled with water to a height of 1.3 m and the streamer is fully submerged for the measurements. A conceptual diagram of the experiment design is shown in Figure 6.8. Due to the shape of the flume and the directionality of the source, we aim to avoid detecting reflections from the side walls.

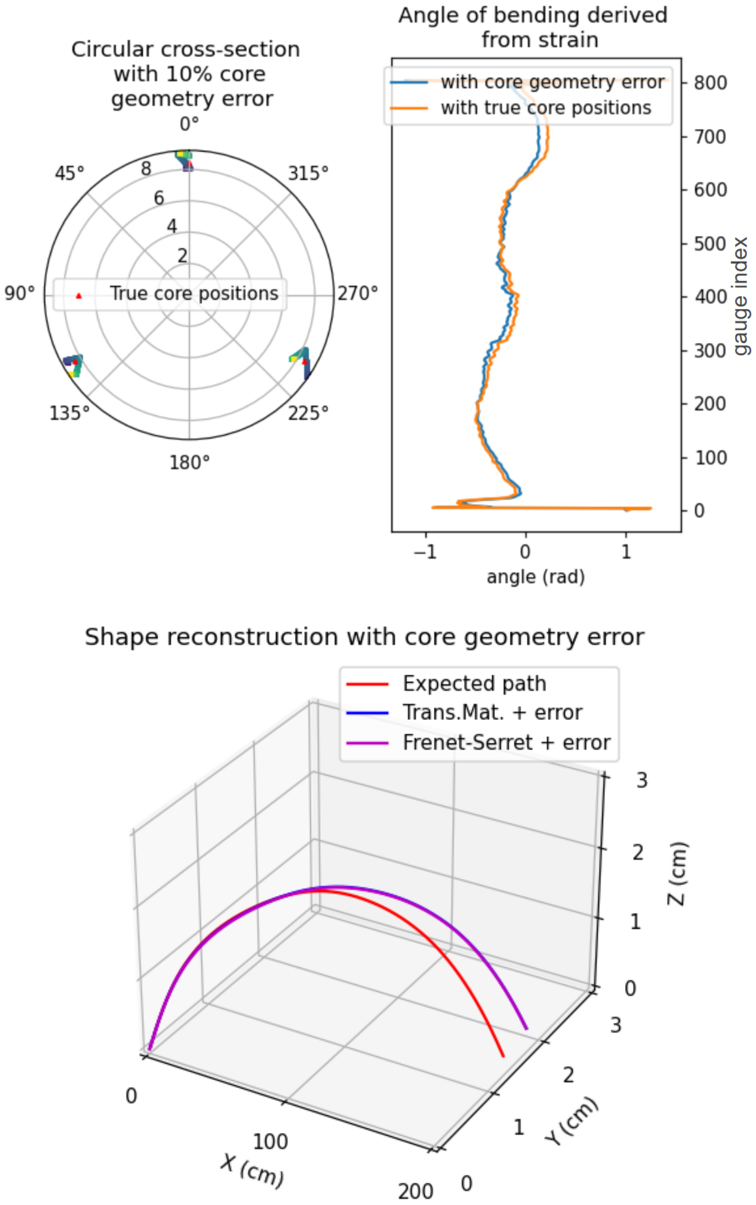

FIGURE 6.5. – *Example of an iteration of the effect of core position drift up to 10%. The top figure shows the angular plot of the core positions drift (left) and the resulting angle of bending values with true core positions and with drift throughout the sensor (right). The bottom figure shows the shape-sensing results using core position drift using Frenet-Serret and Transformation Matrix methods. As the results are near-identical the Transformation Matrix path is partially hidden under the Frenet-Serret path.*

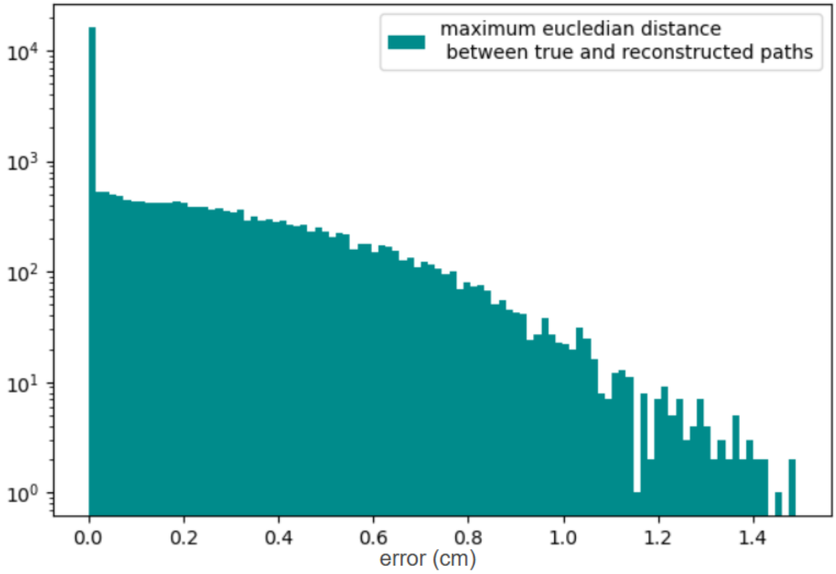

FIGURE 6.6. – *Log-scaled histogram of the maximum Euclidean distance error in shape reconstruction due to core geometry drift up to 10% per core for 24,000 randomly generated examples.*

The LUNA 6104 interrogator [1] is operated at a measurement rate of 3.125 Hz per channel with a gauge pitch of 2.6 mm. The taring measurement of the sensor is performed by placing the streamer and sensor configuration on a straight steel rod while in the flume, as shown in Figure 6.9.

6.4. DATA PROCESSING

We process the raw strain data from the LUNA interrogator using basic signal-processing techniques. We isolate the correct SSU gauges and align them using information from the splice box (shown in Figure 6.4). The signal from each core is interpolated where necessary and high-frequency noise from the interrogator is filtered out. We substract the strain response from the central core to remove non-bending strains from the radial cores signal and reconstruct the sensor path for each time step. this removal is done as a simple subtraction of the strains recorded by the central core from the strains recorded at the radial cores, accounting for possible tugging and acoustic artifacts in the signal. The sensor path is aligned using the known orientation of the beginning of the sensor which is attached to the stationary arm as well as the known core geometry orientation inside the dedicated sleeve.

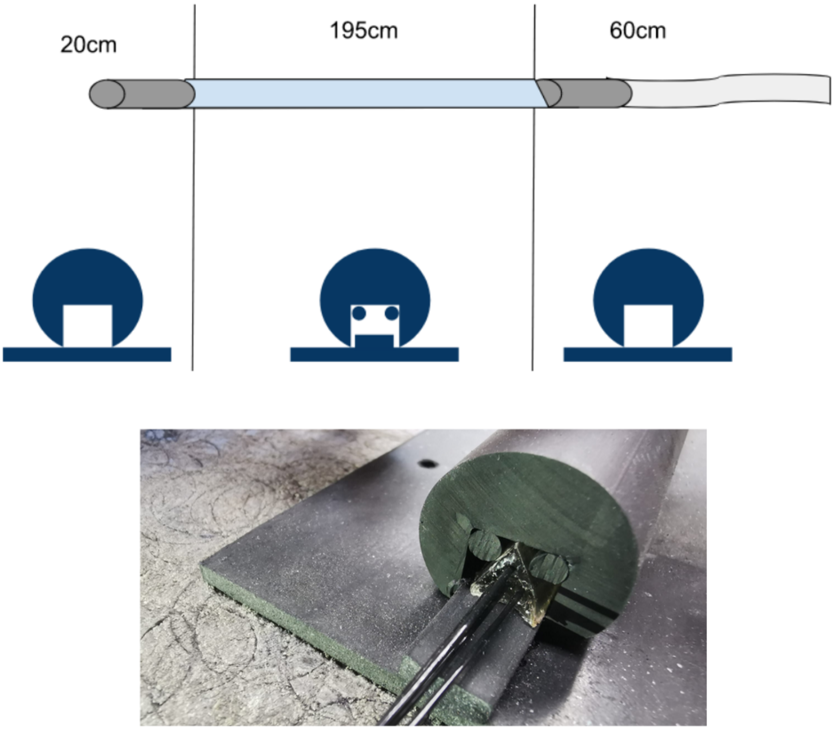

FIGURE 6.7. – *Top : a diagram showing the cross-section of the sleeve along the sensor, consisting of the sleeve base and channel. Bottom : a picture showing the fit of the sensor in the sleeve, allowing sliding but preventing twisting.*

We filter the UHR seismic data to remove frequencies above 5000 Hz that are assumed to be high-frequency streamer noise and 3 repeated shots of the streamer with the same configuration are stacked to improve SNR. The location of the SSU2000 on the streamer is measured to be able to correctly extrapolate the hydrophone depths from the reconstructed shape.

6.5. RESULTS

6.5.1. SHAPE SENSING

The results of the shape-sensing procedure are presented in Figure 6.10, demonstrating that the SSU2000 sensor in its embedding sleeve successfully reconstructed the streamer's shape. The shape is reconstructed iteratively using the matrix transform methods. This reconstruction is validated by

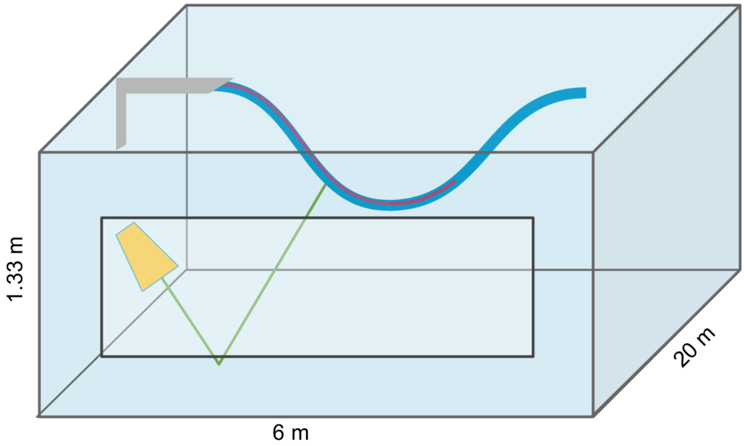

FIGURE 6.8. – *Conceptual diagram of the seismic acquisition layout with the streamer (blue line) and embedded SSU2000 (purple line) attached at one end to a stationary arm. The transducer (yellow box) emits a highly directional pulse (green line) which is directed towards the bottom of the flume.*

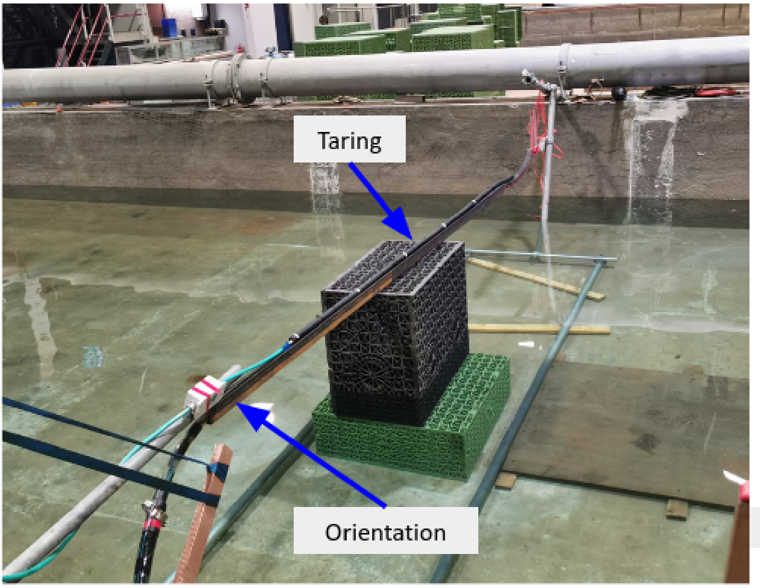

FIGURE 6.9. – *Method of taring the SSU2000 while deployed on the streamer.*

comparing it to the depth measurements recorded during the experiment. However, as lateral deflection was not tracked in this example, the accuracy of the observed lateral deflection at the end of the sensor cannot be assessed. The true lateral displacement of the streamer was not tracked due to the limited methods available for validation. The experiment with the strongest bending (smallest bending radius), shown in Figure 6.11, reveal a case where the shape-sensing procedure failed, as indicated by the significant deviation in the XY view. Upon reviewing the strain data, we hypothesize that the excessive bending caused a circular element within the embedding sleeve to press against the side of the SSU2000. This likely results in point pressure that unevenly affects the cores, disrupting the strain ratios between the radial cores.

From valid shape-sensing results, the actual positions of the hydrophones along the streamer can be derived through careful measurements of the geometry of the experiment set-up given that the SSU2000 is bound to the exterior of the streamer. Using the actual hydrophone positions, we can attempt to improve the frequency response of the data using the ghost operator.

6.5.2. RECEIVER-SIDE DEGHOSTING

As previously discussed, marine seismic data acquisition is fundamentally influenced by the presence of the free surface, which acts as a near-perfect reflector. This boundary condition generates receiver ghost notches that manifest as periodic amplitude cancellations in the spectrum (Chapter 4). In the flume experiments, the vertical deviation of the hydrophones is sufficient to induce receiver ghosts in the data based on the frequency range of the source of 1000-5000Hz. The theoretical notches for a hydrophone at various depths are shown in Figure 6.12.

As described in Chapter 4, the deghosted version of the primary $P(\omega)$ with receiver depth z_r can be retrieved using equation 4.4 where $G(\omega) = 1 - e^{-i\omega\tau}$, and $\tau = \frac{2z_r}{c}$ is the estimated ghost time delay; $G^*(\omega)$ is its complex conjugate, and ϵ is a stabilisation factor [2], [3]. In practice, $\epsilon = 0.01 * max(power)$ is proportional to a small fraction of the maximum spectral power and $c = 1500$ m/s was assumed for the entire flume. Before deghosting, we precondition the traces using a tapered Tukey window with a taper ratio of 0.2 to reduce spectral leakage and minimize edge effects during the Fourier transform. After deghosting, we apply a bandpass filter again between 1000-5000 Hz to the obtained signals. The result from the deghosting procedure is shown in Figure 6.13. The deghosted amplitude spectrum of the stacked traces shows

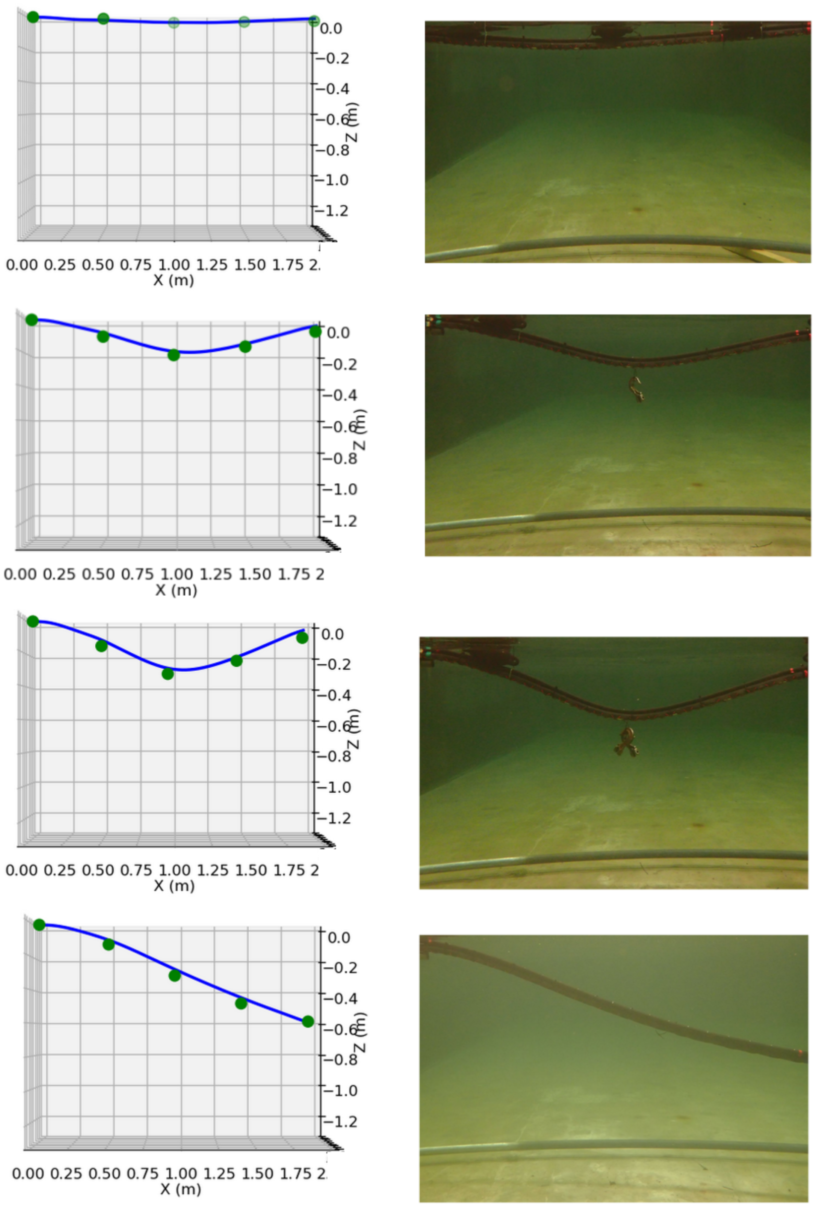

FIGURE 6.10. – *Reconstructed streamer shape from SSU2000 strain data and shape-sensing methods (blue line) and depth measurements taken along the sensor during acquisition (green dots) for verification compared to photographs of the streamer in the water for each shape.*

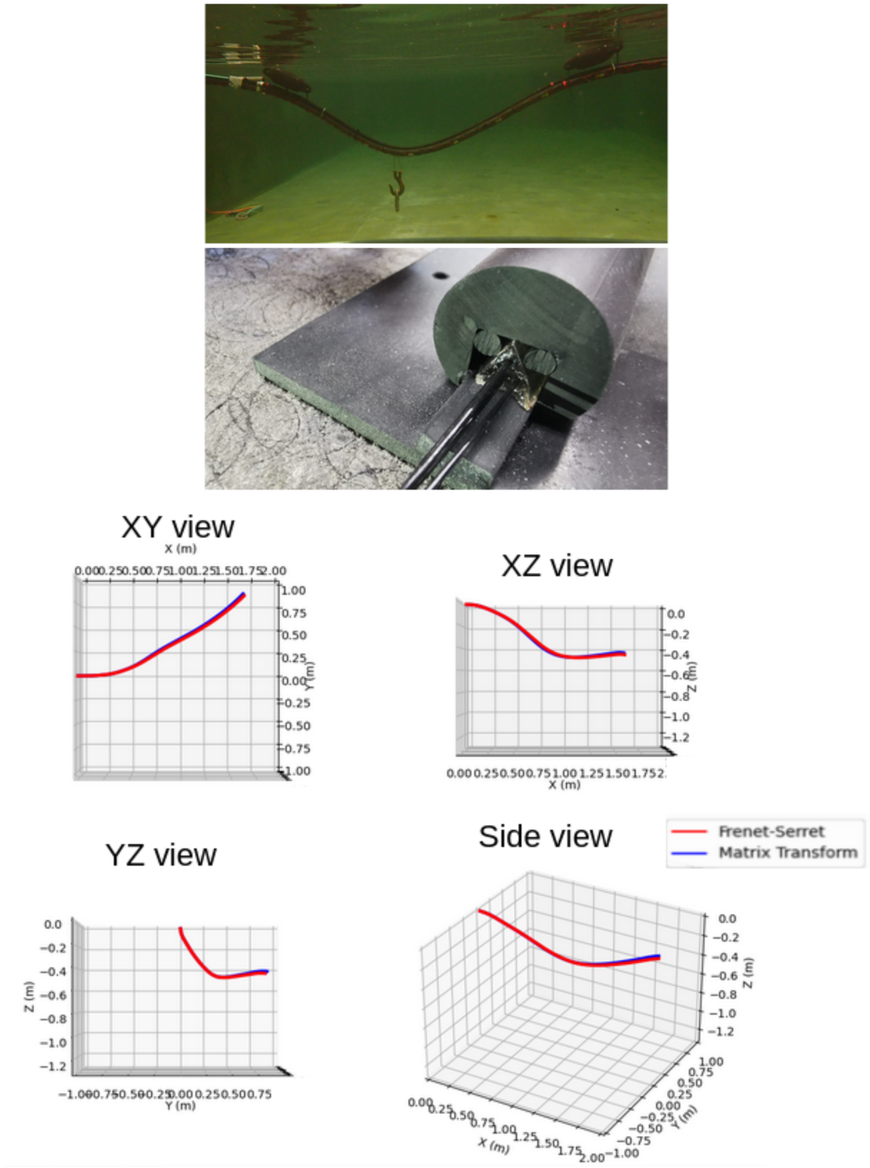

Figure 6.11. – *Example of a shape-sensing reconstruction with unexpected deviation in the Y-direction. Streamer in the flume showing (top) and the fit of the SSU2000 in the embedding sleeve allowing sliding but preventing twisting (middle). Reconstructed shape using Frenet-Serret and transformation matrix methods from different angles (bottom).*

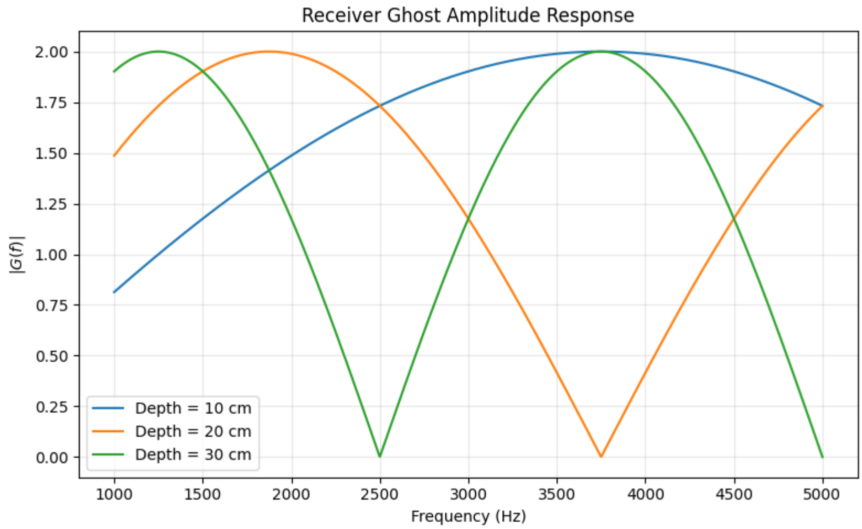

FIGURE 6.12. – *Frequency notching due to variable receiver depths for a signal in the frequency band of 1000-5000 Hz.*

improved amplitudes where the notches around 3500 and 4000 Hz are present in the original (raw) stacked data.

6.6. DISCUSSION

The flume experiments carried out using the SSU2000 prototype show promising results for FOSS in a controlled environment to estimate the location of hydrophones in UHR streamers during acquisition; they also allow to more easily filter ghosts in the data. Yet, failures of the embedding sleeve observed underscore the work to be done to reach a prototype that may be tested in the field. Ideally, the shape sensor should be embedded within the streamer, in a flexible, frictionless, non-collapsible conduit, allowing it to deform due to bending and elongation. Some streamer models are produced in sections that are later assembled, for these systems, one should imaging that the sensor would be attached to the exterior of the streamer after assembly if it cannot be integrated within. Additionally, the inclusion of helically wound fibre cores to monitor sensor twisting, would remove the need to prevent the sensor from twisting and minimize the occurrence of pinch points for short bending radii.

Deployment in the field would also require a longer shape sensor. Although

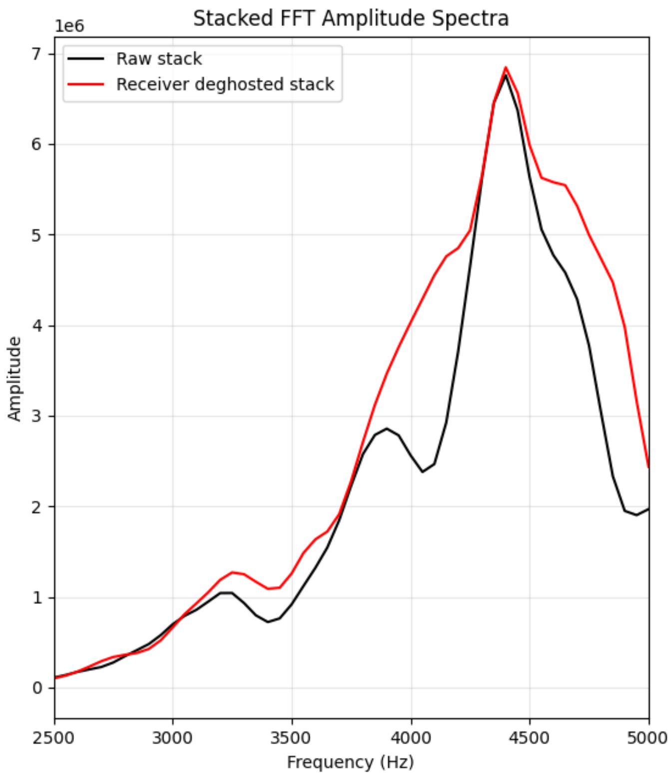

FIGURE 6.13. – *Spectra of stacked traces before and after the deghosting procedure using hydrophone depths derived from the SSU2000 shape sensor.*

the interrogator technologies discussed above can monitor lengths up to 100 m, an obvious vulnerability of FOSS is that errors in the shape reconstruction will accumulate spatially along the reconstructed path. With the shape sensing validation method employed in these experiments, quantifying the exact shape reconstruction error from the true path is limited. More experiments should be carried out using FOSS on a streamer that contains conventional positioning equipment to compare the reconstructed hydrophone locations or validate using another established shape sensing method like visual shape sensing.

Despite these limitations, an initial attempt was made to assess how shape-sensing errors might accumulate over 100 m by studying the effect of increasing gauge length on reconstructed paths. Figures 6.16 and 6.15 illustrate this by downsampling the measured strains to various effective sampling

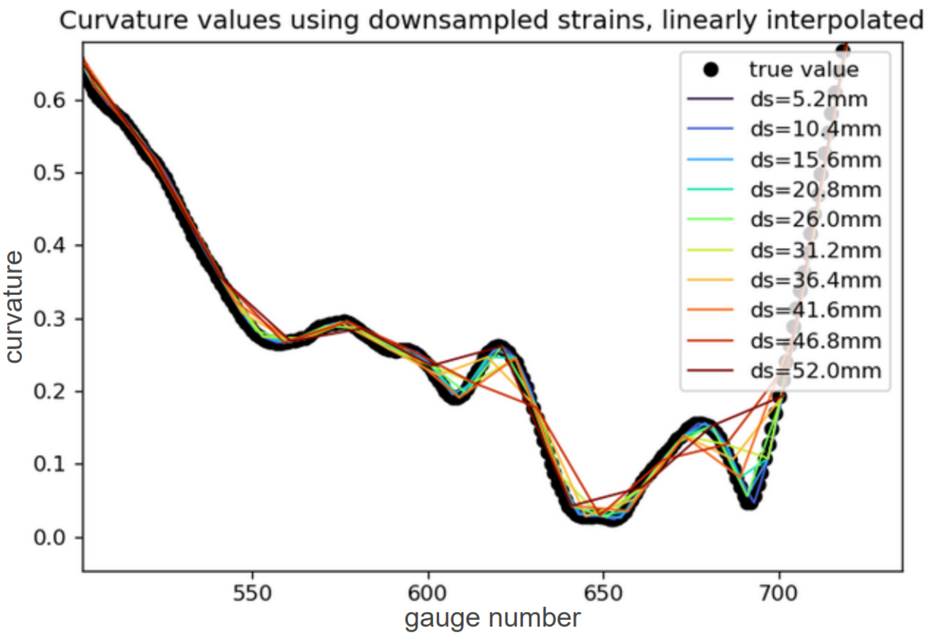

FIGURE 6.14. – *Effects of gauge length on reconstructed shape. The true values are derived from the gauge length of 2.6 mm as used for the bench and flume experiments. The figure shows the derived curvature values using decreasing strain sampling frequencies.*

distances and re-interpolating them to the original 2.6 mm resolution used in the flume experiments. For this analysis, the reconstructed path using the original 2.6 mm gauge length is used as the true path. The top panels in both figures present the reconstructed shapes, while the bottom panels show the corresponding maximum Euclidean distance error relative to the true path. As expected, reducing the strain sampling density removes small-scale curvature information, inducing a forced shape reconstruction error. Interestingly, the matrix-transform method, despite outperforming Frenet–Serret in the controlled flume tests, shows a stronger sensitivity to downsampling. This is notable given that both methods depend on the same derived strain quantities, such as curvature. Keeping the gauge subsampling to 5.2 mm and extrapolating the error reconstruction to 100 m produces a shape reconstruction error of ≈30 cm for the matrix transform method and ≈1.7cm for the Frenet-Serret method due to continuous strain subsampling alone. This analysis shows that for rates bending radii tested in the experiments, the gauge length of 2.6 mm should

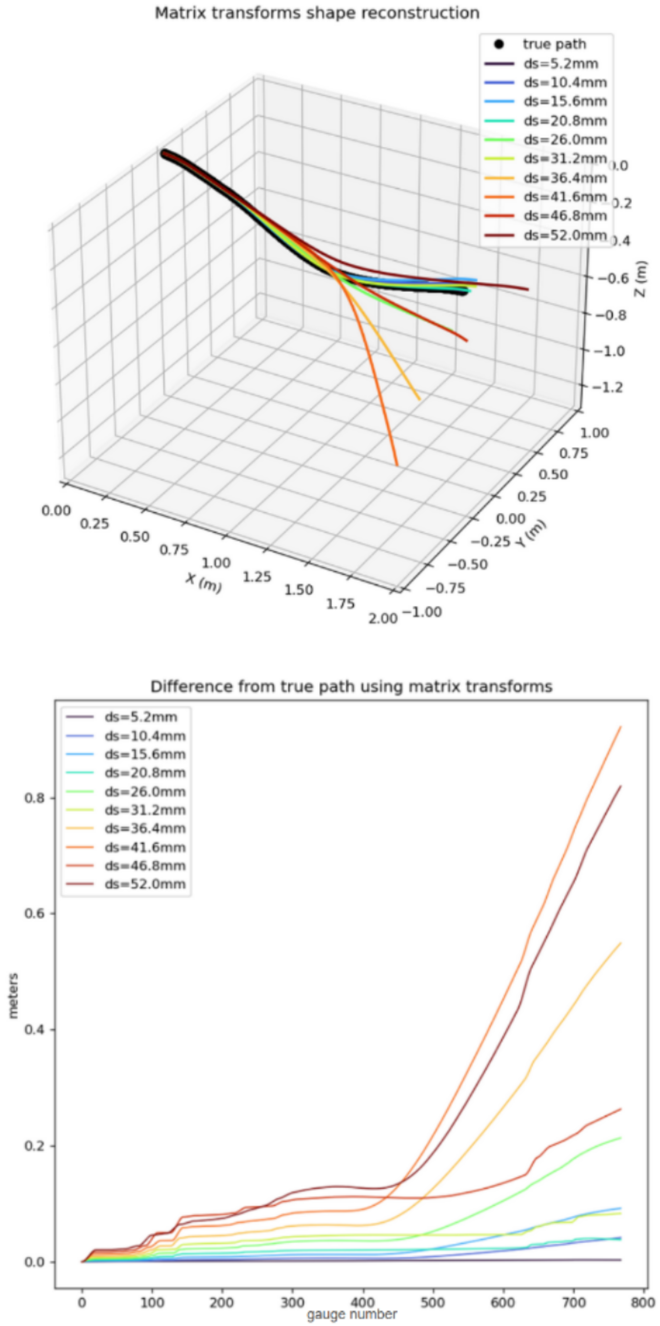

FIGURE 6.15. – *Effects of gauge length on reconstructed shape using the Matrix-Transform method.*

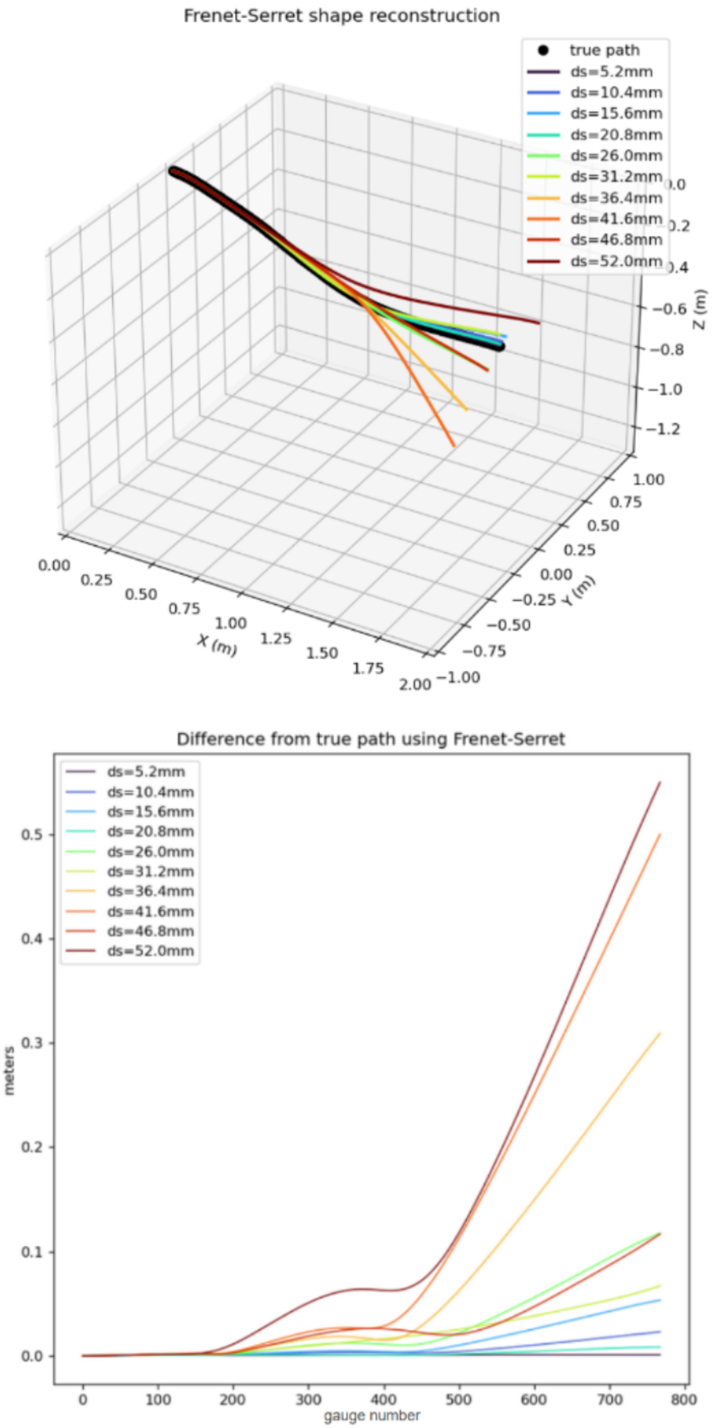

FIGURE 6.16. – *Effects of gauge length on reconstructed shape using the Frenet-Serret method*

be sufficient to capture the streamer deformation.

This analysis neglects interrogator-related noise, such as phase noise, quantization noise, and SNR degradation with distance, all of which can introduce bias into curvature estimation. It also omits potential environmental disturbances like the potential pinching effects in the streamer seen in the flume experiments. Calibration uncertainties, such as errors in gauge-length definition, imperfect taring, imperfect core positioning and uncertain initial orientation, are also not modelled. As a result, the modelled drift observed for gauge lengths above 5 cm should be interpreted as a best-case lower bound, with real-world errors expected to be substantially larger. Several strategies could be employed to reduce possible spatially accumulated errors : 1. the shape can be reconstructed forwards (i.e., from the head buoy) and backwards (i.e., from the tail buoy), thereby creating an envelope of possible paths for the centre of the sensor; 2. the continuous recording of strains to obtain the average path over a sub-sampled number of time-steps, as the deformation of a streamer is expected to be small on a millisecond timescale. Using the forward-backward reconstruction can also be a useful tool to get a feel for the error induced by interrogator and sensor bias. Figure 6.17 shows the reconstruction error in terms of euclidean distance between a path reconstructed forwards and backwards using the Frenet-Serret and matrix transform methods. A much stronger consistency in forward v. backward shape reconstruction appears with the matrix transform method, which initially also provided a more accurate shape reconstruction of the streamer in the flume and therefore was used for the results in Figure 6.10. We therefore argue that the maximum error between the shape reconstruction using the Matrix Transform paths is more representative of the error that may be induced by sensor and interrogator bias. This error of 0.1 cm over the 2 m sensor could scale up to 5 cm over a 100 m distance. It is nonetheless difficult to generalise this analysis and extrapolate it to longer distances as it will be highly dependent on the quality in sensor construction, selection of fibre core materials and selection of the interrogator. Additionally, the optic signal may also degrade over longer distances in ways that cannot be observed over the 2 m sensing distance.

Another factor to consider for field applications is the taring procedure. DOFSs detect the differential strain to a base strain state that is recorded through the taring procedure. For FOSS, it is necessary to record the shape of the sensor during taring so that the shape computed can be reconstructed relative to the tare shape. In the flume experiments, this was simplified by taring the sensor in a straight configuration; however, in the field,

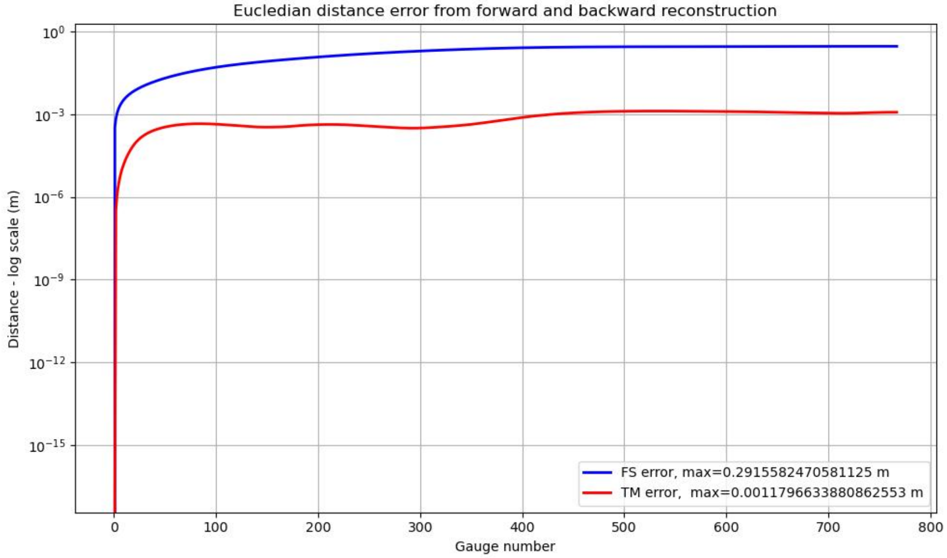

FIGURE 6.17. – *Euclidean distance between paths reconstructed using the FS and TM methods over a 2 m distance using normal gauge sampling 2.6mm.*

this procedure would be carried out while the streamer is wound before deployment. The orientation at the origin of the SSU2000 was also controlled in the experiment using a stationary arm. This is necessary to orient the reconstructed path in a shared global frame. In the field, a FOSS sensor on a streamer would require a gyroscopic instrument at the origin of reconstruction and a GPS. These are commonly present on the head and tail buoys of UHR seismic streamers.

Finally, higher shape-sensing precision is achieved when the radial fibre cores are placed farther from the central core, as larger core separation produces greater differential strain and therefore improves curvature resolution. However, increasing this radial offset also makes the fibre more susceptible to bending-induced strain. Cores positioned farther from the neutral axis experience higher tensile and compressive loads, reducing the minimum allowable bending radius before fibre damage or micro-bending occurs. For streamer operations, this imposes a practical constraint : the sensor must withstand the tight coil diameters used during deployment and storage. Thus, radial spacing must be balanced between sensing sensitivity and mechanical robustness. Any increase in sensing precision must not compromise the fibre's ability to survive repeated coiling during transport and handling.

6.6.1. RELATION TO DAS ACQUISITION

It would be advantageous if the FOSS sensor could also function as a DAS receiver, enabling simultaneous shape sensing and seismic measurements. Helically wound fibre cores—which improve twist sensitivity can also enhance DAS signal directional response when the same fibre is used to record seismic wavefields [4]. Interestingly, it was demonstrated that DAS can capture very low-frequency ambient seismic energy and extract stable surface-wave dispersion information for shear-wave velocity estimation [5], [6], highlighting the strong potential of DAS in the low-frequency regime rather than the high-frequency domain needed for UHR imaging. Perhaps, this shifts the perspective : instead of attempting to extend OFDR-based sensing to high frequencies—where the required long gauge lengths severely restrict usable bandwidth, the real opportunity may lie in using the same fibre for low-frequency measurements, such as background velocity updates, large-scale structural constraints, or low-frequency inputs to FWI. In this view, a combined FOSS–DAS fibre is not a replacement for UHR hydrophones but a complementary sensor that provides low-frequency information unavailable to standard streamer systems.

6.7. CONCLUSION

We demonstrated the feasibility of using FOSS as a complementary positioning method for UHR seismic streamers. A proof-of-concept FOSS sensor, the SSU2000, was designed, manufactured, and validated through a combination of numerical tests, controlled bench experiments, and flume-scale seismic acquisition. The modelling and laboratory results confirmed that the sensor geometry, bonding strategy, and central-core configuration provide sufficient robustness against temperature variations, pressure changes, and distributed loading for the intended application. The flume experiments showed that the SSU2000, when deployed in a custom embedding sleeve, can reliably reconstruct streamer deflection under moderate bending and provide hydrophone positions with accuracy adequate for receiver-side deghosting. Although extreme bending exposed limitations in the mechanical sleeve design, the successful cases demonstrated that shape-based hydrophone repositioning measurably improves the spectral content of the seismic/acoustic data. Overall, the results establish FOSS as a promising technology for enhancing receiver positioning in UHR marine acquisition. The work provides a proof-of-concept framework—from sensor design to seismic application—that can be extended toward longer sensors, improved embedding solutions, and integration with existing navigation systems in future field-scale implementations.

6.8. ACKNOWLEDGMENTS

This work would not have been realized without the collaboration and support from Manos Pefkos, Edvard Ahlrichs and Roeland Nieboer from Deltares as well as Marinus van der Hoek from van der Hoek Photonics. We would also like to thank Olivier Monrigual and Rick van der Kolk from GeoMarine and Willem Fontein from GEOxyz for their in-kind contributions and technical support in this project. Finally, we would like to thank Sakthivel Palani for his insights and discussions on the practical applications of LD-FOSS in other sectors.

RÉFÉRENCES

[1] LUNA-INC, *ODISI-6000 datasheet*, Brochure, 2022. adresse : https://lunainc.com/sites/default/files/assets/files/data-sheet/Luna%20ODiSI%206000%20Data%20Sheet.pdf.

[2] J.-W. VROLIJK et G. BLACQUIERE, « Shot-based deghosting for variable sea surface and receiver depth », p. 4887-4892, août 2017. DOI : 10.1190/segam2017-17742156.1.

[3] G. PROVENZANO, T. J. HENSTOCK, J. M. BULL *et al.*, « Attenuation of receiver ghosts in variable-depth streamer high-resolution seismic reflection data », *Marine Geophysical Research*, t. 41, p. 11, 2020. DOI : 10.1007/s11001-020-09407-9. adresse : https://doi.org/10.1007/s11001-020-09407-9.

[4] B. A. ADENIYI, A. H. ABDUL LATIFF, Z. O. ADEDEJI, A. R. MD ARSHAD et D. T. ASFHA, « Directional sensitivity of fibre optic cables for surface seismic reflection distributed acoustic sensing : a review and potential solutions for enhanced sensitivity », *Geomechanics and Geophysics for Geo-Energy and Geo-Resources*, t. 11, n^o 1, p. 60, 2025, ISSN : 2363-8427. DOI : 10.1007/s40948-025-00972-0. adresse : https://doi.org/10.1007/s40948-025-00972-0.

[5] K. TAWEESINTANANON, M. LANDRØ, J. K. BRENNE et A. HAUKANES, « Distributed acoustic sensing for near-surface imaging using submarine telecommunication cable : A case study in the Trondheimsfjord, Norway », *GEOPHYSICS*, t. 86, n^o 5, B303-B320, 2021. DOI : 10.1190/geo2020-0834.1. eprint : https://doi.org/10.1190/geo2020-0834.1. adresse : https://doi.org/10.1190/geo2020-0834.1.

[6] J. SHRAGGE, J. YANG, N. ISSA, M. ROELENS, M. DENTITH et S. SCHEDIWY, « Low-frequency ambient distributed acoustic sensing (DAS) : case study from Perth, Australia », *Geophysical Journal International*, t. 226, n^o 1, p. 564-581, mars 2021, ISSN : 0956-540X. DOI : 10.1093/gji/ggab111. eprint : https://academic.oup.com/gji/article-pdf/226/1/564/37882374/ggab111.pdf. adresse : https://doi.org/10.1093/gji/ggab111.

7

OUTLOOKS AND VALORISATION

Too often PhD research is stored on a bookshelf, never to be read again. How can the research presented in this thesis be of societal value beyond mere scientific curiosity?

Conclusions on the individual themes tackled in this thesis are included at the end of each relevant chapter. Specifically, the conclusions on the usefulness of JMI compared to FWI for offshore UHR data can be found in Chapter 3; the conclusions on implementing Long-Distance FOSS (LD-FOSS) from an instrumental and practical perspective can be found in Chapter 5; and, the conclusions on the proof-of-concept experiments using LD-FOSS can be found in Chapter 6. In this last chapter, we therefore focus on the general outlooks and valorisation of the methods and technologies discussed for future adoption in various industries.

7.1. OUTLOOKS ON JMI IN (ULTRA) HIGH-RESOLUTION MARINE SEISMICS

Despite its longstanding presence in the scientific literature, JMI has not yet achieved widespread industrial adoption. Several challenges, already addressed by alternative methodologies, have limited its practical deployment. Notably, the angle-independent reflectivity approximation and the handling of AVO effects remain unresolved within current JMI implementations [1]. However, the research presented in this thesis positions JMI as a practical approach for velocity model building in (U)HR marine seismic surveys.

Specifically, the primary angle-dependence and AVO pitfalls have a very limited effect on this type of data. JMI's limited reliance on legacy velocity information is also advantageous in offshore near-surface regions, where historical datasets may be sparse, incomplete, or entirely unavailable, as the near-surface is traditionally treated as a homogeneous layer. Furthermore, the dual imaging and inversion workflow aligns well with the UHR survey philosophy, emphasizing smaller, cost-efficient acquisition campaigns and rapid processing for timely investigation and monitoring. By contrast, traditional FWI would require substantial changes to acquisition strategies, including extended offsets to recover refracted and diving waves. In the constrained environment of a busy North Sea survey, this might necessitate independent source and streamer towing systems, dramatically increasing costs and potentially compromising the feasibility of UHR operations.

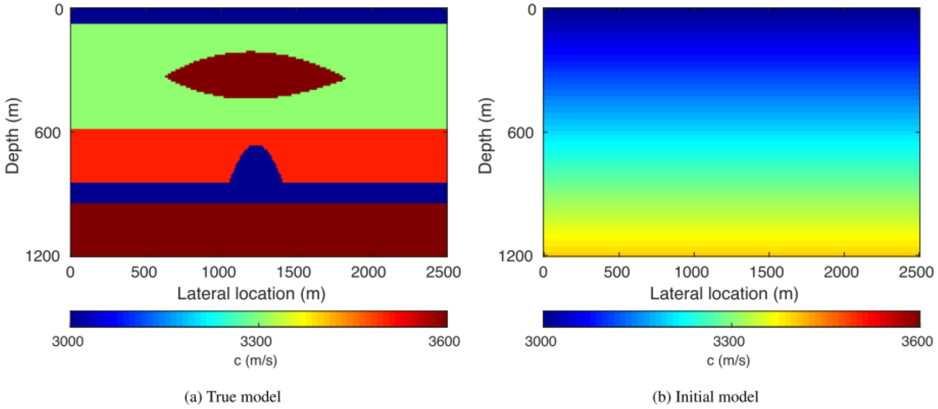

(a) True model

(b) Initial model

FIGURE 7.1. – *Figure from [2] showing the ground truth and starting models used to obtain the results in Figure 7.2*

A High-Resolution JMI was also presented by Abolhassani et. al. 2025 [2], which offers a significant improvement in the tomographic results achievable with JMI. In their paper, JMI is referred to as One-Way Reflection Waveform Inversion (ORWI) and HR-ORWI uses gradient pre-conditioning with the reciprocal of the Hessian matrix to retrieve sharper velocity estimates using less iterative steps, as shown in Figure 7.2 compared to the ground truth shown inf Figure 7.1. In the context of the tomographic results presented in Chapter 3, it is clear that HR-ORWI technology should become an essential component of JMI/ORWI for industry adoption of the method.

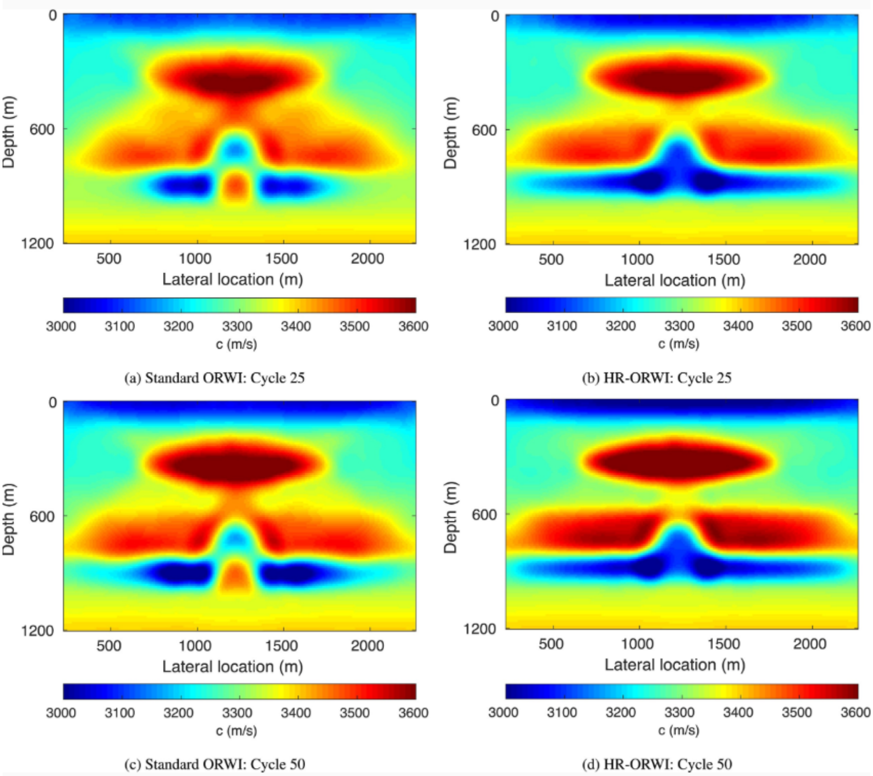

(a) Standard ORWI: Cycle 25

(b) HR-ORWI: Cycle 25

(c) Standard ORWI: Cycle 50

(d) HR-ORWI: Cycle 50

FIGURE 7.2. – *Figure from [2] where ORWI refers to the standard JMI process and HR-ORWI is the High-Resolution JMI.*

Even with HR-ORWI, successful velocity estimation of field data using JMI remains highly dependent on the presence of reflective layers within the entirety of the investigated depth and careful data pre-processing. Despite these limitations, and given the shortcomings of industry-standard methods that were demonstrated in this thesis, JMI may just be the best solution available for this problem.

7.2. OUTLOOKS OF LD-FOSS IN OTHER TECHNICAL APPLICATIONS

The outlook of the experiments presented in Chapters 5 and 6 goes further than UHR streamer shape-sensing. A successful implementation of Long-Distance FOSS (LD-FOSS) could have a significant impact on improving the performance of multiple sensors and instruments that require positioning precision in hard-to-reach environments. The advantage of FOSS would be its ability to track deformation and shapes in remote, hard-to-reach environments under dynamic conditions. With the plug-and-play nature of FO sensors, it is possible to permanently embed FOSS sensor into a structure and periodically interrogate it for monitoring. As interrogator technologies improve, the sensing lengths available for FOSS might increase, allowing for extended-range sensing past 100 m. Careful design choices must be implemented to ensure that a FOSS solution to a specific application would provide accurate, reliable, and repeatable measurements, especially as errors propagate with distances.

TOWED SENSOR ARRAYS

More than just UHR streamers, towed sonar and sensor arrays are a broadly used technology, particularly in naval defense, underwater surveillance, and ocean exploration. In defense, they are a key component of anti-submarine warfare, where they enable ships and submarines to detect, classify, and track quiet underwater targets such as enemy submarines or unmanned underwater vehicles while maintaining stealth, since passive arrays only listen rather than transmit. These arrays, often extending hundreds of meters behind a vessel, help isolate target signals from self-noise and improve directional resolution and detection range. Other applications also include environmental monitoring to map soundscapes or track marine mammals, and oceanographic research to measure temperature, salinity, and current profiles along long transects. In all these applications, accurate positioning and shape estimation of the towed array are essential to ensure that measured data can be correctly interpreted in spatial terms [3]-[5].

For target detection, for example, passive sonar does not emit a signal and a target is located using Bearing-Only Tracking (BOT). BOT heavily relies on knowing where the sensor elements are relative to the own-ship motion; otherwise, the filter updates (e.g., the Kalman or extended Kalman filter) will use incorrect geometry, degrade observability, introduce bias, and lead to poor convergence [6]. When a ship maneuvers, the towed array does not remain fixed behind it but swings, lags, or deforms under hydrodynamic drag and inertia, so a dynamic model of the cable-array is required to estimate the array-head position in real-time. Typical solutions include physics-based dynamic modelling (e.g., Newtonian mechanics of cable drag and tension), filter-based estimation (Kalman, extended Kalman, or particle/Bayesian filters), and joint estimation methods that simultaneously recover array shape or position and target bearings (e.g., sparse Bayesian learning, maximum-likelihood shape estimation, or data-driven approaches)

[7], [8]. An example of a physical-modelling approach to the cable deformation problem is shown in Figure 7.3. LD-FOSS would be a useful technology for towed-array cable tracking as the cable shape could be estimated using real-time field measurements to replace post-acquisition processing.

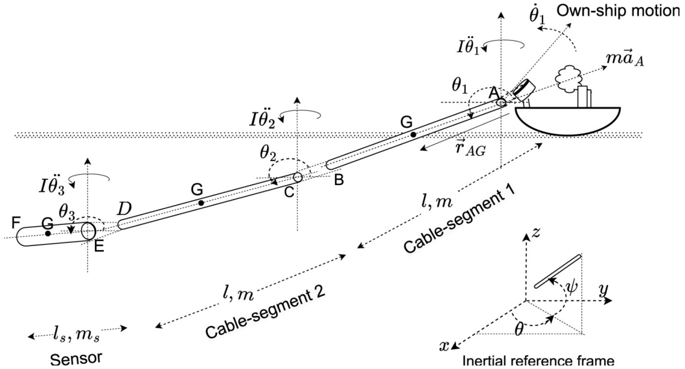

FIGURE 7.3. – *Physical model to estimate towed-array cable shape from Singh et al., 2025 [7].*

Similar to a marine streamer, a land streamer is a towed array of geophones (or fibre-optic sensors) used for acquiring seismic data efficiently over the land surface. Instead of deploying individual geophones manually, the sensors are mounted on a flexible cable or frame that can be dragged behind a vehicle. Modern land streamers may be equipped with gimbaled geophones or flexible frames, allowing operation over uneven or mildly hilly terrain. They have the advantage of being fast to deploy for near-surface reflection surveys, reducing survey costs and operational time [9], [10]. Introducing a LD-FOSS sensor in the land-streamer would support the application of this technology for rapid and flexible acquisition, where the topographical variations of the terrain could be measured for each shot for precise statics corrections without the need of multiple GPS measurements.

PIPELINES AND UTILITY MAPPING

An LD-FOSS sensor could also be of use to monitor the shape of pipelines, duct system and conduits to create 3D models of the infrastructure networks for maintenance purposes. In many refineries, for example, operators use outdated analog maps that do not reflect the 3D configuration of the pipelines to identify a pipe of interest for maintenance purposes. This is a time-consuming task that must be repeated every time maintenance is performed. With an LD-FOSS sensor, the refinery could create a 3D digital twin of its shape in relation to the surrounding pipes. With the inherent resilience of FO sensing methods, the pipes would not necessarily need to be drained and the refinery could stay operational during the mapping. This type of documentation update and 3D model creation is already being carried out at facilities using scanning methods, as shown in Figure 7.4. However, the scanning method does not differentiate between the pipes and the structural elements of the site. It can be imagined how adding an LD-FOSS survey to the scanning survey would quickly enable the integration of the pipeline architecture into the visual 3D survey.

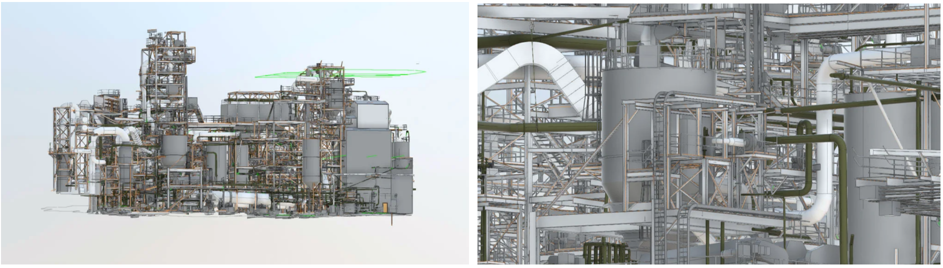

FIGURE 7.4. – *Example of 3D model for an oil refinery created using scanning methods. [11]*

This application could also be extended to mapping existing utilities and pipelines in cities and urban areas to enable target digging for maintenance projects. The underground utilities include communication cables, gas lines, sewer lines, water pipes and electrical lines, these may be existing but utility mapping is also carried out on new development to ensure a future-proof infrastructure development [12]. Utility mapping is generally carried out using variety of techniques including GPR, EM, acoustics, potholing and aerial inspection [13]. The current issue is that each of these methods has severe limitations, which prevents them from being carried out individually when 3D precision is required. An example of this is shown in Figure 7.5 where the ambiguity of GPR measurement for utility mapping can be clearly seen, as the infrastructure approaches the resolution limit of the wavelength. Moreover, the aforementioned measurement methods are limited to areas with exposed ground (limiting their resolution in built-up urban environments) and resolution deteriorates severely with depth. All of these factors can make locating and tracking the utility a time consuming process [14]. In this case, LD-FOSS might become an enabling technology to support endeavours for utility mapping, providing precise utility path reconstruction where other methods may fall short.

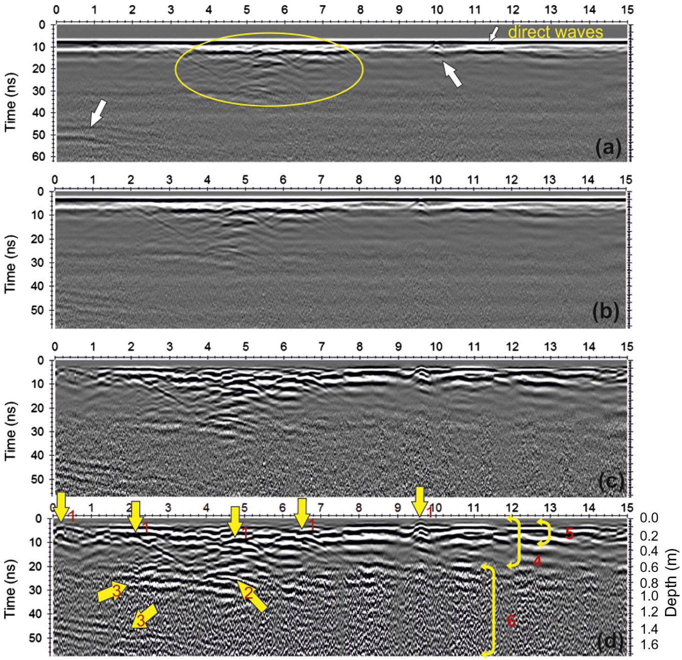

FIGURE 7.5. – *From [15] : "Example of the GPR data acquired along the asphalt road and the successive processing steps applied for the data. (a) Raw data, (b) after time shift, (c) after background removal, (d) after band-pass filter, Automatic Gain Control and depth estimation. Numbers indicate; (1) pipes, (2) deeper pipes, (3) interface, (4) shallow filling sediments, (5) asphaltic zone and (6) moisture filling sediments."*

HORIZONTAL DIRECTIONAL DRILLING AND OTHER WELL OPERATIONS

Horizontal Directional Drilling (HDD) is the process of drilling at shallow depths in the subsurface, first at an angle, then horizontally to reach a specific location in urban environments. This method is used to connect or replace underground utilities in urban areas or to circumvent natural features like rivers or lakes in more remote areas. The typical boring distances range from 10 m to about 2 km. In order to reach the target end-location, the drill head must be steered during operation to adjust its course. Currently, the drill head location is estimated through a series of surveys that measure inclination, azimuth, and tool face at appropriate intervals. These intervals may be small or large depending on the soil conditions and complexity of the target boring path. These surveys provide only discrete measurements of path variables and thus may lead to lower accuracy, specifically if a path deflection occurs between survey points due to a small inclusion in the soil like a rock or boulder. The technologies used for the surveys include gyroscopic measurements and magnetic surveys from the surface. In HDD for underground utilities, a "walkover" tracking system from the surface may be used but is quickly interrupted by the presence of infrastructure or lakes etc., which make standing over the drill impossible [16]. According to conference proceedings from the GEOconvention, 2021 [17] :

> "*Directional survey error and uncertainty can be reduced with mitigation methods. Still, it is entirely possible to be faced with errors in the range of 2-5 meters TVD* [True Vertical Depth] *and 10-20 meters azimuth when drilling a horizontal well of 1500 m length.*"

LD-FOSS could be used to measure the deformation of the drill cable to correctly model the precise location of the drill head in the subsurface.

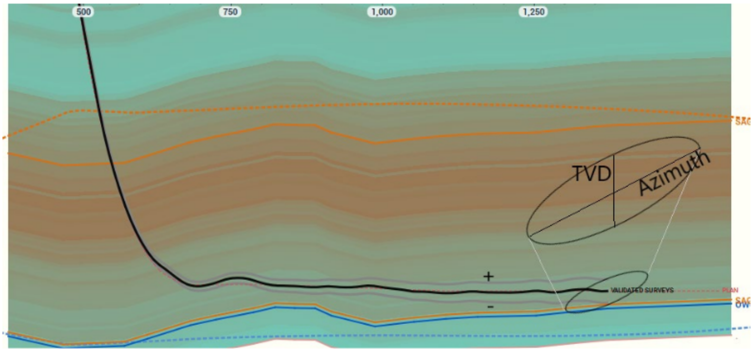

FIGURE 7.6. – *Example of drill head positioning uncertainty from [17].*

Additionally, specific drilling operations require accurate real-time drill head positioning. For example, well intersection technology used for deep wells are costly operations with specialized equipment where a higher trajectory accuracy could reduce operational costs and lead time in the field. Contrastingly, radial drilling is a low-cost technology to increase well productivity that require a fast and cheap way to define the drilling path trajectory whereby the accuracy is not key but the ability to locate the drill is. Using LD-FOSS during a “quiet” period, like when the casing is being introduced or the drill head path is being adjusted, a quasi-instantaneous shape measurement can be made without pulling the drill head out, saving in operational costs.

TETHERED UNMANNED VEHICLES

LD-FOSS could also be applied to the tracking and monitoring of tethered unmanned vehicles operating in hard-to-reach or otherwise constrained environments. Three illustrative examples highlight this potential :

1. Tethered space rovers represent a promising application. Ongoing research by NASA and ESA investigates the use of FOSS to monitor the position and configuration of rover tethers in real-time [18], as shown in Figure 7.7. This approach enables precise awareness of the tether geometry during planetary exploration missions—an essential capability for safe navigation on uneven terrain, especially when rovers are deployed cooperatively or explore caves and lava tubes.
2. Unmanned Underwater Vehicles (UUVs) could significantly benefit from the integration of LD-FOSS sensors within their communication tethers. These vehicles typically rely on a combination of sonar, optical cameras, and inertial navigation systems to estimate their position relative to the guide vessel or a mother submarine. However, these methods can be limited by water turbidity, acoustic interference, and drift errors. Embedding an LD-FOSS sensor along the tether would enable continuous, "quiet," and high-precision tracking of the UUV's position and orientation with minimal hardware overhead. This would complement existing navigation systems and support the integrated positioning strategies toward which the subsea industry is currently progressing [19], [20].
3. Entanglement prevention represents another promising area of application. Recent literature explores strategies to prevent the tangling of tethers in systems involving multiple unmanned vehicles—both aerial and underwater—operating in close proximity [21]. LD-FOSS offers a natural extension to these approaches by providing direct, real-time shape information about each tether, allowing for the reconstruction of their relative paths and potential points of intersection. This capability could form the basis for proactive entanglement-avoidance algorithms or real-time control feedback for multi-robot coordination.

SOFT ROBOTICS

The final application that might benefit from LD-FOSS is also the most obvious as it already benefits from FOSS over short distances : soft robotics.

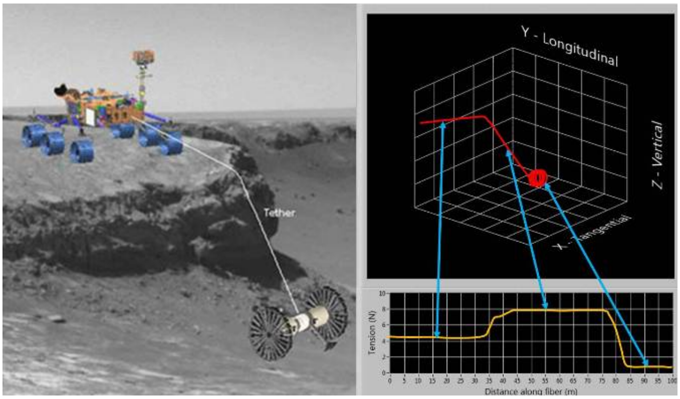

FIGURE 7.7. – *Project image from [18] : Fiber Optic Shape Sensing for Tethered Marsupial Rovers*

As mentioned in Chapter 5, LD-FOSS is an extension of the established FOSS technology, which itself is deployed most prominently in medical instruments and robotic limb tracking. Soft robotics specifically are being applied over longer distances in space exploration for surface and subsurface exploration of lava tunnels and ice caves [22]. Another emerging area is search and rescue robotics, where soft robots are designed to navigate through debris, confined spaces, or collapsed structures [23].

CONCLUDING REMARKS

The breadth of applications illustrate the use-case of LD-FOSS using distributed FO sensing to push the limits of the length of paths that can be reconstructed. Although the research presented in Chapter 6 only presents a proof-of-concept implementation of the technology, research should be continued following the principles discussed in Chapter 5 to fully investigate the possibilities and limitations presented by LD-FOSS.

RÉFÉRENCES

[1] Y. SUN, Y. S. KIM, S. QU et E. VERSCHUUR, « Joint migration inversion : features and challenges », *Journal of Geophysics and Engineering*, t. 17, n^{o} 3, p. 525-538, mars 2020, ISSN : 1742-2132. DOI : `10.1093/jge/gxaa012`. eprint : `https://academic.oup.com/jge/article-pdf/17/3/525/33034983/gxaa012.pdf`. adresse : `https://doi.org/10.1093/jge/gxaa012`.

[2] S. ABOLHASSANI, L. HOOGERBRUGGE et D. J. VERSCHUUR, « One-way reflection waveform inversion with depth-dependent gradient pre-conditioning », *Geophysical Journal International*, t. 240, nº 1, p. 652-672, nov. 2024, ISSN : 1365-246X. DOI : 10.1093/gji/ggae397. eprint : https://academic.oup.com/gji/article-pdf/240/1/652/60926453/ggae397.pdf. adresse : https://doi.org/10.1093/gji/ggae397.

[3] J. WANG, X. PAN, A. LI, F. LIU et J. JIAO, « Fast Joint Estimation of Direction of Arrival and Towed Array Shape Based on Marginal Likelihood Maximization », *Digital Signal Processing*, t. 154, p. 104 676, 2024. DOI : 10.1016/j.dsp.2024.104676.

[4] Q. WU et Y. XU, « A Nonlinear Data-Driven Towed Array Shape Estimation Method Using Passive Underwater Acoustic Data », *Remote Sensing*, t. 14, nº 4, p. 997, 2022. DOI : 10.3390/rs14040997.

[5] Q. WU, H. ZHANG, Z. LAI, Y. XU, S. YAO et J. TAO, « An Enhanced Data-Driven Array Shape Estimation Method Using Passive Underwater Acoustic Data », *Remote Sensing*, t. 13, nº 9, p. 1773, 2021. DOI : 10.3390/rs13091773.

[6] R. SINGH, S. KUMAR et S. BHAUMIK, « Bearing-Only Tracking Considering Dynamics of a Towed Sensor-Array », *IEEE Sensors Letters*, t. PP, p. 1-4, déc. 2024. DOI : 10.1109/LSENS.2024.3484649.

[7] R. K. SINGH, S. KUMAR et S. BHAUMIK, « Dynamics of a towed cable with sensor-array for underwater target motion analysis », *Franklin Open*, t. 11, p. 100 265, 2025, ISSN : 2773-1863. DOI : https://doi.org/10.1016/j.fraope.2025.100265. adresse : https://www.sciencedirect.com/science/article/pii/S2773186325000556.

[8] Q. WU et Y. XU, « A Nonlinear Data-Driven Towed Array Shape Estimation Method Using Passive Underwater Acoustic Data », *Remote Sensing*, t. 14, nº 2, 2022, ISSN : 2072-4292. DOI : 10.3390/rs14020304. adresse : https://www.mdpi.com/2072-4292/14/2/304.

[9] S. M. HANAFY, « Land-Streamer vs. Conventional Seismic Data for High-Resolution Near-Surface Surveys », *Applied Sciences*, t. 12, 2022, ISSN : 2076-3417. DOI : 10.3390/app12020584. adresse : https://www.mdpi.com/2076-3417/12/2/584.

[10] B. J. VILLAMIZAR et A. DESROCHES, « Reflection and Love-wave imaging of a buried valley using 2D 3C land-streamer seismic data », *Geophysics*, t. 90, nº 4, B157-B170, mai 2025, ISSN : 0016-8033. DOI : 10.1190/geo2024-0486.1. eprint : https://pubs.geoscienceworld.org/seg/geophysics/article-pdf/90/4/B157/7196339/geo-2024-0486.1.pdf. adresse : https://doi.org/10.1190/geo2024-0486.1.

[11] SCANM2, *3D Scanning and BIM for Oil Refinery Documentation*, Accessed : 2025-10-25, 2023. adresse : https://scanm2.com/portfolio/3d-laser-scanning-and-bim-for-oil-refinery-documentation/.

[12] ACTS, *Utility Mapping and Data Sharing to Mitigate Risk and Budget Overruns in Roading Projects*, Accessed : 2025-10-25, 2024. adresse : https://actsnowinc.com/global-811-magazine/the-importance-of-3d-utility-mapping-and-data-sharing-to-mitigate-risk-and-budget-overruns-in-roading-projects.

[13] 4. ANALYTICS, *What Is Underground Utility Mapping?*, Accessed : 2025-10-25, 2024. adresse : https://www.4manalytics.com/blog/what-is-underground-utility-mapping.

[14] B. utility SOLUTIONS, *Limitations of GPR : What Can and Cannot Be Detected Underground?*, Accessed : 2025-10-25, 2024. adresse : https://www.bessutilitysolutions.com/blog/limitations-of-ground-penetrating-radar/.

[15] M. METWALY, « Application of GPR technique for subsurface utility mapping : A case study from urban area of Holy Mecca, Saudi Arabia », *Measurement*, t. 60, p. 139-145, 2015, ISSN : 0263-2241. DOI : https://doi.org/10.1016/j.measurement.2014.09.064. adresse : https://www.sciencedirect.com/science/article/pii/S0263224114004448.

[16] W. ZHOU, Y. HUANG, J. CHEN et C. WANG, « Horizontal Directional Drilling Positioning Based on Strong Tracking Adaptive Kalman Filter », in *2025 8th International Conference on Advanced Algorithms and Control Engineering (ICAACE)*, 2025, p. 576-582. DOI : 10.1109/ICAACE65325.2025.11019103.

[17] C. DRAGOIE, « Survey Uncertainty and Implications for Development with Horizontal Wells », in *GEOconvention*, 2021. adresse : https://geoconvention.com/wp-content/uploads/abstracts/2021/67235-survey-uncertainty-and-implications-for-developmen.pdf.

[18] NASA, *Fiber Optic Shape Sensing for Tethered Marsupial Rovers*, Accessed : 2025-10-25, 2023. adresse : https://techport.nasa.gov/projects/16635?utm_source=chatgpt.com.

[19] C. ALEXANDRIS, P. PAPAGEORGAS et D. PIROMALIS, « Positioning Systems for Unmanned Underwater Vehicles : A Comprehensive Review », *Applied Sciences*, t. 14, nº 21, 2024, ISSN : 2076-3417. DOI : 10.3390/app14219671. adresse : https://www.mdpi.com/2076-3417/14/21/9671.

[20] J. WANG, X. PAN, L. CHENG et J. JIAO, « Adaptive Array Shape Estimation and High-Resolution Sensing for AUV-Towed Linear Array Sonar During Turns », *Remote Sensing*, t. 17, nº 15, p. 2690, 2025. DOI : 10.3390/rs17152690.

[21] G. BATTOCLETTI, D. BOSKOS, D. TOLIĆ, I. PALUNKO et B. D. SCHUTTER, « Entanglement Definitions for Tethered Robots : Exploration and Analysis », *IEEE Access*, t. 12, p. 178 153-178 170, 2024. DOI : 10.1109/ACCESS.2024.3507217. adresse : https://pure.tudelft.nl/ws/portalfiles/portal/231762728/Entanglement_Definitions_for_Tethered_Robots_Exploration_and_Analysis.pdf.

[22] Y. ZHANG, P. LI, J. QUAN, L. LI, G. ZHANG et D. ZHOU, « Progress, Challenges, and Prospects of Soft Robotics for Space Applications », *Advanced Intelligent Systems*, t. 5, nº 3, p. 2 200 071, 2023. DOI : `https://doi.org/10.1002/aisy.202200071`. eprint : `https://advanced.onlinelibrary.wiley.com/doi/pdf/10.1002/aisy.202200071`. adresse : `https://advanced.onlinelibrary.wiley.com/doi/abs/10.1002/aisy.202200071`.

[23] A. SEBASTIAN, « Soft Robotics for Search and Rescue : Advancements, Challenges, and Future Directions », fév. 2025, Preprint. DOI : `10.48550/arXiv.2502.12373`.

A

FIBRE OPTIC STRAIN SENSING USING OFDR

When a fibreglass core is directly connected to a laser source and a pulse is emitted, the light will travel through the core. As light travels through a transparent medium, its speed is given by $c = c_0/n$ where $c_0 = 3 \times 10^8$ m/s is the speed of light in a vacuum and n is the refractive index [1]. When the core is wrapped in highly reflective cladding, with a lower refractive index than the core, light that would otherwise leak can travel long distances along the core. The angle of incidence of the light hitting the core/cladding interface should be higher than the critical angle of reflectance angle as dictated by Snell's Law to ensure that all the light is reflected back into the core. For this reason, if the fibre is bent at a sharp angle, energy leakage may occur. The core itself is extremely thin so a coating is added around the cladding to protect it from environmental damage. The light travelling along the fibre and back towards the source can be used to measure continuous parameters along the fibre. Although there are different methods used to measure a variable along an optical fibre, in this thesis we have focused on Distributed Optical fibre Sensors (DOFSs), which determine the spatial distribution of a measurand along the fibre contrary to discrete measurements, which require interpolation like fibre Bragg Gratings (FBGs).

As the light travels along the transparent medium, it will scatter when encountering an imperfection in the atomic matrix and part of the energy will be backscattered towards the laser input where a sensor lays. Backscattered light will present with a shift in wavelength, which can be detected and attributed to a specific gauge along the fibre. A gauge can refer to a fixed location of increased refractive index (like in FBGs) or to a section of the sensor where backscattering occurs in DOFSs.

Figure A.1 shows the three types of spontaneous or stimulated photon scattering events that can be measured at different frequencies : Raman, Brillouin, and Rayleigh. For FOSS only Brillouin and Rayleigh back-scattering are relevant as they are sensitive to strain changes of the transmission medium. These non-overlapping back-scattering effects also allow for mixed interrogating of the same sensors (i.e., cycling between strain and temperature sensing). Table A.1 shows the criteria, that differentiate types of distributed strain sensing. It is important to note that these criteria are interconnected and trade-offs between accuracy and sensing lengths are intrinsic [2]. For the application of (U)HR streamer shape reconstruction, we propose that Optical Frequency Domain Reflectometry (OFDR) is the optimum option.

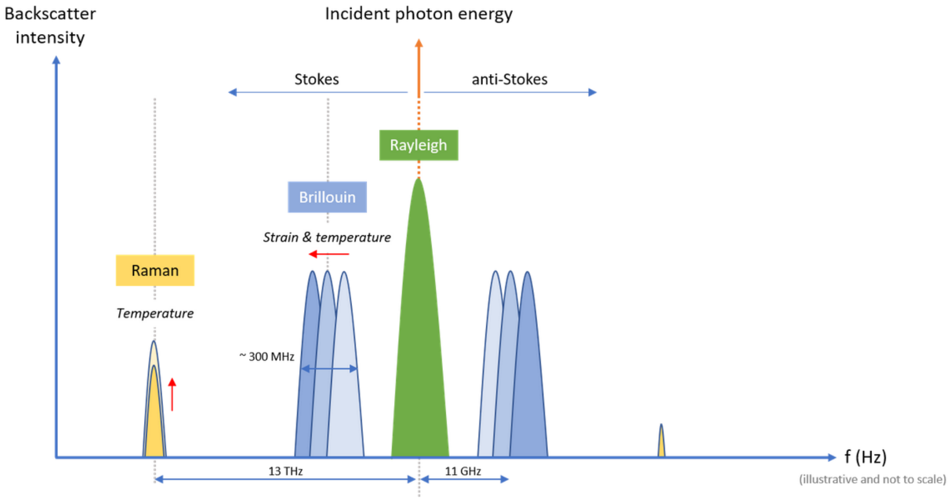

FIGURE A.1. – *Three types of photon scattering in optical fibre and their intensity at different frequencies and measurand state. Sourced from [3].*

OFDR technology uses a Tunable Laser Source (TLS), which produces a set of light pulses in a "chirp" linearly sweeping in frequency. The distance z along the Fibre Under Test (FUT) can be mapped to the frequency sweep as

$$z = \frac{v_g}{2\gamma} f_b, \tag{A.1}$$

where v_g is the group velocity of the light pulses, γ is the sweep rate of the TLS and f_b is the particular frequency at z [5], [6]. The sweep rate itself is a function of the sweep duration T_r and the frequency range Δf. We can therefore rewrite

Theory	Measurable	Sensing Range	Spatial Resolution
Rayleigh OTDR	T and ε	1 - 2 km	0.5 m
Rayleigh OFDR	T and ε	70 - 100 m	<5 mm
Brillouin BOTDA	T and ε	10 km	1.5 m
Brillouin BOTDR	T and ε	45 km	5 m
Brillouin PPP-BOTDA	T and ε	2 km / 0.5 km	10 cm/ 2 cm
Brillouin BOFDA	T and ε	9 m / 11 km	3 cm / 1.4 m
Raman	T	20 km	1 - 2 m

TABLE A.1. – *Comparison between different kinds of distributed fibre optic sensing systems as reported by [4] and corresponding to criteria reported by [2]. Acronyms used can be found in the Acronyms section of this thesis (C).*

Equation A.1 as

$$z = \frac{v_g}{2}\frac{T_r}{\Delta f} f_b, \tag{A.2}$$

and spatial resolution is then given by the range of the frequency sweep

$$dz = \frac{v_g}{2\Delta f}. \tag{A.3}$$

Finally the maximum sampled frequency as a function of FUT length L is given by

$$f_{max} = \frac{\Delta f}{L}\frac{2}{v_g T_r}, \tag{A.4}$$

As we can see, the high spatial-resolution of OFDR for the relatively long sensing-lengths, compared to other methods shown in Figure A.1 and Table A.1, is the result of its dependency on the frequency sweep range rather than the speed of the sweep. Methods like Optical Time Domain Reflectometry (OTDR) rely on short laser pulse duration to travel through the FUT and back leading to a higher maximum frequency f_{max} to be sampled which is technologically more challenging; hence the trade-off between resolution and sensing length in traditional time-domain Rayleigh based reflectometry.

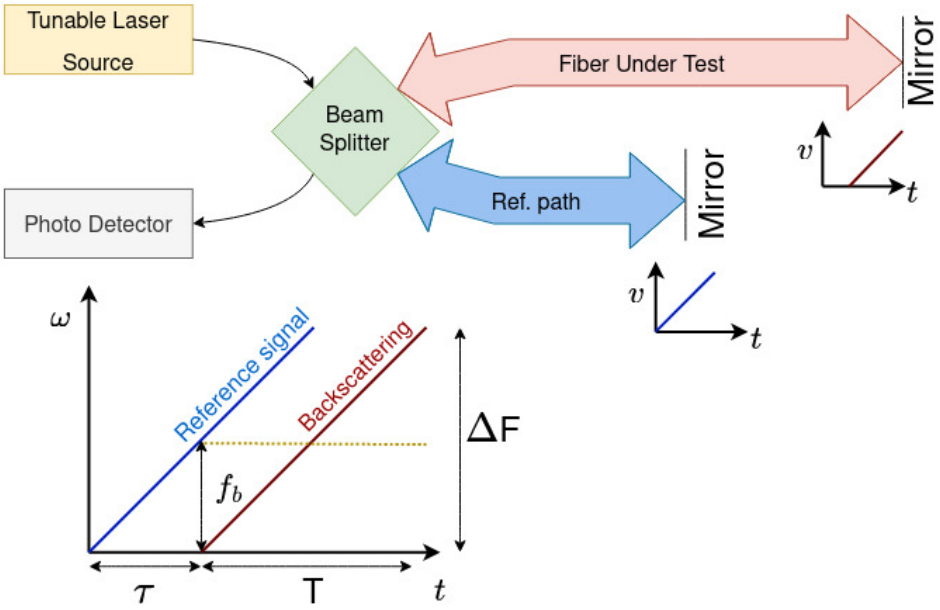

FIGURE A.2. – *Schematic representation of Mach-Zehnder interferometer used for OFDR with the beating signal (yellow dotted line) between reference and backscattering signals.*

Figure A.2 shows the schematic configuration of an OFDR system using a Mach-Zehnder interferometer. The light is channeled from the tunable laser source to the beam splitter where the energy is split into two paths. Before entering the beam splitter, the energy field can be described as a function of the instantaneous angular frequency $\omega(t)$ of the sweep [6] :

$$E_{in} = E_0 e^{-i\omega(t)}, \tag{A.5}$$

where E_0 is the amplitude of the signal and the frequency sweep in time t is a function of the frequency sweep γ, the initial frequency f_0, and the phase noise $e(t)$.

$$\omega(t) = 2\pi f_0 t + \pi\gamma t^2 + e(t). \tag{A.6}$$

At the beam splitter, the energy field is split into two identical fields. Each field travels through a different path; the first will typically travel through the FUT while the second travels an inert path of short length [7]. Part of the signal is backscattered as it travels along the FUT. The energy is the backscattered signal at a time delay τ is given by :

$$E_{FUT}(t) = \sqrt{R(\tau)}E_0 e^{\omega(t-\tau)}, \tag{A.7}$$

where R is the reflectivity attenuation of FUT related to the time delay τ. Both fields are reflected at the end of their individual paths back toward the beam splitter. The energy from the reference path can also be described in terms of its own (shorter) time delay. For simplicity, the common time delay between both paths is subtracted such that the reference path appears to have no time delay as shown in Equation A.5. At the beam splitter, both fields are recombined.

$$E_{out} = E_0(t+\tau_1)e^{-i\omega(t+\tau_1)t}E_0(t+\tau_2)e^{-i\omega(t+\tau_2)t}, \tag{A.8}$$

where τ_1 and τ_2 are the time delays of the signal traveling through the reference path and the FUT respectively. The electrical output detected at the photodetector is derived from the square magnitude of the electrical field :

$$I(t) = 2\sqrt{R(\tau)}E_0^2\cos(2\pi(f_0\tau+\gamma\tau t+\frac{1}{2}\gamma\tau^2+e(t)-e(t-\tau^2))) \tag{A.9}$$

where $e(t)-e(t-\tau^2)$ is the phase noise and $\gamma\tau$ is proportional to the frequency of the beating signal f_b.

RÉFÉRENCES

[1] A. GÜEMES, « Fiber Optics Strain Sensors », *NATO-STO Lecture Series (STO-EN-AVT-220)*, t. 16, 2014.

[2] A. HARTOG, *An introduction to distributed optical fibre sensors*. CRC Press, Taylor amp; Francis Group, 2018.

[3] N. GILBERTSSON, « Distributed Optical Fiber Sensing (DOFS) », *Teledyne SP Devices*, juin 2022.

[4] C. XU et S. KHODAEI Zahra, « Shape Sensing with Rayleigh Backscattering Fibre Optic Sensor », *Sensors*, t. 20, n° 14, p. 4040, 2020. DOI : https://doi.org/10.3390/s20144040.

[5] S. KREGER, A. RAHIM, N. GARG, S. KLUTE, D. METREY, N. BEATY, J. JEANS et R. GAMBER, « Optical frequency domain reflectometry : principles and applications in fiber optic sensing », mai 2016, 98520T. DOI : 10.1117/12.2229057.

[6] C. LIANG, Q. BAI, M. YAN, Y. WANG, H. ZHANG et B. JIN, « A Comprehensive Study of Optical Frequency Domain Reflectometry », *IEEE Access*, t. 9, p. 41 647-41 668, 2021. DOI : 10.1109/ACCESS.2021.3061250.

[7] LUNA, *Optical Distributed Sensor Interrogator Model ODiSI-B : User Guide*, English, LUNA, 2017, 127 p.

[8] C. CHAPELAND, « Novel hardware development for UHR streamer hydrophone position correction using fiber optic shape sensing », in *Proceedings of the European Association of Geoscientists & Engineers Conference*, t. 2023, 2023, p. 1-5. DOI : 10.3997/2214-4609.202320150.

[9] C. CHAPELAND, D. J. VESCHUUR et D. DRAGANOV, « Novel method for UHR streamer shape reconstruction and improved receiver positioning : A conceptual overview », in *Proceedings of the European Association of Geoscientists & Engineers Conference*, t. 2023, 2023, p. 1-5. DOI : 10.3997/2214-4609.2023101490.

[10] C. CHAPELAND, « High-resolution seismic velocity inversion and imaging of the shallow-subsurface using a combined JMI/FWI workflow », in *Proceedings of the European Association of Geoscientists & Engineers Conference*, t. 2022, 2022, p. 1-5. DOI : 10.3997/2214-4609.202210826.

[11] L. TRANI, G. A. PAGANI, J. P. P. ZANETTI, C. CHAPELAND et L. EVERS, « Deepquake — an application of CNN for seismo-acoustic event classification in the Netherlands », *Computers & Geosciences*, t. 159, p. 104 980, 2022, ISSN : 0098-3004. DOI : 10.1016/j.cageo.2021.104980.

B

4D FOSS EXAMPLE

During the shape-sensing experiments, the temporally continuous recording from the OFDR interrogator permitted 4D FOSS tests using the streamer and sensor sey-up presented in Chapter 6. Despite the lack of a 4D shape-validation method, the streamer was filmed and can be roughly visually compared with the reconstructed shape. Some comparison plots are shown below; frames where the hydrophones can be seen on the streamer (white modules) display strong twisting of the streamer. The full recording can be found using the following link : 4D-FOSS video.

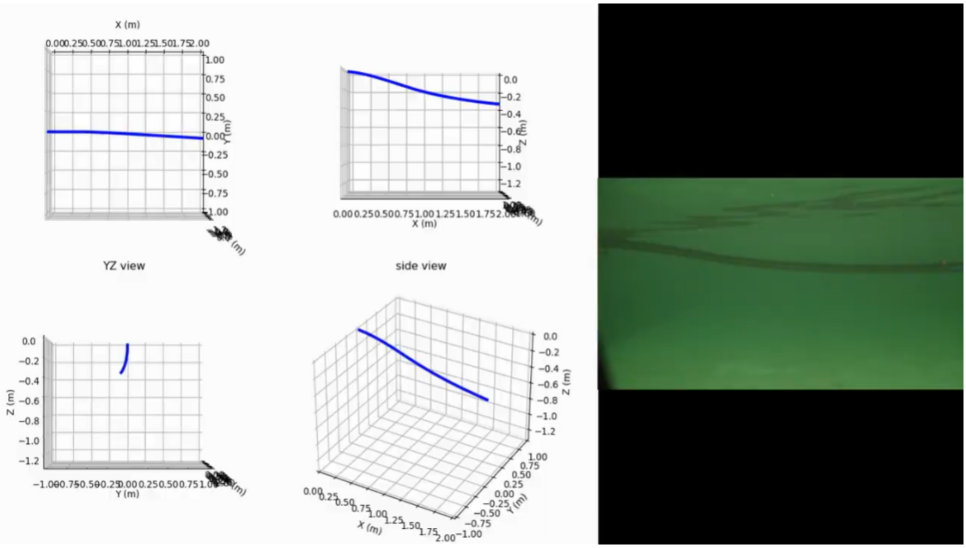

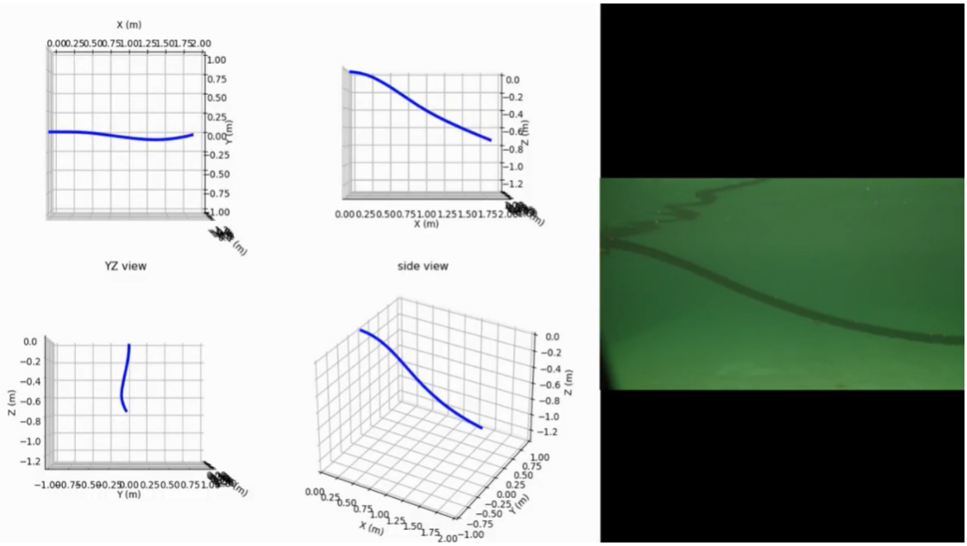
X (m)
0.00 0.25 0.50 0.75 1.00 1.25 1.50 1.75 2.00
1.00
0.75
0.50
0.25
0.00
−0.25
−0.50
−0.75
−1.00
Y (m)
0.0
−0.2
−0.4
−0.6
−0.8
−1.0
−1.2
Z (m)
X (m)
YZ view
side view
Z (m)
Y (m)
X (m)

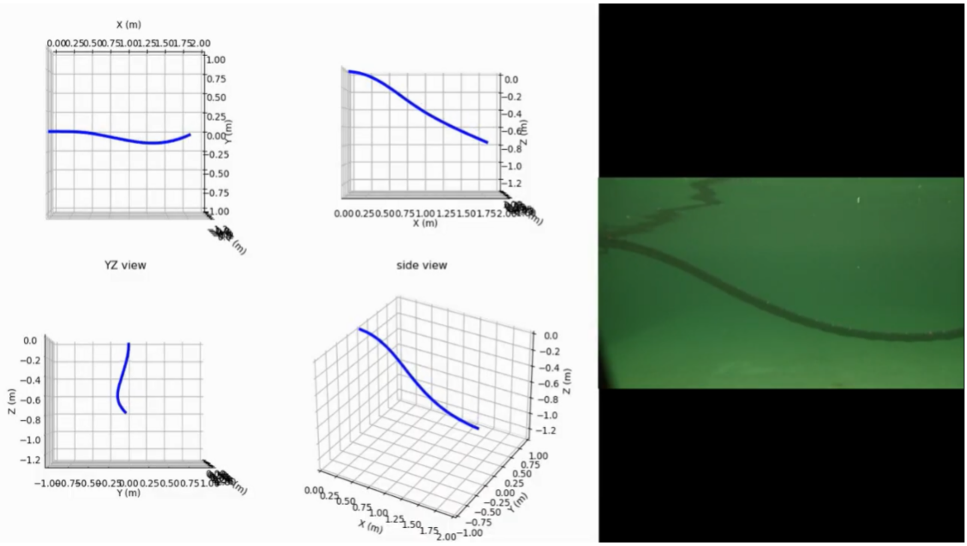
X (m)
0.00 0.25 0.50 0.75 1.00 1.25 1.50 1.75 2.00
1.00
0.75
0.50
0.25
0.00
−0.25
−0.50
−0.75
−1.00
Y (m)
0.0
−0.2
−0.4
−0.6
−0.8
−1.0
−1.2
Z (m)
X (m)
YZ view
side view
Z (m)
Y (m)
X (m)

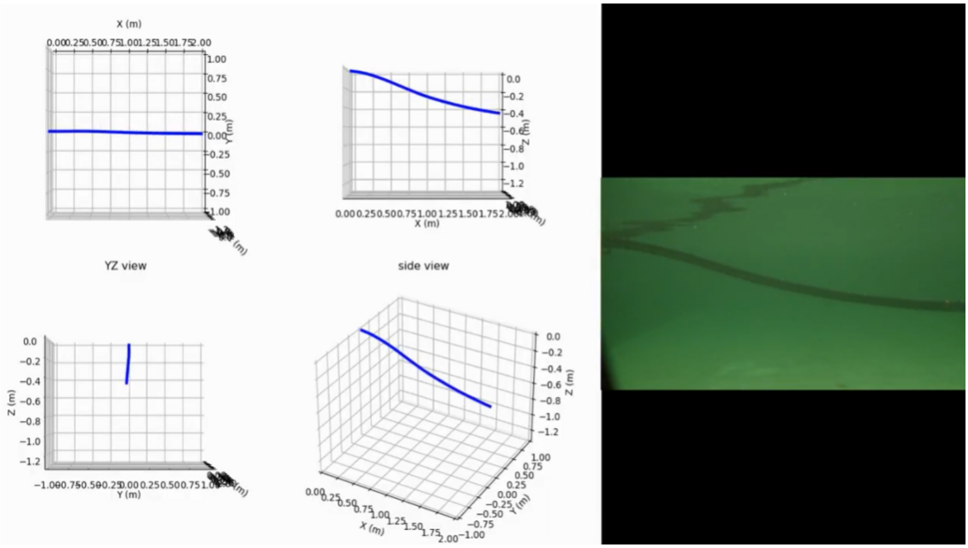
X (m)
Y (m)
YZ view
side view
Z (m)
Y (m)
X (m)
Z (m)
X (m)
Y (m)
Z (m)

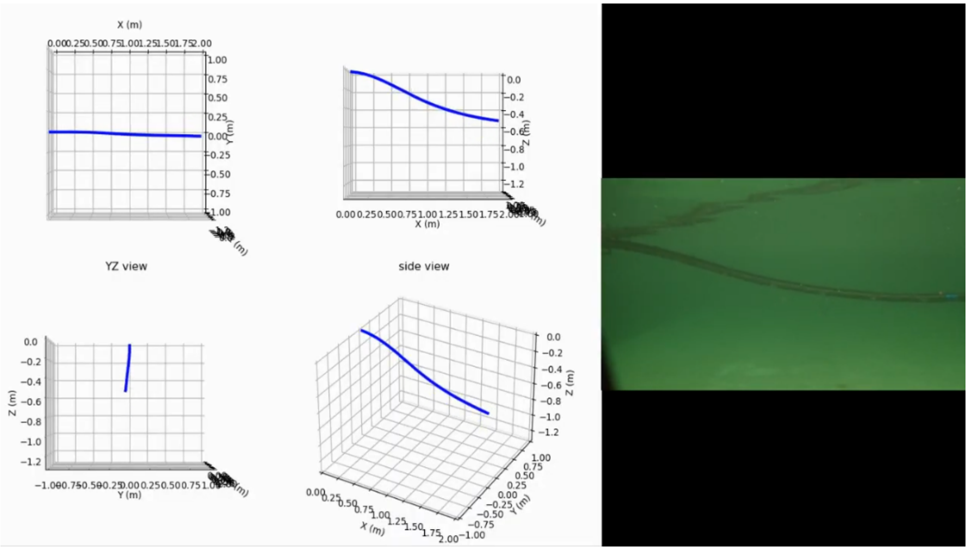
X (m)
Y (m)
YZ view
side view
Z (m)
Y (m)
X (m)
Z (m)
X (m)
Y (m)
Z (m)

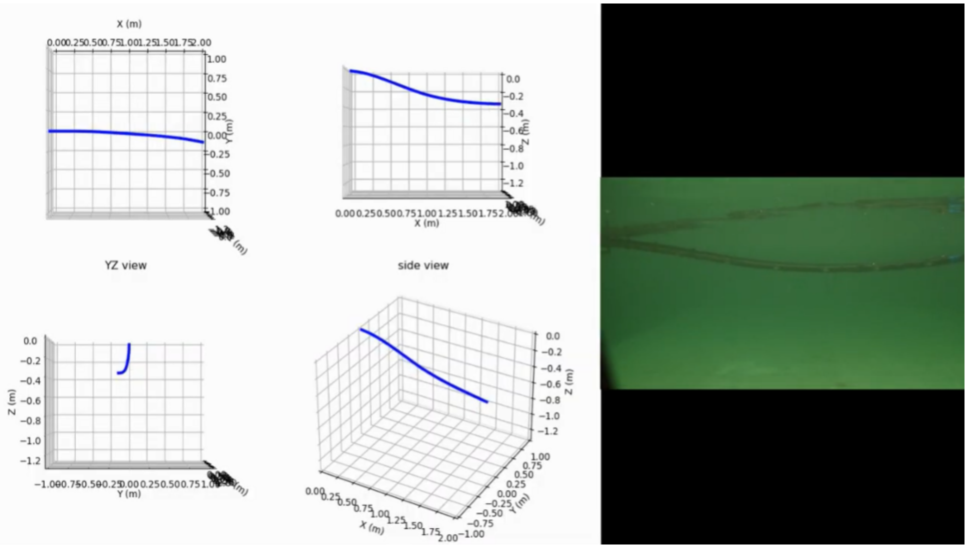
X (m)
Y (m)
YZ view
side view
X (m)
Z (m)
Y (m)
Z (m)
X (m)
Y (m)
Z (m)

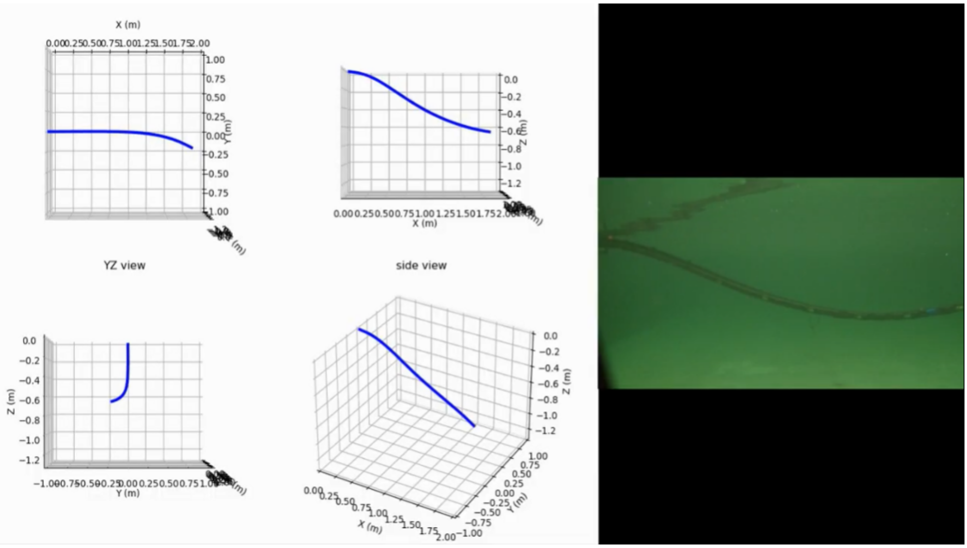
X (m)
Y (m)
YZ view
side view
X (m)
Z (m)
Y (m)
Z (m)
X (m)
Y (m)
Z (m)

C

ACRONYMS

BOFDA - Brillouin Optical Frequency Domain Analysis
BOTDA - Brillouin Optical Time Domain Analysis
BOTDR - Brillouin Optical Time Domain Reflectometry
BOT - Bearing-Only Tracking
CCS - Carbon Capture and Storage
CL-SRME - Closed-Loop Surface Related Multiples Elimination
CPT - Cone Penetration Test
CSEM - Controlled Source ElectroMagnetic
DAS - Distributed Acoustic Sensing
DOFS - Distributed Optical Fiber Sensors
FUT - Fiber Under Test
FBG - Fiber Braggs Gratings
FO - Fiber Optic
FOSS - Fiber Optic Shape Sensing
FWI - Full Waveform Inversion
FWM - Full Wavefield Migration
FWMod - Full Wavefield Modelling
JMI - Joint Migration Inversion
GN - Gauss-Newton
GPR - Ground Penetrating Radar
GPS - Global Positioning System
INS - Inertial Navigation Systems
JMI - Joint Migration Inversion
LD-FOSS - Long-Distance FOSS
OBC/N - Ocean Bottom Cable/Node
OFDR - Optical Frequency Domain Reflectometry

(HR)-ORWI	-	(High-Resolution) One-way Reflection Waveform Inversion
OTDR	-	Optical Time Domain Reflectometry
P/S-wave	-	Pressure/Shear wave
PPP-BOTDA	-	Pulse Pre-Pump BOTDA
RTK	-	Real-Time Kinematic
SBP	-	Sub-Bottom Profiler
TLS	-	Tunable Laser Source
(U)HR	-	(Ultra)-High-Resolution
UXO	-	UneXploded Ordnance

D

ACKNOWLEDGEMENTS

Although there is only one name on the cover, the work presented in this thesis is the product of scientific collaboration and was enabled by the support from the academic body of TUDelft and industry partners. I would like to spare some words to acknowledge the individuals that shaped my PhD journey into a positive and fruitful experience.

I would first like to express my sincere gratitude to my supervisors. **Gerrit Blacquière**, my first supervisor, supported me from the very beginning , including through the tumultuous COVID years, and I am especially grateful for his guidance during our collaboration with Fugro. **Deyan Draganov**, who accompanied me throughout the entire trajectory, offered continuous supervision, encouragement, and constructive insights. Your steady involvement helped me navigate the many stages of my research. After Gerrit's retirement, **Eric Verschuur** stepped in as supervisor. Eric, I am extremely grateful for your kindness, support, and generosity with your time. I particularly appreciate the encouragement from both Eric and Deyan when I decided to shift the direction of my research towards streamer shape sensing, a topic that was outside the general topics tackled by our group. The ability to pursue this research direction increased my self-confidence and was a major turning point in my professional life. Eric, Deyan and Gerrit, thank you again for this PhD experience.

I am also grateful to my **Delphi colleagues**, who were always willing to help when I was stuck and who taught me more than they may realize. Special thanks go to **Evgeniia Martuganova** for the coffee breaks that helped me decompress, and to **Andrea Cuesto Cano** for the many car-ride conversations that made long days feel a little shorter.

I wish to thank my collaborators at Deltares, whose expertise and enthusiasm pushed this project further than I could have imagined. **Manos Pefkos**, thank you for believing in my idea and for championing it within Deltares. Your positivity through the inevitable complications during the experiments kept our spirits high and our eyes looking forward. I also thank **Edvard Alrichs** for his solution-oriented advice and for providing technical support during both the bench experiments and the flume campaign. I might say that I am most grateful for your foresight on taking specific measurements "just in case" that turned out to be indispensable in my analysis.

Through Deltares, I had the great opportunity to work with **Marinus van der Hoek** who made our vision of the SSU2000 come to life and refined its design based on our discussion and experiments. Marinus, I am grateful to have had benefited from your extensive knowledge of fiber-optic sensing and for the precision-driven mindset you brought to the project. I like to tell myself that a little bit of that mindset has rub-off on me, although, I must admit that I do still own a can or two of silicone spray. Your patience and kindness were greatly appreciated, I hope to learn more from you in future projects.

Finally, I would like to honour the memory of **Olivier Monrigual**, who tragically left us too soon. I am deeply grateful to him for taking a chance on this research and for providing the shortened shape sensor used in the flume experiments through GEO Marine Survey Systems. His contribution remains an important part of this work, and his generosity and enthusiasm will not be forgotten.

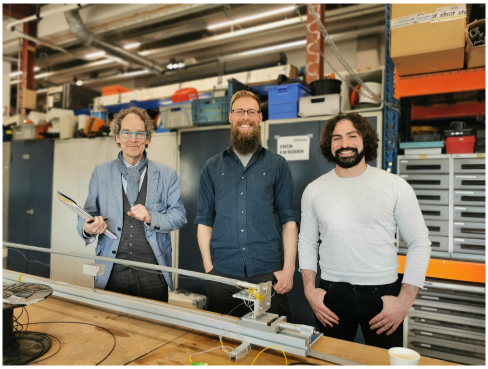

FIGURE D.1. – *The 3DES team (from left to right) : Marinus van der Hoek, Edvard Alrichs and Manos Pefkos*

CURRICULUM VITÆ

Camille Geneviève Marie CHAPELAND

EDUCATION

2020–2025	PhD Geophysics Delphi Consortium, TUDelft, Delft, Netherlands Thesis : *Understanding the offshore shallow subsurface : From inversion and imaging methods to acquisition hardware development.* Promotor : *dr. D.J. Verschuur* Supervisors : *dr. D. Draganov and dr. G. Blacquière*
2019–2020	M.Sc. Geophysics University of Utrecht, Utrecht, Netherlands Program : *Earth Structure and Dynamics* Thesis : *Machine learning engineer for automatic seismic event detection and classification* Supervisors : *Prof.dr. J. Trampert and Prof.dr. L.G. Evers*
2016–2019	Bachelors of Liberal Arts and Sciences University College Utrecht, Utrecht, Netherlands Majors : *Physics and Earth Science* Thesis : *FEM of mantle flow around craton boundaries* Supervisor : *dr C. Thieulot*
2014–2016	International Baccalaureate

International School of Kuala Lumpur, Kuala Lumpur, Malaysia

Awards

2023	Best Presentation Award Near-Surface Geoscience conference 2023, Edinburgh
2022	Best Poster Award CiTG poster day 2023, TUDelft, Netherlands

Certifications

2023	Technical cave diver, IANTD
2016	Divemaster, PADI

List of Publications

4. C. Chapeland, « Novel hardware development for UHR streamer hydrophone position correction using fiber optic shape sensing », in *Proceedings of the European Association of Geoscientists & Engineers Conference*, t. 2023, 2023, p. 1-5. doi : `10.3997/2214-4609.202320150`

3. C. Chapeland, D. J. Veschuur et D. Draganov, « Novel method for UHR streamer shape reconstruction and improved receiver positioning : A conceptual overview », in *Proceedings of the European Association of Geoscientists & Engineers Conference*, t. 2023, 2023, p. 1-5. doi : `10.3997/2214-4609.2023101490`

2. C. Chapeland, « High-resolution seismic velocity inversion and imaging of the shallow-subsurface using a combined JMI/FWI workflow », in *Proceedings of the European Association of Geoscientists & Engineers Conference*, t. 2022, 2022, p. 1-5. doi : `10.3997/2214-4609.202210826`

1. L. Trani, G. A. Pagani, J. P. P. Zanetti, C. Chapeland et L. Evers, « Deepquake — an application of CNN for seismo-acoustic event classification in the Netherlands », *Computers & Geosciences*, t. 159, p. 104 980, 2022, issn : 0098-3004. doi : `10.1016/j.cageo.2021.104980`